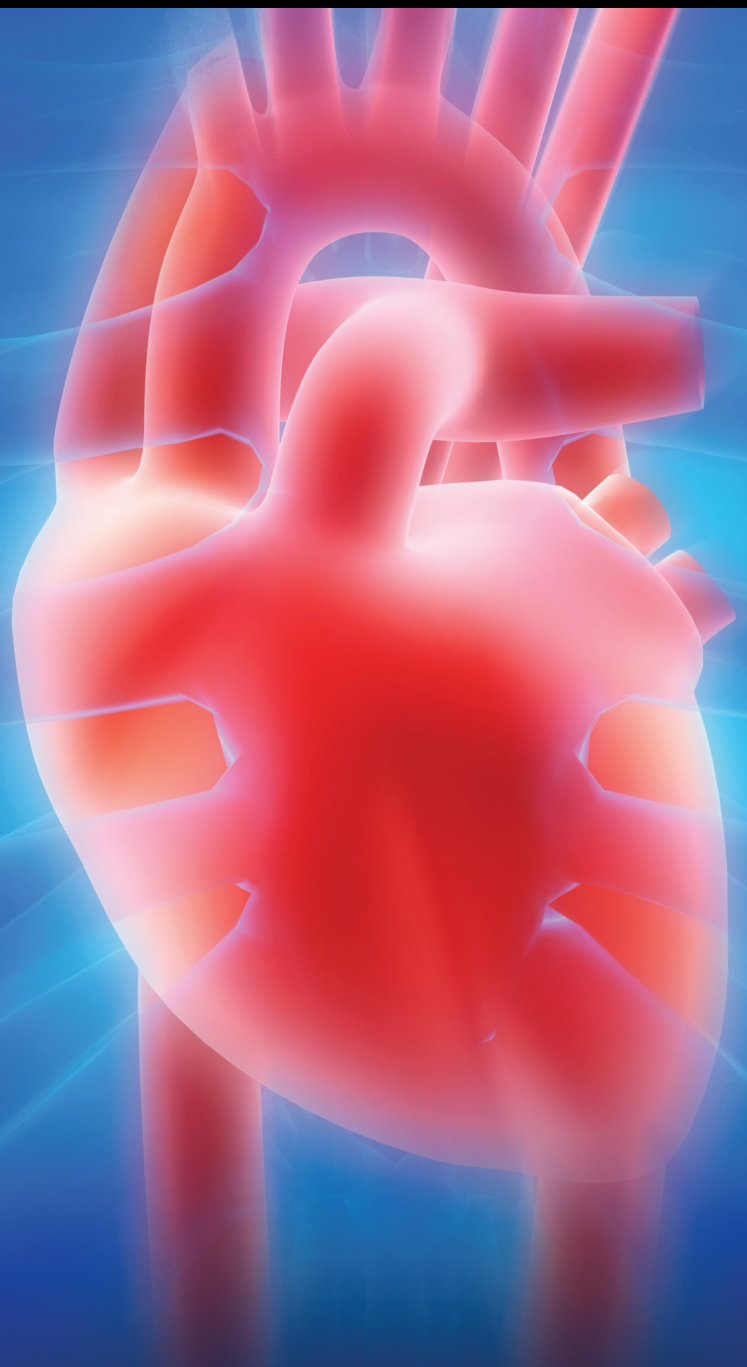# Advances in Hemodynamic Analysis in Cardiovascular Diseases

Lead Guest Editor: Zhen Qian
Guest Editors: Xiao Zhou and Anqiang Sun

Advances in Hemodynamic Analysis in Cardiovascular Diseases

Advances in Hemodynamic Analysis in Cardiovascular Diseases

Lead Guest Editor: Zhen Qian
Guest Editors: Xiao Zhou and Anqiang Sun

Contents

Research Article

Influence of Artery Straightening on Local Hemodynamics in Left Anterior Descending (LAD) Artery after Stent Implantation

Pengfei Liu, Xiaoyan Deng [ID], Xiao Liu [ID], Anqiang Sun [ID], and Hongyan Kang [ID]

Key Laboratory for Biomechanics and Mechanobiology of the Ministry of Education,
School of Biological Science and Medical Engineering, Beijing Advanced Innovation Center for Biomedical Engineering,
Beihang University, Beijing 100083, China

Correspondence should be addressed to Anqiang Sun; saq@buaa.edu.cn and Hongyan Kang; hongyankang@buaa.edu.cn

Academic Editor: Mariantonietta Cicoira

Objectives. The study investigates local hemodynamic environment changes caused by straightening phenomenon and the relationship between straightening phenomenon and in-stent restenosis. *Background.* Intravascular intervention is an effective treatment in restoring the normal flow conditions and vascular lumen. Unfortunately, in-stent restenosis often occurs in a subset of patients after stent implantation and limits the success of stent implantation outcomes. The implanted stent usually causes artery straightening locally, rather than coinciding and adjusting to the physiological curve exactly. Artery straightening would apparently modify the artery geometry and therefore alter the local hemodynamic environment, which may result in intimal hyperplasia and restenosis after stenting implantation. *Methods.* In the current investigation, we verify the hypothesis that the artery straightening influences the local hemodynamic state using the different 3D CT models. Flow analysis for blood in the left anterior descending coronary artery and the straightening model is simulated numerically. *Result.* The current results reveal that the straightening phenomenon alters the distribution of wall shear stress and flow patterns, decreases the wall shear stress (WSS), and increases the oscillatory shear index (OSI) and the relative residence time (RRT), especially at the proximal and distal areas of stenting. *Conclusions.* The local straightened geometry established after stent implantation was likely to generate portions of the stenting area to a high risk of neointimal hyperplasia and subsequent restenosis.

1. Introduction

Stents are usually implanted into stenotic coronary arteries to improve or restore blood flow environment. However, restenosis has some persistent problems that limit the development of percutaneous coronary intervention [1, 2, 3]. Studies reported that restenosis occurs in 12 % of patients after stent implantation [3].

The mechanisms responsible for restenosis were not yet fully elucidated. Stent geometry and its subsequent effects on localized hemodynamics may cause restenosis [4–6]. Williams et al. reported that reduced vessel compliance and altered distributions of the wall shear stress (WSS) within the stented region could induce restenosis occurrence [7–9]. Besides, previous studies demonstrated that smooth muscle and endothelial cell damage would be implicated as

potential factors for stimulating neointimal hyperplasia [8, 10, 11]. There was a putative link between the hemodynamic environment changes and restenosis [12, 13]. Moreover, Regar et al. found that the procedure-specific factors such as implantation technique also can influence restenosis [14].

In addition to these reasons, the existing researches suggested that the straightening phenomenon caused by stent implantation induced changes in local hemodynamic environment and the rate of restenosis occurrence rate [15–18]. However, these studies were just conducted with simple two-dimensional models or three-dimensional idealized models, which cannot illustrate the realistic blood flow environment [7, 19, 20].

The straightening phenomenon is usually due to the different curvatures between stent and lesion vessels,

resulting in two evident angle changes near both ends of the stented region. The present study hypothesized that the straightening phenomenon can change the local hemodynamic state and vascular geometry. These changes can increase the possibility of restenosis occurrence and affect the stent surgeries.

In order to verify this hypothesis, the study reconstructed the left anterior descending coronary artery (LAD) and the straightening model based on the realistic computed tomography (CT) images and stent. The normal blow flow condition is used to simulate the local hemodynamic state. This study revealed the changes in local hemodynamics caused by the straightening phenomenon and discussed the relationship between artery straightening and restenosis. The implications of this study help the determination of potential causes of restenosis after stent implantation and the optimization design of the stent.

2. Materials and Methods

2.1. Reconstruction of Normal and the Straightening Models.
The study reconstructed the realistic coronary artery model based on the CT scan images with Mimics (v15.0, Materialise, Ann Arbor, MI, USA). The CT relevant parameters were described as follows: 0.9 mm slice thickness, 0.45 mm slice increment, 0.324 mm pixel size, a 512×512 image resolution, and total 293 [21]. The LAD model was obtained from the coronary artery model by using intercept function. The features of stent structure would be neglected especially after the endothelialization [10, 20]. Therefore, only the artery curve information was considered in the modeling process. The straightening model was obtained from LAD fitting with the stent model. Subsequently, simple smoothing and surfacing processes were applied to the models with Geomagic Studio 2012 (3D Systems, Morrisville, NC, USA). The diameter of LAD is 1.7 mm. Using a stent-to-artery diameter ratio of 1.2, the diameter of the stent was defined as 2 mm, and the length of the stent was 7 mm. The two models are shown in Figure 1.

2.2. Meshing.
ANSYS ICEM 16.0 (ANSYS, Inc., Canonsburg, PA, USA) software was used to complete the models meshing. Hexahedral elements were used, and the number of boundary layer was set to 10, with the height ratio 1.1 and initial height 0.009 mm. The total node number of the normal model was 116081. The total node number of the straightening model was 112476. Two models' meshes are shown in Figure 2.

2.3. Simulation and Boundary Conditions.
Simulation calculation was conducted by ANSYS Fluent 16.0 software (ANSYS, Inc., Canonsburg, PA, USA) under the pulsatile flow conditions. Blood was modeled as a Newtonian fluid and assumed to be homogeneous and incompressible [22, 23]. The convergence criterion was set to 0.00001. The vascular wall was postulated to be nonslip of the rigid wall. The inlet condition used the realistic blood flow velocity (Figure 3) [24]. The numerical simulation was conducted

based on a three-dimensional incompressible Navier–Stokes equation and the conservation of mass:

$$\rho \left[\frac{\partial \mathbf{u}}{\partial t} + (\mathbf{u} \cdot \nabla)\mathbf{u} \right] + \nabla p - \mu \nabla^2 \mathbf{u} = 0, \tag{1}$$

$$\nabla \cdot \mathbf{u} = 0, \tag{2}$$

where $\mathbf{u}$ and p represent the fluid velocity vector and pressure, respectively. ρ and μ are the density and viscosity of blood $(\mu = 3.5 \times 10^{-3}\, \text{kg/m·s}$ and $\rho = 1050\, \text{kg/m}^3)$ [25]. SIMPLE algorithm was used to calculate the blood flow velocity, and pressure-based solver was used for pressure correction and to solve the momentum equation. Computation period was set to 1.08 s, each step for 0.008 s, with 136 steps in each cycle. Every cycle was required to obtain a convergence for the transient analysis. The largest number of iterations in every step was 500, and the total steps were 1000. The whole computational process spanned twelve working days.

2.4. Hemodynamic Parameters.
Postprocessing was conducted with Matlab (The Math Works, Natick, Mass) and Tecplot 360 2013R1 software using the data exported from ANSYS FLUENT 16.0. Three WSS-based hemodynamic parameters (TAWSS, OSI, and RRT) were calculated based on the research by Claudio Chiastra [13].

Wall shear stress (WSS) was defined to be the product of fluid viscosity and shearing velocity of the neighboring vascular wall. We used $1050\, \text{kg/m}^{-3}$ as the viscosity of blood. WSS had close connection with blood characters, blood flow velocity, and vascular morphology.

The time-averaged wall shear stress (TAWSS) was the average of WSS in the entire cardiac cycle of WSS. TAWSS was described as the characteristics of WSS in pulsatile flow. TAWSS was calculated as follows:

$$\text{TAWSS} = \frac{1}{T} \int_0^T |\mathbf{WSS}(\mathbf{s}, t)| \cdot dt, \tag{3}$$

where T is the duration of the cardiac cycle and $\mathbf{s}$ is the position on the vascular wall.

The oscillatory shear stress index (OSI) was the nondimensional parameter; it indicated the magnitude of WSS fluctuations during a cardiac cycle. It is defined as follows:

$$\text{OSI} = 0.5 \left[1 - \left(\frac{\left| (1/T) \int_0^T \mathbf{WSS}(\mathbf{s}, t) \cdot dt \right|}{(1/T) \int_0^T |\mathbf{WSS}(\mathbf{s}, t)| \cdot dt} \right) \right]. \tag{4}$$

The high OSI leads to the lack of endometrial cells function and the decisive factor to change cellular structure cyclic stress.

The relative residence time (RRT) is introduced:

$$\text{RRT} = \frac{1}{(1 - 2 \cdot \text{OSI}) \cdot \text{TAWSS}}. \tag{5}$$

The RRT is inversely proportional to the magnitude of the TAWSS vector and has obvious connections to the

(a)   (b)
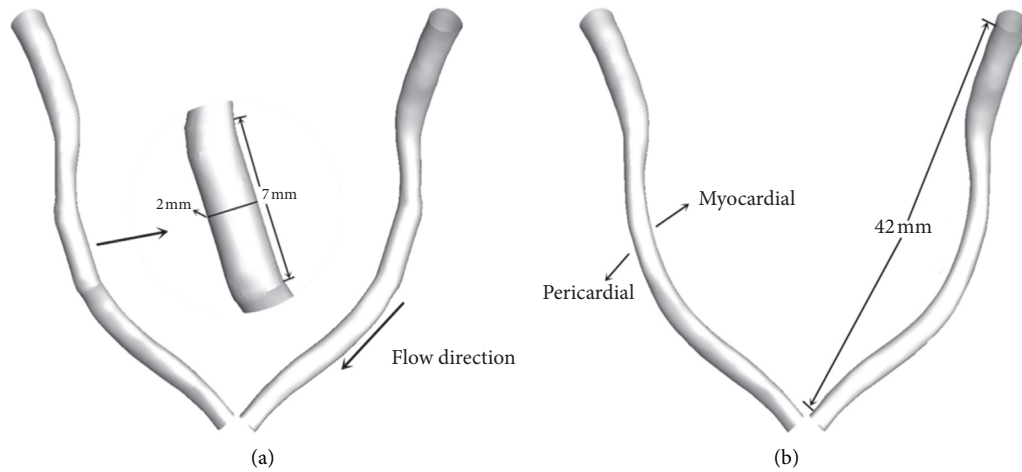
FIGURE 1: (a) Straightening and (b) normal models. The enlarged image shows the straightening phenomenon caused by stent implantation.

(a)   (b)
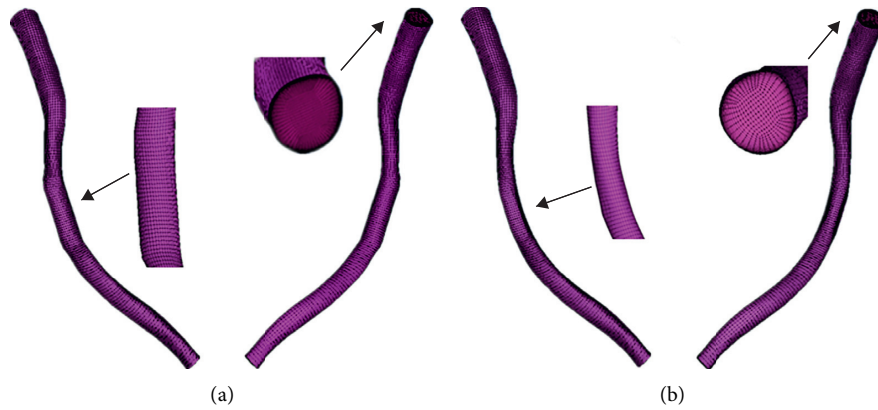
FIGURE 2: Mesh of the (a) straightening and (b) normal models.
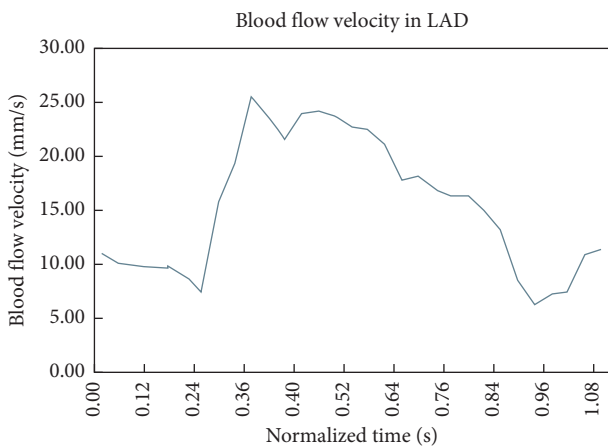
FIGURE 3: Inlet velocity pulsating flow. A representative waveform describing the average blood flow velocity measured in the proximal portion of a human left anterior descending coronary artery during a cardiac cycle. This waveform was used to complete the time-dependent simulations in the present study.

biological mechanisms of atherosclerosis. The OSI modifies the TAWSS effects on the RRT at a given region of the endothelium. Therefore, the RRT parameter includes the effects of both OSI and TAWSS.

3. Results

Two reconstruction models were used for simulation calculation; the best convergence cycle of seven cycles was selected to analyze the experiment data. On the basis of the hemodynamic parameters (blood flow velocity, WSS, TAWSS, OSI, and RRT), the study aimed at investigating the influence of straightening phenomenon after stent implantation on local hemodynamic environment in LAD.

3.1. The Blood Flow Velocity. Four points from one cardiac cycle are shown in Figure 4; early systole (t_1), peak systole (t_2), second peak systole (t_3), and end systole (t_4) were selected from one cardiac cycle.
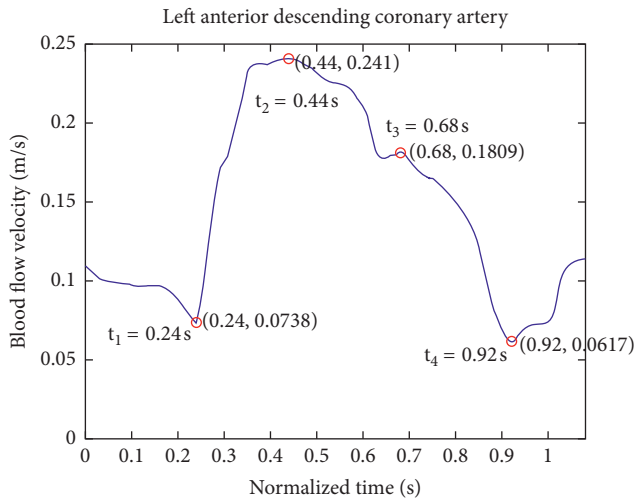
FIGURE 4: Four typical points during one cardiac cycle. t_1, t_2, t_3, and t_4 are selected from one cardiac cycle and, respectively, represent early systole, peak systole, second peak systole, and end systole.

Figure 5 shows the velocity streamlines in normal and straightening models. There was no obvious difference in the flow patterns and velocity between the models except the stenting area. In the stented area, the blood velocity of the straightening model obviously decreased. The highest blood flow velocity and the maximum difference of velocity between models emerged at the t_2 moment. In contrast, the t_4 moment had the lowest blood flow velocity and the minimum difference of velocity between models. The flow pattern of the straightening model obviously altered at time t_1 and time t_3. According to the velocity contours, the velocity near the pericardial surface was higher. The difference of velocity distribution between two models increased from t_1 to t_3, and the maximum disparity occurred at time t_3.

3.2. WSS and TAWSS. Contours of the WSS at the four points are shown in Figure 6. The distributions of WSS between models except the stented area were similar. In the stented area, the distributions of WSS were significantly altered, and the WSS was reduced by the straightening phenomenon. The WSS of the straightening model illustrates a gradient increase along the pericardial surface. To compare with other points, the maximum change in WSS between two models occurred at the t_2 moment, and the minimum difference occurred at time t_4. From the straightening model, the highest average WSS was 8.77 Pa at time t_2, and the lowest average WSS was 2.20 Pa at time t_4. Meanwhile, from the normal model, it increased to 11.27 Pa at time t_2 and 2.68 Pa at time t_4.

The distribution of TAWSS is described in Figure 7 (TAWSS counters on different models), and similar distribution of TAWSS was observed compared with above-described WSS distribution. Within the stented area, the TAWSS of the straightening model significantly decreased, especially at the inlet and outlet of the stenting region and the pericardial surface. Examination of TAWSS as a function of normalized axial length revealed that TAWSS of the straightening model was greater at the pericardial compared to the myocardial luminal surface. The largest TAWSS difference occurred at the inlet area.

3.3. OSI and RRT. Figure 8 shows the contours of OSI on the different models. Generally, the areas of high OSI were observed in areas of low WSS where the direction changed frequently. The significantly higher OSI of the straightening model was observed at the inlet of the stented area compared to the normal (shown in enlarge image).

The contours of RRT under different conditions are shown in Figure 9. The straightening phenomenon increased RRT values within the stented area, especially the RRT at the inlet of the stent and the pericardial surface. From the straightening model, the difference of RRT on both sides was higher. The highest RRT of the straightening model was calculated at the inlet of the stent along the myocardial surface, and the maximum RRT difference between two models occurred in this region. Beyond all that, the straightening phenomenon had a serious influence on the distribution of RRT.

4. Discussion

Stenting is used as an important treatment for critical artery stenosis. However, postoperation complications are still perplexing the patients over time, for example, neo-intimal hyperplasia and subsequent restenosis [7, 8, 9, 17, 26]. The reasons causing the restenosis are still being explored. Numerous studies have been conducted to investigate the potential influences including stent types, carrying drugs, and many postoperative and intraoperative factors [26–28]. As the compliance of the stent usually does not adjust to the curved artery, artery "straightening" is easily formed at the stented areas, potentially changing the local blood flow features and consequently influencing arterial cells behaviors and inducing tissue remodeling. It would be very useful and necessary to investigate the detailed hemodynamic changes in the straightened areas after stenting. Some studies focused on the straightening of vascular caused by stent implantation, but the relationship between the straightening phenomenon and restenosis was unclear [15–17, 28]. In these published studies, idealized cylindrical models were usually used to examine flow patterns through stented vessels with "straightening" [7, 19, 20]. However, the detailed local hemodynamic features changed by straightening phenomenon in realistic 3D models was not clear.

In the last 5 decades, the low wall shear stress hypothesis of atherosclerosis proposed by Caro et al. has been validated [29]. The connection between low WSS and high intimal proliferation had been further certified in rodents [30]. The vascular regions subjected to WSS below 0.5 Pa have been shown to strongly correlate with sites of intimal thickening [31, 32]. Low TAWSS was thought to be associated with regions of cellular proliferation and the potential factors for the development of neointimal.[33]. The high OSI created greater endothelial cells proliferation, and increased RRT
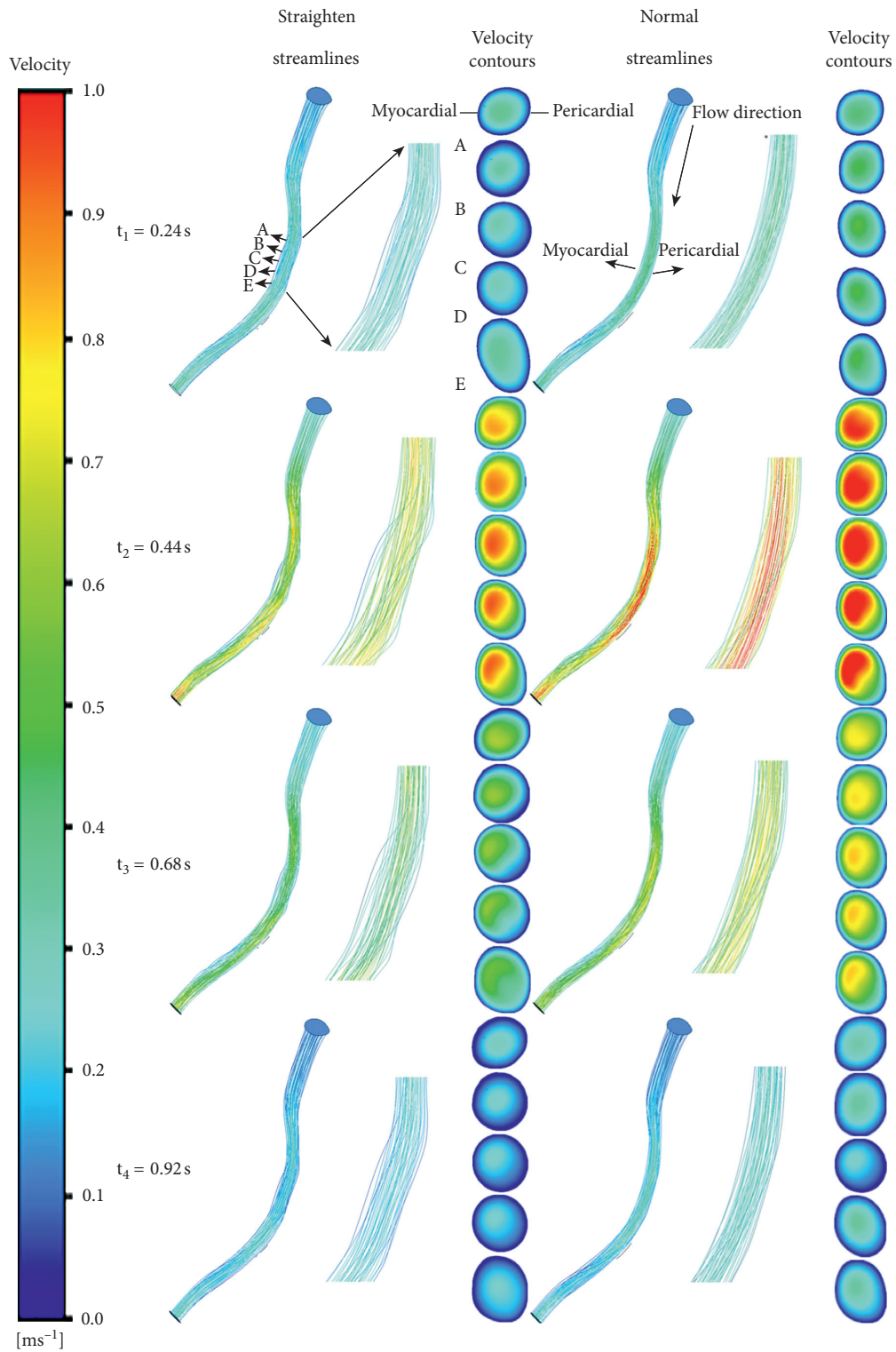
FIGURE 5: The streamlines near the left anterior descending coronary artery at four typical points with the various models. Cross sections are velocity contours in different moments of the different models. A, B, C, D, and E are selected from the models, and the first point is located at the inlet of the stented region. The distance between two points is 1 mm, and these points are also shown. Slicing in these points along the direction perpendicular to the centerline forms the cross sections.
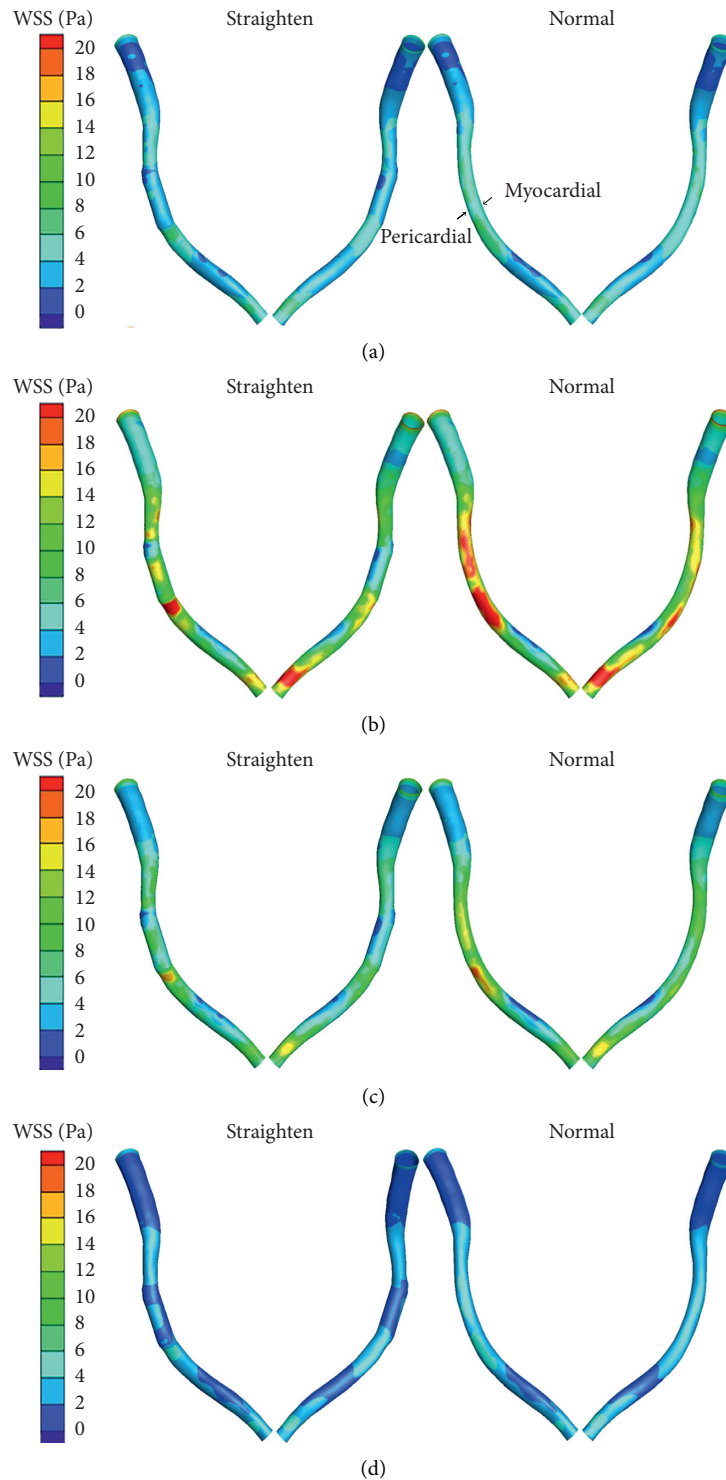
FIGURE 6: Counters of WSS at four typical points: (a) $t_1 = 0.24$ s; (b) $t_2 = 0.44$ s; (c) $t_3 = 0.68$ s; (d) $t_4 = 0.92$ s.

had obvious connections with biological mechanisms of atherosclerosis [18]. Moreover, Colombo pointed that abnormal blood flow patterns can promote inflammation, endothelial cells proliferation, and thrombosis [34].

In study, the straightening phenomenon caused by stent implantation was an potential factor to the restenosis. Normal and straightening models based on CT images were

reconstructed, and blood flow parameters in LAD were used as boundary conditions. The numerical simulation results revealed the straightening phenomenon altered the lumen geometry and consequently changed blood flow patterns in the local areas. The velocity and WSS in the stented area decreased after the straightening phenomenon. Besides, the RRT and OSI increased on the straightening model. The significant changes
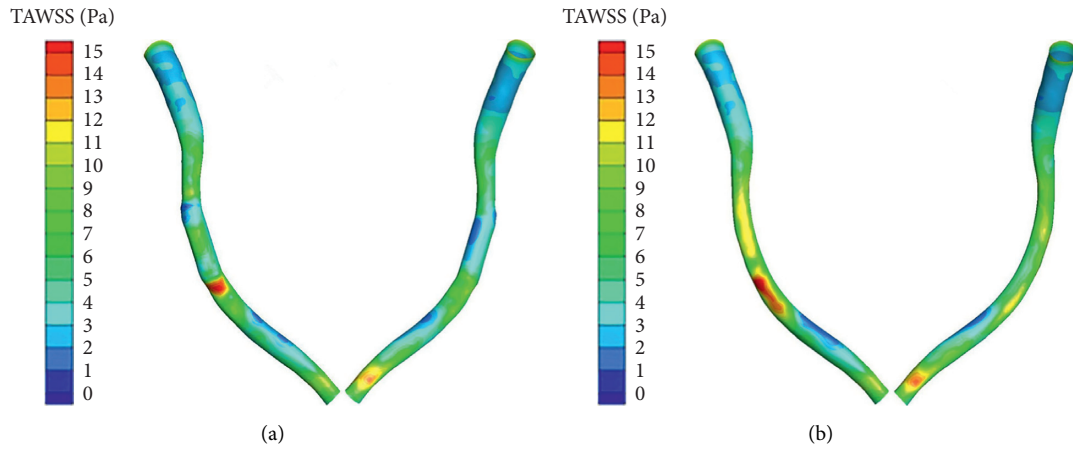
Figure 7: Counters of TAWSS: (a) straightening; (b) normal.
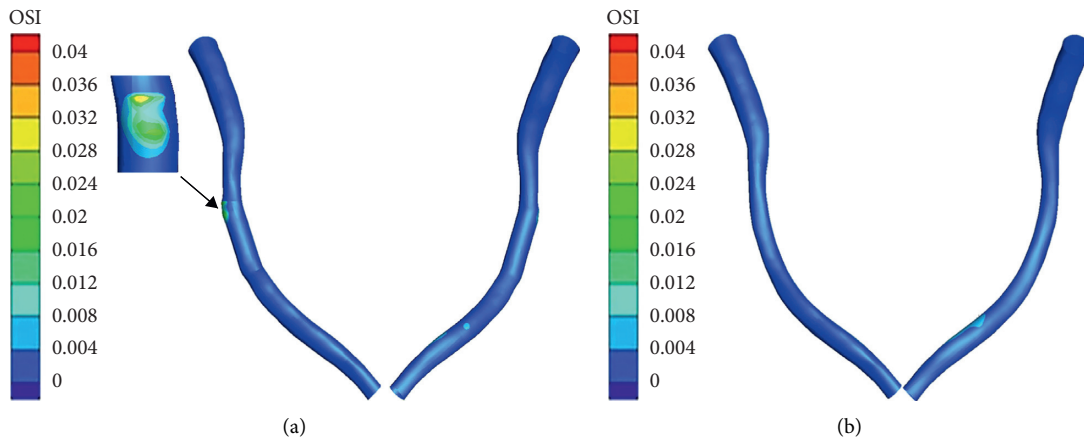
Figure 8: Counters of OSI: (a) straightening; (b) normal.
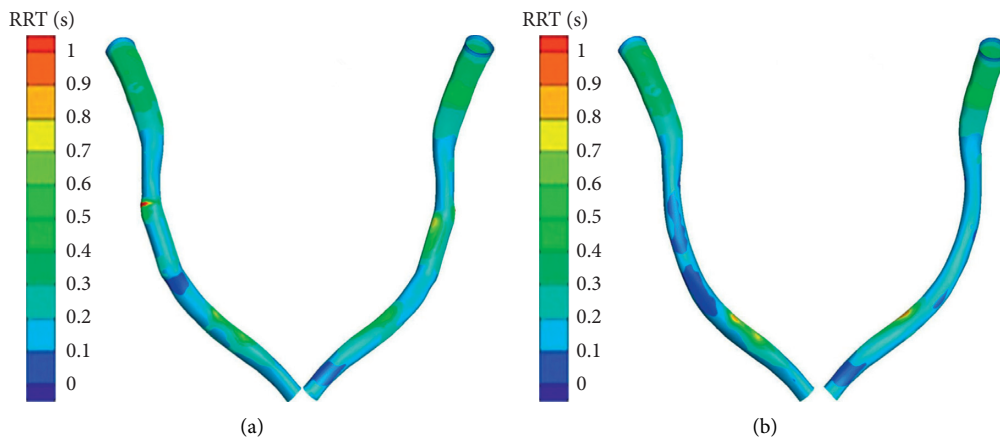
Figure 9: Counters of relative residence time (RRT): (a) straightening; (b) normal.

in parameters happened especially at the proximal and distal end of stented areas and the pericardial surface. As the low WSSs, high RRTs, and high OSIs were all indexes of restenosis subsequently [18], the straightening phenomenon hereby would induce a hemodynamic environment in LAD that promotes these conditions. Therefore, we conclude that the straightening phenomenon could affect the hemodynamic environment in the LAD and expose the endothelial cells to low WSS, high OSI, and high RRT conditions. These can make stented area more likely to cause the restenosis and neointimal hyperplasia, especially at the proximal and distal ends of the stented area and the pericardial surface. This conclusion

coincided with the findings of Wentzel and colleagues who observed clinical evidence of restenosis in [16].

Because some assumptions and simplification have been used in this study (e.g., the rigid wall assumption and neglect of detailed stent strut features), the results may not perfectly describe the hemodynamic environment in the straightened areas. However, the present study can still provide some clues to investigate the physiological and pathological impacts of straightening phenomenon after stent implantation.

In the future, at least two issues should be highly concerned. The first one is to analyze the artery wall stress and strain in the straightened areas. Because the arterial wall remodeling could be significantly regulated by the stress and strain in the artery [35]. The second one is the drug delivery and deposition characteristics in the special hemodynamic environment caused by straightening phenomenon. Drug eluting stent (DES) is now being prevalently used in clinics, and previous studies had proved the high correlation between local blood flow patterns and drug delivery [12, 36, 37]. Thus, investigating the drug delivery and deposition characteristics in straightened areas will be important in optimizing DES stenting.

5. Conclusion

This study investigated the local hemodynamic environment changes caused by straightening phenomenon. And we explored the relationship between the straightening phenomenon and the restenosis. The straightening phenomenon would lead to the decrease in WSS, TAWSS, and blood flow velocity and increase in RRT and OSI. This study concluded that the regional geometry of straightening phenomenon established after stent implantation is likely to lead to portions of the stenting area to a high risk of neointimal hyperplasia and subsequent restenosis (especially in the inlet and outlet of the stent and the pericardial surface). This study could help elucidate the mechanism of restenosis and promote the development of stent technology. This study can also serve as a reminder of the potential risks and provide useful guides in the stent deployment procedures.

Abbreviations

CT: Computed tomography
LAD: Left anterior descending
WSS: Wall shear stress
TAWSS: Time-averaged wall shear stress
OSI: Oscillatory shear stress index
RRT: Relative residence time.

Data Availability

The data used to support the findings of this study are included within the article.

Conflicts of Interest

The authors declare that they have no conflicts of interest.

Acknowledgments

References

[1] J. F. Ladisa, I. Guler, L. E Olson et al., "Three-dimensional computational fluid dynamics modeling of alterations in coronary wall shear stress produced by stent implantation," *Annals of Biomedical Engineering*, vol. 31, no. 31, pp. 972–980, 2003.

[2] S. B. Simon, "A randomized comparison of coronary-stent placement and balloon angioplasty in the treatment of coronary artery disease. Stent Restenosis Study Investigators," *New England Journal of Medicine*, vol. 331, no. 8, pp. 496–501, 1994.

[3] K. Palialexis, S. Spiliopoulos, A. Dalakidis et al., "Covered stents for symptomatic iliac artery in-stent restenosis treatment: midterm Results," *Hellenic Journal of Radiology*, vol. 2, no. 2, 2017.

[4] A. B. Fontaine, D. G. Spigos, G. Eaton et al., "Stent-induced intimal hyperplasia: are there fundamental differences between flexible and rigid stent designs?" *Journal of Vascular and Interventional Radiology*, vol. 5, no. 5, pp. 739–744, 1994.

[5] A. Kastrati, J. Mehilli, J. Dirschinger et al., "Restenosis after coronary placement of various stent types," *The American Journal of Cardiology*, vol. 87, no. 1, pp. 34–39, 2001.

[6] C. J. Vrints, M. J. Claeys, J. Bosmans, V. Conraads, and J. P. Snoeck, "Effect of stenting on coronary flow velocity reserve: comparison of coil and tubular stents," *Heart*, vol. 82, no. 4, pp. 465–470, 1999.

[7] A. R. Williams, B.-K. Koo, T. J. Gundert, P. J. Fitzgerald, and J. F. LaDisa, "Local hemodynamic changes caused by main branch stent implantation and subsequent virtual side branch balloon angioplasty in a representative coronary bifurcation," *Journal of Applied Physiology*, vol. 109, no. 2, pp. 532–540, 2010.

[8] J. M. Garasic, E. R. Edelman, J. C. Squire, P. Seifert, M. S. Williams, and C. Rogers, "Stent and artery geometry determine intimal thickening independent of arterial injury," *Circulation*, vol. 101, no. 7, pp. 812–818, 2000.

[9] C. Rogers and E. R. Edelman, "Endovascular stent design dictates experimental restenosis and thrombosis," *Circulation*, vol. 91, no. 12, pp. 2995–3001, 1995.

[10] L. D. J. Jr, L. E. Olson, R. C. Molthen et al., "Alterations in wall shear stress predict sites of neointimal hyperplasia after stent implantation in rabbit iliac arteries," *Ajp Heart & Circulatory Physiology*, vol. 288, no. 5, pp. H2465–H2475, 2005.

[11] R. S. Schwartz, K. C. Huber, J. G. Murphy et al., "Restenosis and the proportional neointimal response to coronary artery injury: results in a porcine model," *Journal of the American College of Cardiology*, vol. 19, no. 2, pp. 267–274, 1992.

[12] C. Chiastra, S. Morlacchi, D. Gallo et al., "Computational fluid dynamic simulations of image-based stented coronary

bifurcation models," *Journal of the Royal Society Interface*, vol. 10, no. 84, p. 57, 2013.

[13] G. Liu, J. Wu, D. N. Ghista, W. Huang, and K. K. L. Wong, "Hemodynamic characterization of transient blood flow in right coronary arteries with varying curvature and side-branch bifurcation angles," *Computers in Biology and Medicine*, vol. 64, pp. 117–126, 2015.

[14] E. Regar, G. Sianos, and P. W. Serruys, "Stent development and local drug delivery," *British Medical Bulletin*, vol. 59, no. 1, pp. 227–248, 2001.

[15] M. Gyöngyösi, P. Yang, A. Khorsand, and D. Glogar, "Longitudinal straightening effect of stents is an additional predictor for major adverse cardiac events," *Journal of the American College of Cardiology*, vol. 35, no. 6, pp. 1580–1589, 2000.

[16] J. J. Wentzel, M. D. Whelan, W. J. van der Giessen et al., "Coronary stent implantation changes 3-D vessel geometry and 3-D shear stress distribution," *Journal of Biomechanics*, vol. 33, no. 10, pp. 1287–1295, 2000.

[17] J. F. LaDisa, L. E. Olson, H. A. Douglas et al., "Alterations in regional vascular geometry produced by theoretical stent implantation influence distributions of wall shear stress: analysis of a curved coronary artery using 3D computational fluid dynamics modeling," *Biomedical Engineering Online*, vol. 5, no. 1, p. 1, 2006.

[18] A. M. Malek, S. L. Alper, and S. Izumo, "Hemodynamic shear stress and its role in atherosclerosis," *Jama*, vol. 282, no. 21, pp. 2035–2042, 1999.

[19] L. D. J. Jr, L. E. Olson, I. Guler et al., "Circumferential vascular deformation after stent implantation alters wall shear stress evaluated with time-dependent 3D computational fluid dynamics models," *Journal of Applied Physiology*, vol. 98, no. 3, pp. 947–957, 2005.

[20] J. F. LaDisa, L. E. Olson, I. Guler et al., "Stent design properties and deployment ratio influence indexes of wall shear stress: a three-dimensional computational fluid dynamics investigation within a normal artery," *Journal of Applied Physiology*, vol. 97, no. 1, pp. 424–430, 2004.

[21] X. Tian, A. Sun, X. Liu et al., "Influence of catheter insertion on the hemodynamic environment in coronary arteries," *Medical Engineering & Physics*, vol. 38, no. 9, pp. 946–951, 2016.

[22] D. J. Patel and R. N. Vaishnav, *Basic Hemodynamics and its Role in Disease Processes*, pp. p1–504, University. Park Press, Baltimore, 1980.

[23] Z. Wang, A. Sun, Y. Fan, and X. Deng, "Comparative study of Newtonian and non-Newtonian simulations of drug transport in a model drug-eluting stent," *Biorheology*, vol. 49, no. 4, pp. 249–259, 2012.

[24] R. F. Wilson, D. E. Laughlin, P. H. Ackell et al., "Transluminal, subselective measurement of coronary artery blood flow velocity and vasodilator reserve in man," *Circulation*, vol. 72, no. 1, pp. 82–92, 1985.

[25] T. Chaichana, Z. Sun, and J. Jewkes, "Computation of hemodynamics in the left coronary artery with variable angulations," *Journal of Biomechanics*, vol. 44, no. 10, pp. 1869–1878, 2011.

[26] M. De Beule, P. Mortier, S. G. Carlier, B. Verhegghe, R. Van Impe, and P. Verdonck, "Realistic finite element-based stent design: the impact of balloon folding," *Journal of Biomechanics*, vol. 41, no. 2, pp. 383–389, 2008.

[27] J. Murphy and F. Boyle, "Predicting neointimal hyperplasia in stented arteries using time-dependant computational fluid dynamics: a review," *Computers in Biology and Medicine*, vol. 40, no. 4, pp. 408–418, 2010.

[28] W. Wu, W.-Q. Wang, D.-Z. Yang, and M. Qi, "Stent expansion in curved vessel and their interactions: a finite element analysis," *Journal of Biomechanics*, vol. 40, no. 11, pp. 2580–2585, 2007.

[29] C. G. Caro, J. M. Fitz-Gerald, and R. C. Schroter, "Atheroma and arterial wall shear. Observation, correlation and proposal of a shear dependent mass transfer mechanism for atherogenesis," *Proceedings of the Royal Society of London. Series B, Biological Sciences*, vol. 177, no. 177, pp. 109–159, 1971.

[30] C. K. Zarins, D. P. Giddens, B. K. Bharadvaj, V. S. Sottiurai, R. F. Mabon, and S. Glagov, "Carotid bifurcation atherosclerosis. Quantitative correlation of plaque localization with flow velocity profiles and wall shear stress," *Circulation Research*, vol. 53, no. 4, pp. 502–514, 1983.

[31] D. N. Ku, D. P. Giddens, C. K. Zarins, and S. Glagov, "Pulsatile flow and atherosclerosis in the human carotid bifurcation. Positive correlation between plaque location and low oscillating shear stress," *Arteriosclerosis: An Official Journal of the American Heart Association, Inc.* vol. 5, no. 3, pp. 293–302, 1985.

[32] B. Su, Y. Huo, G. S. Kassab et al., "Numerical investigation of blood flow in three-dimensional porcine left anterior descending artery with various stenoses," *Computers in Biology and Medicine*, vol. 47, no. 1, pp. 130–138, 2014.

[33] J. P. Archie Jr., S. Hyun, C. Kleinstreuer et al., "Hemodynamic parameters and early intimal thickening in branching blood vessels," *Critical Reviews™ in Biomedical Engineering*, vol. 29, no. 1, 2001.

[34] A. Colombo, E. Bramucci, S. Saccà et al., "Randomized study of the crush technique versus provisional side-branch stenting in true coronary bifurcations," *Circulation*, vol. 119, no. 1, pp. 71–78, 2009.

[35] Q. Liu and H.-C. Han, "Mechanical buckling of artery under pulsatile pressure," *Journal of Biomechanics*, vol. 45, no. 7, pp. 1192–1198, 2012.

[36] E. Cutrì, P. Zunino, S. Morlacchi, C. Chiastra, and F. Migliavacca, "Drug delivery patterns for different stenting techniques in coronary bifurcations: a comparative computational study," *Biomechanics and Modeling in Mechanobiology*, vol. 12, no. 4, pp. 657–669, 2013.

[37] A. Sun, Z. Wang, Z. Fan et al., "Influence of proximal drug eluting stent (DES) on distal bare metal stent (BMS) in multi-stent implantation strategies in coronary arteries," *Medical Engineering & Physics*, vol. 37, no. 9, pp. 840–844, 2015.

Research Article

The Hemodynamic Effect of Enhanced External Counterpulsation Treatment on Atherosclerotic Plaque in the Carotid Artery: A Framework of Patient-Specific Computational Fluid Dynamics Analysis

Jianhang Du [1,2,3] **Guangyao Wu**,[4] **Bokai Wu**,[5] **Chang Liu**,[5] **Zhouming Mai**,[1,2] **Yumeng Liu**,[5] **Yawei Wang**,[6] **Pandeng Zhang**,[5] **Guifu Wu** [1,2,3] **and Jia Liu** [5,7]

[1]*Department of Cardiology, The Eighth Affiliated Hospital of Sun Yat-sen University, Shenzhen 518033, China*
[2]*Guangdong Innovative Engineering and Technology Research Center for Assisted Circulation (Sun Yat-sen University), Shenzhen 518033, China*
[3]*NHC Key Laboratory of Assisted Circulation (Sun Yat-sen University), Guangzhou 510080, China*
[4]*Department of Radiology, Shenzhen University General Hospital, Shenzhen 518055, China*
[5]*Laboratory for Engineering and Scientific Computing, Shenzhen Institutes of Advanced Technology, Chinese Academy of Sciences, Shenzhen 518055, China*
[6]*School of Biological Science and Medical Engineering, Beihang University, Beijing 100083, China*
[7]*Shenzhen Key Laboratory for Exascale Engineering and Scientific Computing, Shenzhen, China*

Correspondence should be addressed to Guifu Wu; wuguifu@mail.sysu.edu.cn and Jia Liu; jia.liu@siat.ac.cn

Received 7 June 2019; Revised 18 September 2019; Accepted 21 January 2020; Published 30 April 2020

Academic Editor: Panagiotis Korantzopoulos

Long-term enhanced external counterpulsation (EECP) therapy has been recommended for antiatherogenesis in recent clinical observations and trials. However, the precise mechanism underlying the benefits has not been fully clarified. To quantify the effect of EECP intervention on arterial hemodynamic environment, a framework of numerical assessment was introduced using a parallel computing algorithm. A 3D endothelial surface of the carotid artery with mild atherosclerotic plaque was constructed from images of magnetic resonance angiography (MRA). Physiologic boundary conditions were derived from images of the ultrasound flow velocity spectrum measured at the common carotid artery and before and during EECP intervention. Hemodynamic factors relating to wall shear stress (WSS) and its spatial and temporal fluctuations were calculated and analyzed, which included AWSS, OSI, and AWSSG. Measuring and computational results showed that diastole blood pressure, perfusion, and WSS level in carotid bifurcation were significantly increased during EECP intervention. Mean AWSS level throughout the model increased by 16.9%, while OSI level did not show a significant change during EECP. We thus suggested that long-term EECP treatment might inhibit the initiation and development of atherosclerotic plaque via improving the hemodynamic environment in the carotid artery. Meanwhile, EECP performance induced a 19.6% increase in AWSSG level, and whether it would influence the endothelial functions may need a further study. Moreover, the numerical method proposed in this study was expected to be useful for the instant assessment of clinical application of EECP .

1. Introduction

As a kind of noninvasive and atraumatic assisted circulation procedure, enhanced external counterpulsation (EECP) has exhibited itself to be an effective, safe, and economical therapy in clinics for the management of ischemic cardiovascular and cerebrovascular diseases in the recent decades [1–5] and has been thought providing a better choice for patients with chronic stable angina who failed to respond to standard revascularization procedures and aggressive pharmacotherapy [6].

The treatment of EECP (see Figure 1) involves the use of an EECP device to inflate and deflate a series of

FIGURE 1: EECP treatment in clinics and animal experiment [6]. The technique involves the using of a set of cuffs that are wrapped around the lower parts of the body and connected to an air compressor with tubes.

compressive cuffs wrapped around the patient's calves, lower thighs, and upper thighs. As a result, the enhanced flow perfusion is achieved from the device's propelling blood from veins of the lower body to arteries of the upper body and increases the blood supply for the important organs and the brain [7].

Long-term EECP intervention has been demonstrated in recent studies to be able to improve the endothelial functions and in turn may inhibit the generation and development of atherosclerosis lesion [8–11]. The hemodynamic effects, especially the wall shear stress variations, induced by EECP have been thought contributing the most important part of its benefits. Michaels et al. [12] confirmed that EECP treatment could significantly increase coronary artery flow determined by both Doppler and angiographic techniques. Braith et al. [10] suggested that EECP had a beneficial effect on peripheral artery flow-mediated dilation and endothelial-derived vasoactive agents. Our previous study [8] experimentally confirmed that EECP inhibits intimal hyperplasia and atherogenesis by modifying biomechanical stress-responsive gene expression. However, the actual influence of EECP intervention on wall shear stress (WSS) and its spatial and temporary fluctuations remained elusive.

It has been widely accepted that biomechanical stresses of large and medium arteries play an important role in maintaining the functions of endothelium and vascular remodeling progression [13]. Low and/or oscillating WSS has been commonly believed to be correlated positively with initiation and development of atherosclerosis [14–16]. Several hemodynamic factors have been proposed by different research groups to represent the biomechanical indicators connected to arterial functions, such as average wall shear stress (AWSS), oscillatory shear index (OSI), particle resident time (PRT), and wall shear stress gradient (WSSG).

This paper was aimed to conduct a pilot study on how the EECP treatment affects the hemodynamic environment and the important factors in carotid arterial bifurcation where the atherosclerotic lesion localizes characteristically. A numerical method-combined finite element method with *in vivo* medical imaging measurement was introduced to assess the local hemodynamic factors during EECP intervention.

2. Medical Image Acquisition and Processing

A 55-year-old coronary heart disease patient with mild carotid atheromatous plaque diagnosed (severity of stenosis was less than 20%) was enrolled to the measurement. The subject underwent the clinical protocol for carotid plaque MRI on a 3T MRI (General Electric Company, Discovery MR750). A two-element bilateral 8-channel carotid surface coil (Wk401 Jiangyin Wankang Medical Technology Co., Ltd.) was used for image acquisition.

A three-dimensional phase-contrast magnetic resonance angiography (3D Phase Contrast) sequence was performed: repetition time/echo time (TR/TE) 15.0/3.7 ms; flip angle 8°, field of view 32 cm × 32 cm, slice thickness 1.8 mm, and matrix 384 × 256. A High Resolution Three-Dimensional CUBE (computer use by engineers) T1 Weighted Imaging(HR 3D CUBE T1WI) sequence was performed as follows: repetition time/echo time (TR/TE) 575/15 ms; echo chain length (ETL) 24, slice thickness 0.8 mm, field of view 28 cm × 28 cm, and matrix 256 × 256).

3. EECP Intervention Protocol and Color Doppler Ultrasound Measurement

A short-term EECP intervention was performed using Pushikang P-ECP/TM Oxygen Saturation Monitoring Enhanced External Counterpulsation Instrument (made in Chongqing, China). The subject received a single, 45-minute session EECP treatment with the working pressure set to 0.033 MPa.

The blood velocity measurements of before EECP (rest state) and during EECP (15-25min after EECP initiated) were performed based on a Color Doppler Ultrasound System (Philip EPIQ7). (see Figure 2). The left common carotid arteries (CCA) were examined with 1.5 cm proximal to the bifurcation of the vessels. The blood velocity waveforms (see Figure 3) in cardiac cycles and before and during EECP intervention were extracted from the images of ultrasound flow velocity spectrum. Meanwhile, the diameter changes of the lumen section (see Figure 4) in cardiac cycles were extracted from images of ultrasound. The blood flow rate in cardiac cycle and perfusion in CCA could be calculated based on velocity waveforms and diameter changes.

4. 3D Reconstruction for the Endothelial Surface of the Carotid Artery

We propose a method to virtually reconstruct the endothelial surface of the carotid artery so as to visualize the carotid atheromatous plaque in 3D. The pipeline of our work is shown in Figure 5, where I_t denotes the input MR image with index t, $t = 1, 2, 3, \ldots$; P_t represents the artery endothelial boundary extracted from I_t. This pipeline consists of three main steps: image preprocessing, endothelial boundary extraction, and 3D reconstruction.

(a) (b)
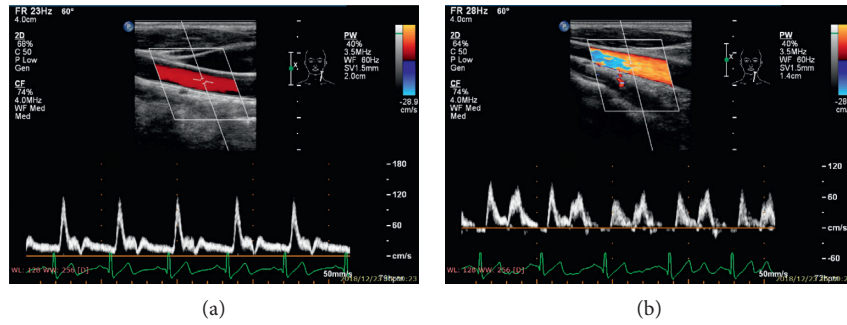
FIGURE 2: Blood flow velocity and spectrum measurement based on Color Doppler Ultrasound. (a) pre-EECP intervention. (b) During EECP intervention. Note that EECP significantly changed the blood flow pattern and increased the blood flow level in diastole.
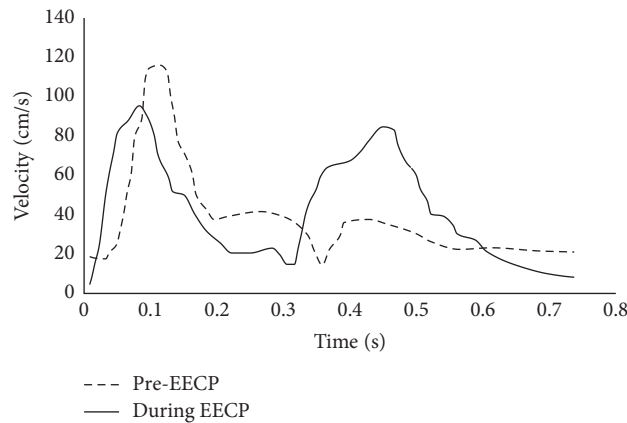
FIGURE 3: Blood velocity waveforms at CCA in a cardiac cycle before and during EECP, which were extracted from the images of ultrasound flow velocity spectrum.
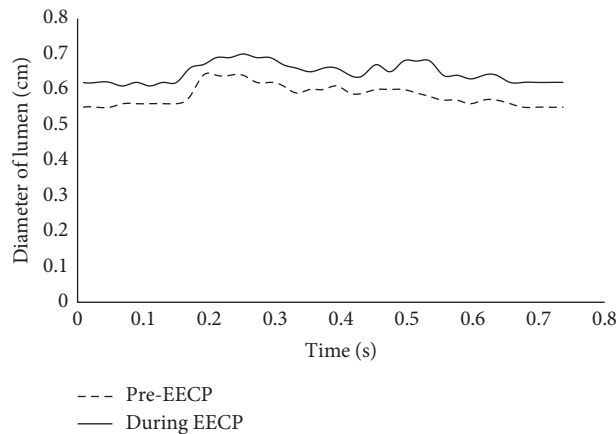
FIGURE 4: Diameter of the lumen at CCA in a cardiac cycle before and during EECP, which were extracted from the images of ultrasound carotid artery.

5. Image Preprocessing

There exists serious inherent noise in the MR image, as shown in Figure 6(a). The noise has a detrimental influence on the accuracy of the artery extraction and 3D reconstruction. In order to reduce the noise without affecting the shape of the carotid artery, we make use of the morphological technique called open-by-reconstruction and close-by-reconstruction

[17]. The processed result is illustrated in Figure 6(b). It can be seen that most of the clutters in Figure 6(a) have been removed, and the shape of the carotid artery is not influenced.

5.1. Endothelial Boundary Extraction. The extraction of the endothelial boundary of the carotid artery in each MRA image is implemented based on the result of image
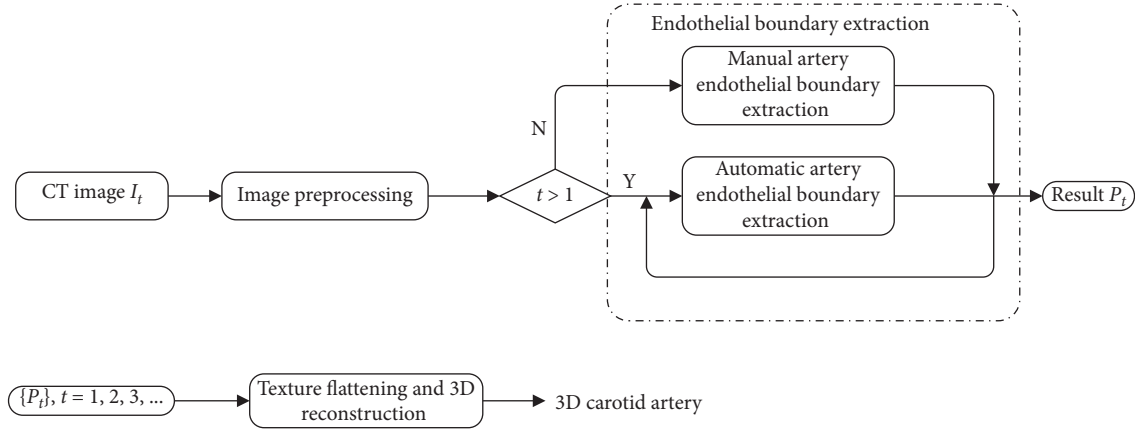
FIGURE 5: The pipeline of our algorithm.

(a)   (b)
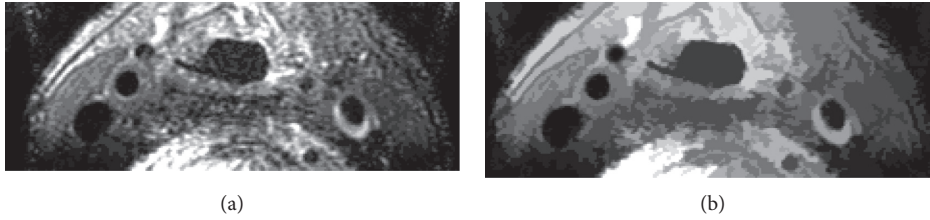
FIGURE 6: (a) The original MR image. (b) The result of morphological reconstruction.

preprocessing. For $t = 1$, we manually extract the boundary of the carotid artery in I_1, so as to initialize the subsequent automatic extraction. If $t > 1$, given the extraction result P_{t-1} (the yellow curve in Figure 7(a)),we first binarize the I_t preprocessed and then obtain the edge map E from this binary image (Figure 7(b)). Because of the great similarity between I_t and I_{t-1}, we eventually optimize a closed curve $c = [x, y]$, which satisfies the following equation with calculus of variations using P_{t-1} as the initial value.

$$\min \oint \alpha \left\| \frac{dc(s)^2}{ds} \right\| + \beta \left\| \frac{d^2 c(s)^2}{ds^2} \right\| + \gamma (1 - E(x(s), y(s)))ds, \tag{1}$$

where s is the arc parameter of c, and α, β, as well as γ are the three scalars to balance the three terms in equation (1). The optimized c is the result P_t of I_t, as shown by the yellow curve in Figure 7(c). Equation (1) can be calculated by the method proposed in [18].

5.2. Texture Flattening and 3D Reconstruction. The carotid artery can be approximately considered as a surface of revolution (SOR). Providing that the endothelial boundary of the carotid artery in each MRI slice has been extracted, the algorithm proposed in [19] can be adopted to flatten the texture of the endothelial surface of the carotid artery and then generate a 3D texture reconstruction for the endothelial surface. The carotid artery will bifurcate at its end, so we can generate the 3D texture reconstruction for each bifurcation by the same way and finally combine all reconstructions together. The final reconstruction of

the carotid artery is demonstrated in Figure 8. In this figure, the dark and concave region is the carotid atherosclerotic plaque.

6. The CFD Method and the Boundary Conditions

6.1. Geometry and Boundary Conditions. To simplify simulations, the elasticity of vessel wall is not considered in the present study (i.e., computational domain was fixed). Original geometry consists of four boundaries: inlet, outlet, and wall. An artificial extension geometry, with a length of 5 times the averaged radius of the inlet is added outward along the normal direction of the inlet boundary to acquire a fully developed velocity waveform [15], as depicted in Figure 9. Inflow velocity (V_{in}) measured by the carotid Doppler (see Figure 3) is specified at the inlet_ex. Opening condition is set at the outlet, and wall is assumed to be no-slip.

6.2. Mesh Generation. Most part of the geometry is meshed with tetrahedral cells by employing the commercial software ANSYS ICEM (ANSYS, Inc., USA). To capture the flow behavior where high velocity gradient exists, inflation layers are created near the wall [16] (as shown in Figure 10). To optimize the mesh size, a specific mesh-independent study is carried out for reliable results, while keeping computational loads as low as possible. As indicated in Table 1, change in AWSS is around 3% with refinement from Mesh 1 to Mesh 3, while less than 1% from Mesh 3 to Mesh 4 for both states with and without EECP. Mesh used in this study is of quantity 720085 (i.e., Mesh 3) and with a quality of ~0.4

(a)

(b)

(c)
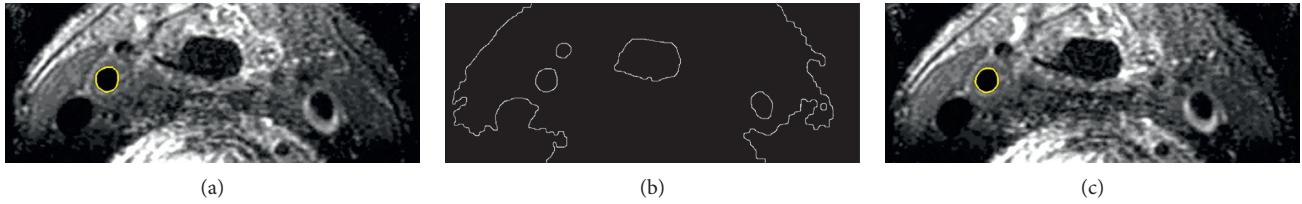
FIGURE 7: Automatic endothelial boundary extraction. (a) The result P_{t-1}. (b) The edge map of the binarized I_t. (c) The result P_t.
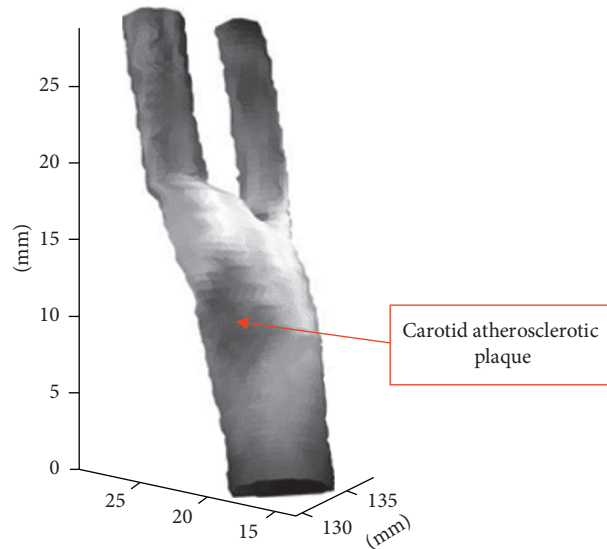
FIGURE 8: The reconstruction of the carotid artery.
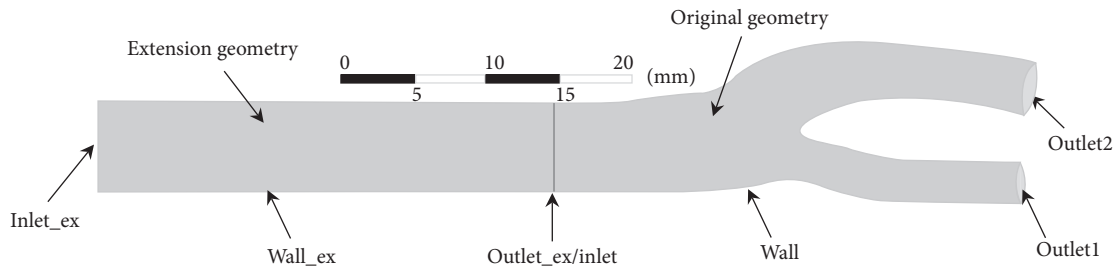
FIGURE 9: Geometry and boundaries of the carotid artery.

FIGURE 10: Schematic mesh at the inlet.

(measured by its orthogonality and warpage), which is at an acceptable level.

6.3. Rheology and Governing Equations. The blood fluid used in the present study is assumed to be impressible and iso-viscous (i.e., Newtonian type). Therefore, the governing transport equations for this study are continuity and momentum equations which can be written in their general forms [20], as follows:

$$\text{continuity: } \nabla \cdot v = 0, \tag{2}$$

$$\text{momentum: } \frac{\partial v}{\partial t} + (v \cdot \nabla)v = -\frac{1}{\rho}\nabla p + \frac{\mu}{\rho}\nabla^2 v + f, \tag{3}$$

where v is the velocity vector, p is the pressure, ρ is the fluid density, and f is the external force (assumed to be 0 here).

TABLE 1: Results of specific mesh-independent study.

	Mesh 1	Mesh 2	Mesh 3	Mesh 4
Mesh quantity	259706	419466	720085	907589
AWSS, (Pa) (pre-EECP)	7.772	7.921	7.966	7.991
AWSS, (Pa) (during EECP)	9.043	9.236	9.359	9.372
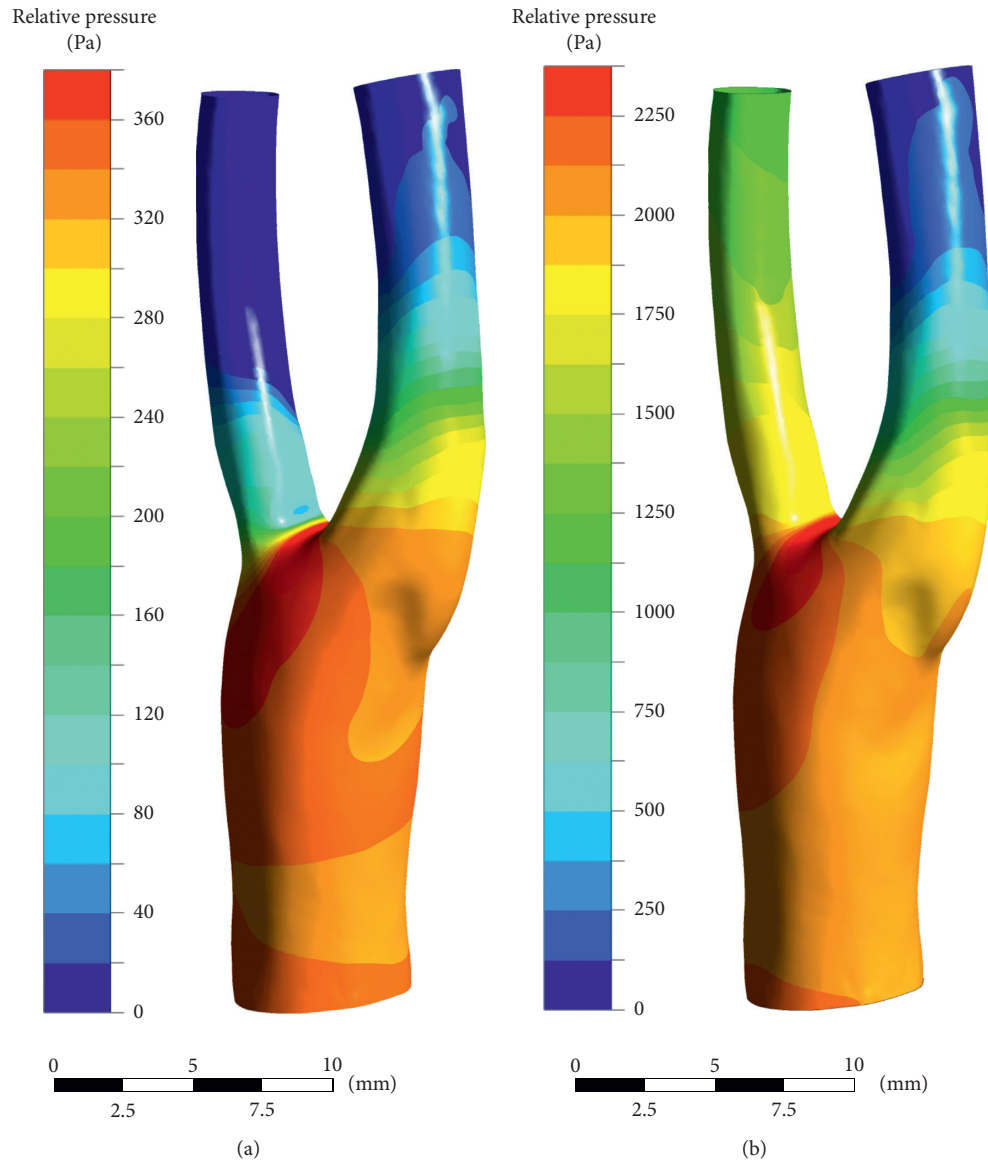
FIGURE 11: Relative blood pressure distributions in diastole. (a) Pre-EECP, $t = 0.54T$. (b) During EECP, $t = 0.58T$. Note that EECP intervention significantly increased the blood pressure in diastole.

6.4. *The solver.* The governing equations are discretized by CFX code based on a finite-volume method. To meet the requirement on both robustness and accuracy, a so-called "High Resolution Advection Scheme" is implemented in this study [21]. Numerical solutions are acquired while root mean square (RMS) of both mass and momentum residuals are below 10^{-5}. In fact, however, at most time steps, even lower RMS residual values are generally reached. We solve the unknowns with this configuration for four cardiac cycles. Results of the last cardiac cycle are presented in the following section.

7. Results

Several important hemodynamic factors such as AWSS, OSI, RRT, and WSSG were calculated in this paper, which were introduced by different research groups to represent
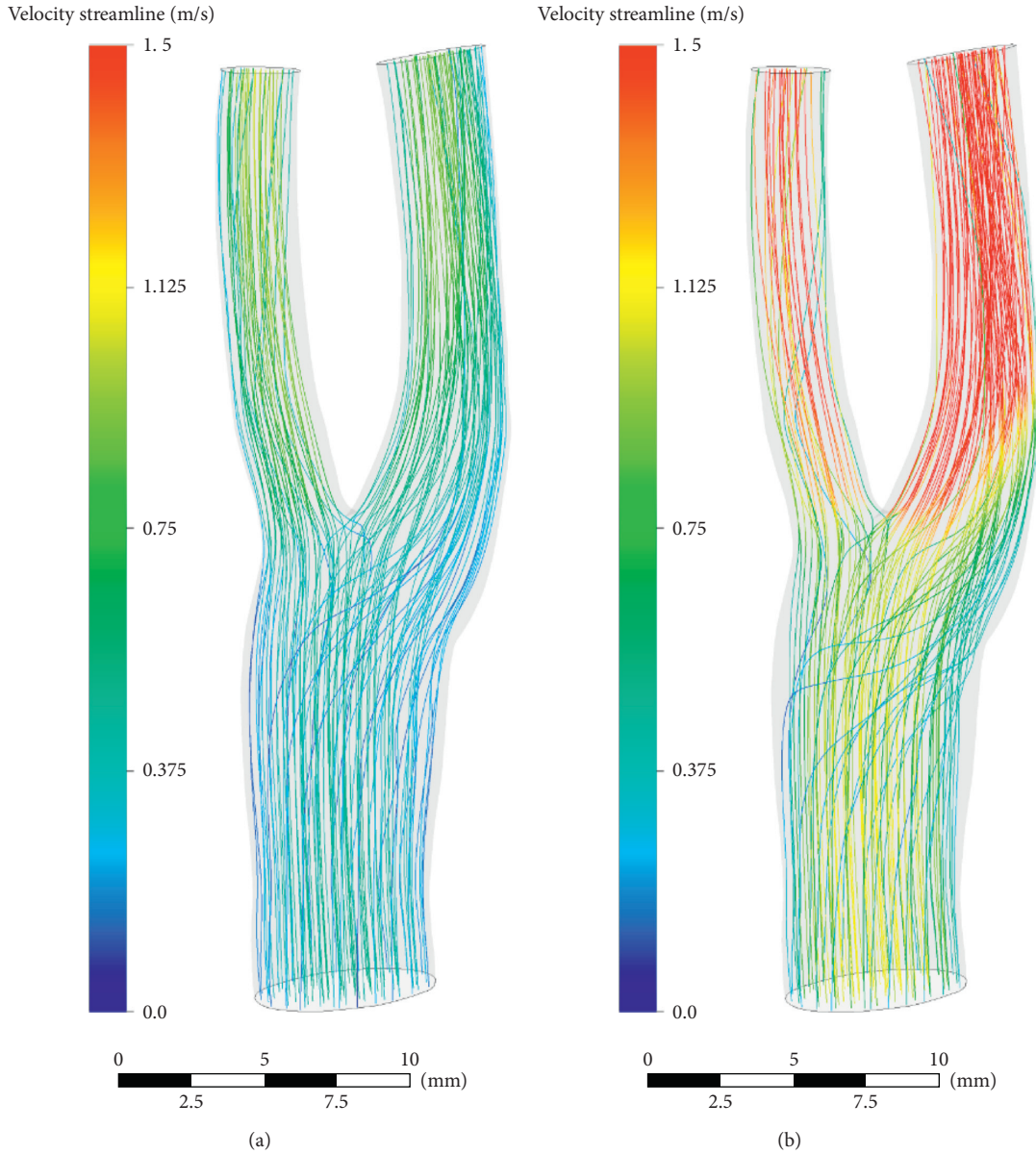
Figure 12: Blood velocity distributions in diastole. (a) Pre-EECP, $t = 0.54T$. (b) During EECP, $t = 0.58T$. Note that EECP intervention significantly increased the blood velocity in diastole.

the WSS level in a cardiac cycle and its spatial and temporary fluctuation. These factors are defined as follows [22, 23]:

$$AWSS = \frac{1}{T}\int_0^T |\vec{\tau}_w| dt, \tag{4}$$

$$\%WSSG = \sqrt{\left(\left|\frac{\partial \vec{\tau}_w}{\partial x}\right|\right)^2 + \left(\left|\frac{\partial \vec{\tau}_w}{\partial y}\right|\right)^2 + \left(\left|\frac{\partial \vec{\tau}_w}{\partial z}\right|\right)^2}, \tag{5}$$

$$\%AWSSG = \frac{1}{T}\int_0^T WSSG \, dt, \tag{6}$$

$$OSI = \frac{1}{2}\left(1 - \frac{\left|\int_0^T \vec{\tau}_w dt\right|}{\int_0^T |\vec{\tau}_w| dt}\right), \tag{7}$$

$$RRT = \frac{1}{(1 - 2OSI) \times AWSS}, \tag{8}$$

where $|\vec{\tau}_w|$ is the magnitude of the instantaneous WSS vector $\vec{\tau}_w$ and T is the cardiac cycle.

The numerical results are shown in Figures 11–15. Focus of previous studies were mainly put on how EECP affected the blood flow and pressure in diastole [1, 12]. In the current paper, the velocity and pressure at time points of $t = 0.54T$ and $t = 0.58T$ were chosen to represent the blood velocity and pressure in diastole before and during
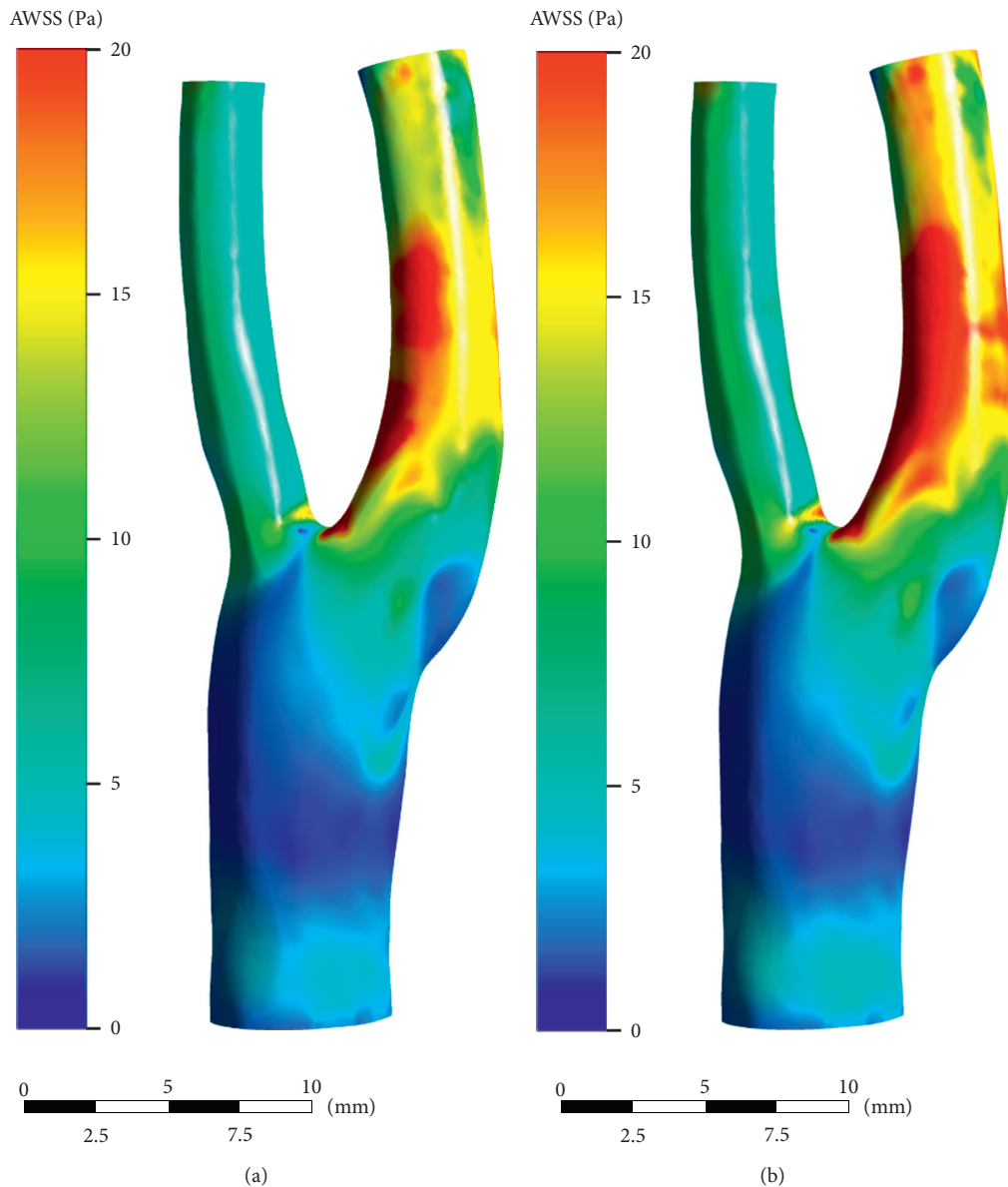
FIGURE 13: AWSS distributions over the cardiac cycle. (a) Pre-EECP. (b) During EECP. Note that high level AWSS occurred at the internal carotid artery (ICA), whereas low level AWSS occurred at bulb. EECP intervention significantly increased the AWSS level at sinus of the bifurcation.

EECP intervention respectively, considering that peak blood velocity in diastole occurred at these time points based on Figure 3.

8. Discussions

The computational results are summarized in Table 2, which include AWSS, OSI, and AWSSG over the cardiac cycle and before and during EECP intervention. All calculations and statistics were performed based on the whole model.

The results showed that EECP performance significantly increased the blood velocity in diastole, as well as the blood pressure. Peak relative pressure during EECP increased about 2260 Pa comparing to pre-EECP state. The elevation of diastolic pressure was thought playing a key

role for the increasement of perfusion [24]. A calculation based on Figures 3 and 4 showed that EECP performance induced a 12.6% elevation of the perfusion over a cardiac cycle in CCA.

WSS has been widely recognized to be an important hemodynamic factor affecting the initiation and development of atherosclerotic plaque. It is now well accepted that low and oscillating WSS correlate positively with atherosclerosis progression [25]. Our calculating results showed that EECP performance significantly increased the WSS level in carotid bifurcation and especially in bulb and ICA, and the mean AWSS level throughout the model increased by 16.9% (7.90 Pa versus 6.76 Pa).

As a factor proposed to represent the temporary fluctuation of WSS, OSI has been found to be associated
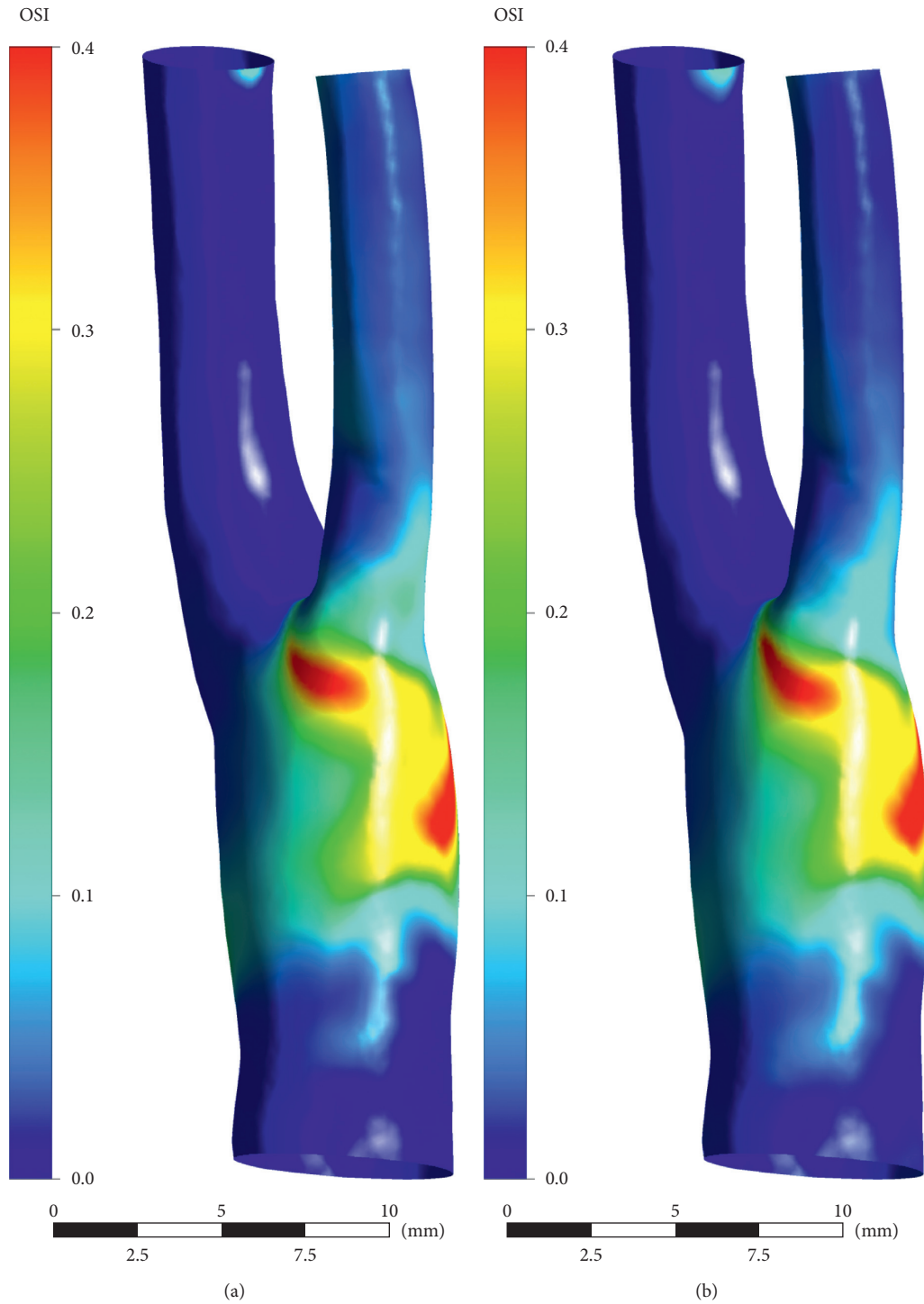
FIGURE 14: OSI distributions over the cardiac cycle. (a) Pre-EECP. (b) During EECP. Note that high level OSI occurred at bulb, and EECP intervention didn't induce significant change of OSI level.

with early atherosclerosis in some studies, and region of high OSI coincides with a high probability of occurrence of early atherosclerosis lesions [26, 27]. Our results showed that EECP performance didn't induce a significant change in OSI level in the carotid artery, although this kind of intervention greatly changed the blood flow pattern.

As a factor proposed to represent the spatial fluctuation of WSS, WSSG has been suggested in some studies that might correlate with intima-medial thickness and endothelial dysfunction [27, 28]. Our current study showed that EECP performance induced a significant increase in WSSG level in the carotid artery. The mean and peak AWSSG level throughout the model, respectively, increased by 19.6%
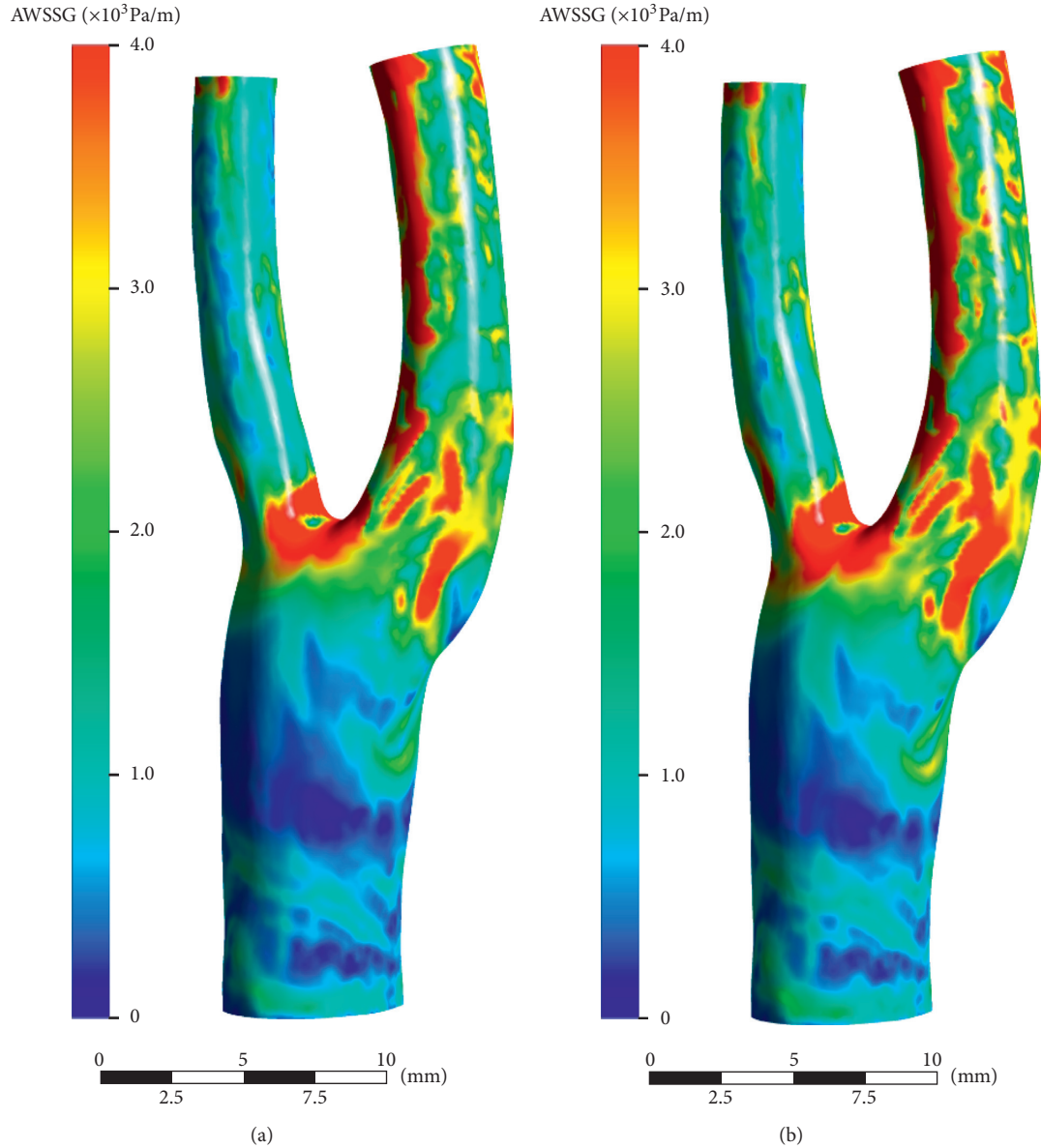
FIGURE 15: AWSSG distributions over the cardiac cycle. (a) Pre-EECP. (b) During EECP. Note that high level AWSS mainly occurred at bifurcation site and ICA. Meanwhile, EECP intervention slightly increased the AWSSG level.

TABLE 2: Hemodynamic statistics before and during EECP intervention for the whole model and over the cardiac cycle.

	AWSS (Pa)		OSI		AWSSG (Pa/m)	
	Pre-EECP	During EECP	Pre-EECP	During EECP	Pre-EECP	During EECP
Max	38.69	44.90	0.48	0.47	2.12×10^4	2.60×10^4
Min	0.73	0.70	3.2×10^{-7}	2.1×10^{-6}	93.11	97.87
Mean	6.76	7.90	0.041	0.042	1.68×10^3	2.01×10^3

$(2.01 \times 10^3 \, \text{Pa/m}$ versus $1.68 \times 10^3 \, \text{Pa/m})$ and 22.6% $(2.60 \times 10^4 \, \text{Pa/m}$ versus $2.12 \times 10^4 \, \text{Pa/m})$.

One of the main limitations in the current study was that we did not enroll healthy subjects as comparison. Because the aim of this paper was to introduce a medical imaging-based numerical method to assess the instant hemodynamic response during EECP treatment and to conduct a pilot study of the influence of EECP on WSS and its fluctuations in carotid bifurcation with mild plaque.

9. Conclusions

We suggest that the framework of patient-specific numerical approach developed in the current paper can be potentially

used in clinics for the assessment of instant hemodynamic response in the carotid artery during EECP treatment and in turn may play a role on improvement of the treatment strategies for better clinical outcome. Meanwhile, findings of this paper show that EECP treatment induced a significant augmentation of blood perfusion and WSS level in the carotid artery, which may be the main hemodynamic mechanism underlying its good clinical effect for treatment of the ischemic cerebrovascular diseases and the long-term effect for inhibition of the atherosclerosis lesion.

Data Availability

The data used to support the findings of this study are available from the corresponding author upon request.

Conflicts of Interest

The authors declare that they have no conflicts of interest.

Authors' Contributions

Jianhang Du and Guangyao Wu contributed equally to this work.

Acknowledgments

References

[1] W. Lin, L. Xiong, J. Han et al., "External counterpulsation augments blood pressure and cerebral flow velocities in ischemic stroke patients with cerebral intracranial large artery occlusive disease," *Stroke*, vol. 43, no. 11, pp. 3007–3011, 2012.

[2] W. E. Lawson, J. C. K. Hui, E. D. Kennard, and G. Linnemeier, "Enhanced external counterpulsation is cost-effective in reducing hospital costs in refractory angina patients," *Clinical Cardiology*, vol. 38, no. 6, pp. 344–349, 2015.

[3] Task Force Members, G. Montalescot, U. Sechtem et al., "2013 ESC guidelines on the management of stable coronary artery disease," *European Heart Journal*, vol. 34, no. 38, pp. 2949–3003, 2013.

[4] E. C. Jauch, J. L. Saver, H. P. Adams et al., "Guidelines for the early management of patients with acute ischemic stroke," *Stroke*, vol. 44, no. 3, pp. 870–947, 2013.

[5] S. D. Fihn, J. C. Blankenship, K. P. Alexander et al., "2014 ACC/AHA/AATS/PCNA/SCAI/STS focused update of the guideline for the diagnosis and management of patients with stable ischemic heart disease," *The Journal of Thoracic and Cardiovascular Surgery*, vol. 149, no. 3, pp. e5–e23, 2015.

[6] A. Raza, K. Steinberg, J. Tartaglia et al., "Enhanced external counterpulsation therapy: past, present, and the future," *Cardiology in Review*, vol. 25, no. 2, p. 59, 2016.

[7] J. Du and L. Wang, "Enhanced external counterpulsation treatment may intervene the advanced atherosclerotic plaque progression by inducing the variations of mechanical factors: a 3D FSI study based on in vivo animal experiment," *Molecular & Cellular Biomechanics*, vol. 12, no. 4, pp. 249–263, 2015.

[8] Y. Zhang, X. He, X. Chen et al., "Enhanced external counterpulsation inhibits intimal hyperplasia by modifying shear stress-responsive gene expression in hypercholesterolemic pigs," *Circulation*, vol. 116, no. 5, pp. 526–534, 2007.

[9] D. P. Casey, C. R. Conti, W. W. Nichols, C. Y. Choi, M. A. Khuddus, and R. W. Braith, "Effect of enhanced external counterpulsation on inflammatory cytokines and adhesion molecules in patients with angina pectoris and angiographic coronary artery disease," *The American Journal of Cardiology*, vol. 101, no. 3, pp. 300–302, 2008.

[10] R. W. Braith, C. R. Conti, W. W. Nichols et al., "Enhanced external counterpulsation improves peripheral artery flow-mediated dilation in patients with chronic angina," *Circulation*, vol. 122, no. 16, pp. 1612–1620, 2010.

[11] D.-Y. Yang and G.-F. Wu, "Vasculoprotective properties of enhanced external counterpulsation for coronary artery disease: beyond the hemodynamics," *International Journal of Cardiology*, vol. 166, no. 1, pp. 38–43, 2013.

[12] A. D. Michaels, M. Accad, T. A. Ports, and W. Grossman, "Left ventricular systolic unloading and augmentation of intracoronary pressure and Doppler flow during enhanced external counterpulsation," *Circulation*, vol. 106, no. 10, pp. 1237–1242, 2002.

[13] A. J. Brown, Z. Teng, P. C. Evans, J. H. Gillard, H. Samady, and M. R. Bennett, "Role of biomechanical forces in the natural history of coronary atherosclerosis," *Nature Reviews Cardiology*, vol. 13, no. 4, pp. 210–220, 2016.

[14] Y. Mohamied, E. M. Rowland, E. L. Bailey, S. J. Sherwin, M. A. Schwartz, and P. D. Weinberg, "Change of direction in the biomechanics of atherosclerosis," *Annals of Biomedical Engineering*, vol. 43, no. 1, pp. 16–25, 2015.

[15] X. Li, X. Liu, X. Li, L. Xu, X. Chen, and F. Liang, "Tortuosity of the superficial femoral artery and its influence on blood flow patterns and risk of atherosclerosis," *Biomechanics and Modeling in Mechanobiology*, vol. 18, no. 4, pp. 883–896, 2019.

[16] L. Xu, F. Liang, B. Zhao, J. Wan, and H. Liu, "Influence of aging-induced flow waveform variation on hemodynamics in aneurysms present at the internal carotid artery: a computational model-based study," *Computers in Biology and Medicine*, vol. 101, pp. 51–60, 2018.

[17] R. Gonzalez, R. Woods, and S. Eddins, *Digital Image Processing Using Matlab*, Publishing House of Electronics Industry, Beijing, China, 2004.

[18] P. Rosin, Y. Lai, C. Liu et al., "Virtual recovery of content from X-ray micro-tomography scans of damaged historic scrolls," *Scientific Reports*, vol. 8, no. 1, Article ID 11901, 2018.

[19] C. Liu and W. Hu, "Real-time geometric fitting and pose estimation for surface of revolution," *Pattern Recognition*, vol. 85, pp. 90–108, 2019.

[20] R. B. Bird, R. C. Armstrong, and O. Hassager, *Dynamics of Polymeric Liquids: Fluid Mechanics*, Wiley, New York, USA, 1987.

[21] S. Tian, "Wall effects for spherical particle in confined shear-thickening fluids," *Journal of Non-Newtonian Fluid Mechanics*, vol. 257, pp. 13–21, 2018.

[22] F. Rikhtegar, J. A. Knight, U. Olgac et al., "Choosing the optimal wall shear parameter for the prediction of plaque location—a patient-specific computational study in human left coronary arteries," *Atherosclerosis*, vol. 221, no. 2, pp. 432–437, 2012.

[23] C. V. Cunnane, E. M. Cunnane, and M. T. Walsh, "A review of the hemodynamic factors believed to contribute to vascular access dysfunction," *Cardiovascular Engineering and Technology*, vol. 8, no. 3, pp. 280–294, 2017.

[24] H. Mueller, S. M. Ayres, and W. J. Grace, "Hemodynamic and myocardial metabolic response to external counterpulsation in acute myocardial infarction in man," *The American Journal of Cardiology*, vol. 31, no. 1, p. 149, 1973.

[25] D. Tang, R. D. Kamm, C. Zheng et al., "Image-based modeling for better understanding and assessment of atherosclerotic plaque progression and vulnerability: data, modeling, validation, uncertainty and predictions," *Journal of Biomechanics*, vol. 47, no. 4, pp. 834–846, 2014.

[26] D. N. Ku, C. K. D. P. Giddens, and S. Glagov, "Pulsatile flow and atherosclerosis in the human carotid bifurcation. Positive correlation between plaque location and low oscillating shear stress," *Arteriosclerosis: An Official Journal of the American Heart Association, Inc,* vol. 5, no. 3, pp. 293–302, 1985.

[27] J. R. Buchanan, C. Kleinstreuer, G. A. Truskey, and M. Lei, "Relation between non-uniform hemodynamics and sites of altered permeability and lesion growth at the rabbit aorto-celiac junction," *Atherosclerosis*, vol. 143, no. 1, pp. 27–40, 1999.

[28] J. Murphy and F. Boyle, "Predicting neointimal hyperplasia in stented arteries using time-dependant computational fluid dynamics: a review," *Computers in Biology and Medicine*, vol. 40, no. 4, pp. 408–418, 2010.

Research Article

A Hypothetical Vascular Stent with Locally Enlarged Segment and the Hemodynamic Evaluation

Yudi Niu,[1] Anqiang Sun (ID),[1,2] Zixuan Wang,[1] Chenghong Yao,[1] and Juxingsi Song[1]

[1]*Key Laboratory for Biomechanics and Mechanobiology of Ministry of Education,*
 School of Biological Science and Medical Engineering, Beihang University, Beijing 100083, China
[2]*Beijing Advanced Innovation Center for Biomedical Engineering, Beihang University, Beijing 100083, China*

Correspondence should be addressed to Anqiang Sun; saq@buaa.edu.cn

Among the interventional stenting methods for treating coronary bifurcation lesions, the conventional treatments still have disadvantages, which include increased intervention difficulties or inadequate supply of blood flow to side branches and may alter the physiological function of downstream organs. Thus, the optimized design of stent geometry needs to be improved based on the specific shape of branches to minimize the complications of inadequate blood flow to the downstream organs and tissues. Our research used 3D modeling and fluid dynamics simulation to design and evaluate a new stent with locally enlarged segment by altering the proportion and length of enlarged surface area based on Bernoulli's equation. The aim is to increase the pressure and blood flow supply at side branches. According to series of blood flow simulations, the stent with 10% enlargement of surface area and length of 3 folders of stent diameter was assigned as the optimized design. The results revealed that by using this design, according to the simulation results, the average pressure on side branches increased at the rate of 43.6%, which would contribute to the adequate blood supply to the downstream organs. Besides, the average wall shear stress (WSS) at sidewalls increased at 9.2% while the average WSS on the host artery wall decreased at 14.1%. There is in the absent of noticeable rise in the total area of low WSS that blows the threshold of 0.5 Pa. Therefore, the present study provides a new method to optimize the hemodynamics features of stent for bifurcation arteries.

1. Introduction

Coronary bifurcation lesion mainly refers to the presence of larger than 50% of stenosis in the main vessel and branch vessel openings [1]. It accounts for about 15% to 20% of coronary interventional therapy [2] and have low surgical success rate [3], high risk of intraoperative occlusion during percutaneous coronary angioplasty [3, 4], as well as high rate of postoperative branch restenosis [5]. Due to its anatomical structure, there is no standard guideline for the treatment of branch lesions in clinical practice [6]. Coronary branch lesion itself is an independent risk factor for stent thrombosis after Percutaneous Coronary Intervention (PCI) [7] and has relatively low long-term intervention safety [6, 8].

Single-stent intervention is a simple treatment strategy that can significantly shorten the intervention time and complexity during clinical practice, but this oversimplified surgical approach which emphasizes the provisional stent strategy would lead to the potential decrease of blood supply [9] in side branches and finally induces occlusion, local myocardial necrosis [10], and increased perioperative myocardial infarction [11]. Thus, double-stent intervention is designed to cover the main vessels and side branches at the meantime to guarantee sufficient blood flow and avoid residual stenosis in the lateral branch. However, there are also some disadvantages for double-stent intervention strategy including incomplete coverage, vascular dissegment, high rate of thrombus and restenosis, etc. [12, 13].

Both the existing single-stent and double-stent intervention techniques have difficulties in avoiding shielding of the bifurcation vessels [14, 15], causing increased restenosis rate and insufficient blood supply to downstream organs,

which may alter the corresponding physiological functions [14].

As a result, we proposed a novel design based on Bernoulli's equation [16] (equation (1)) to simultaneously ensure the adequate blood supply to bifurcation vessel and lower risk of restenosis rate with enlarged segment at branches.

$$\frac{v^2}{2} + gz + \frac{p}{\rho} = \text{constant}, \tag{1}$$

where g is the gravitational acceleration, v is the fluid flow speed of a streamline point, z is the elevation of the point above a reference plane, p is the pressure at the targeted point, and ρ is the density of the fluid.

The above equation suggests that when the fluid velocity decreases, the fluid pressure may increase, which can improve the blood supply and avoid blockage in clinical treatment of atherosclerosis. Given consideration to that the energy difference caused by the changes of elevation in blood flow is minor and can be neglected [17, 18], it is obvious to draw the conclusion that the decrease in velocity of blood contributes to the rise of blood supply pressure and may compensate for the inadequate blood supply near branch lesions. The decrease of blood velocity may result from the enlargement of cross-segment area of vessel when the flow rate remains the same or appears in the flow stagnant zone [19] of disturbed laminar flow where Reynold's number exceeds 200 [20]. Our research is based on the theory that aims at lifting the blood supply pressure by designing enlarged segment in the vascular stent at side branches. It also provides reliable theoretical analysis and experimental data for clinical applications. At the same time, based on the single-stent intervention strategy, the operational difficulty of the existing technique would not increase the implantation difficulties. However, the potential decrease in wall shear stress should be monitored, which may augment the risk of disturbed hemodynamics pattern and atherosclerosis.

The goal of the present study is to investigate the hemodynamic improvement after the use of a stents with enlarged segment at the bifurcated vessel according to the ideal vascular models with variable controls (length and percentage of the enlarged area) through quantitative calculation of WSS and pressure to determine the optimized parameter of the vascular stent design. Finally, the ideal design has been selected based on the criteria of increased flow pressure (in the absence of abrupt decrease in wall shear stress as well) and adequate blood supply to the downstream organs.

2. Methods

Before the simulation of ideal vascular models, a series size of vascular stents without enlargement and with certain percentage of enlargement at 5%, 10%, 15%, 20%, 25%, and 30% (the clinical standard upper limit) were constructed according to the clinical data of PCI treatment [21]. With the length of the fixed expansion varied from (L (length) = D (main vessel diameter) to $L = 3D$), we explored the blood flow pressure distribution at the bifurcation vessel after stent

implantation to determine the enhancement of blood flow supply. At the same time, the average WSS at the main and branch vessels were examined and calculated to monitor the potential increased risk of atherosclerosis due to the decrease of blood flow velocity. Consequently, an optimized design is defined based on the selecting criteria of maximum increase in blood pressure and minimum decrease in WSS.

2.1. Modeling in SolidWorks. Construct a series of ideal vessel models in SolidWorks (Dassault Systemes S.A, USA) with different enlargement percentage at bifurcation at the rate of 0% to 30% with the interval of 5% and different length (L) of enlarged area at diameter (D) of 1 to 3 times of the initial value based on the clinical threshold of vascular stent design. Take the blood vessel with enlargement rate of 0% as static control in each group of different diameters. Constructed models with clarification of parts and corresponding parameters are shown in Figure 1.

To sum up, the detailed geometry parameters of stents are listed in (Tables 1 and 2). The average value above is derived from 1171 cases of clinical data of PCI treatment [21].

2.2. Meshing in ICEM CFD. ICEM (ANSYS, Inc., Canonsbury, PA, USA) software was used to generate meshes of ideal models. Mesh is generated using the Octree approach to distinguish "boundary layer," which is normally formed under nonnegligible adhesive force in blood flow. Global prism settings were assigned as: initial height 0, height growing ratio 1.1, and number of layers 5 [22]. Meshes were computed based on above settings. Mesh numbers are 413,578. The mesh of prism layer and the completed mesh of enlarged vessel model are shown in Figure 2.

2.3. Grid Independence Test. The enlarged vessel after the intervention of vascular stent with 5% enlargement at surface area and length of enlarged area at $L = D$, $L = 2D$, and $L = 3D$ meshed by the control of relevance varies from 0, 10, to 100 is calculated in Ansys Fluent to determine the pressure in Group A (average pressure between inlet and outlet 2), B (average pressure between main wall and outlet 2), and C (average pressure between main wall and sidewall). The relative error based on the set of relevance equals to 100 is calculated to figure out whether the computing results is reliable and stable with the error beneath 1.00%. The results are listed in Table 3.

Most of the relative error based on the mesh control of relevance equals to 100 is beneath the limit value of 1.00%, which further implies the reliability of the computational results in our model. Thus, relevance equals to 100 is selected as the fixed index in following mesh control.

2.4. Simulation in Ansys Fluent. Numerical simulations were performed by employing ANSYS Fluent CFD (ANSYS Inc., Canonsburg, PA). Three-dimensional, laminar, steady-state, and pulsatile flows in all the modeled (Figure 2) coronary vessel geometries were analyzed, by solving incompressible
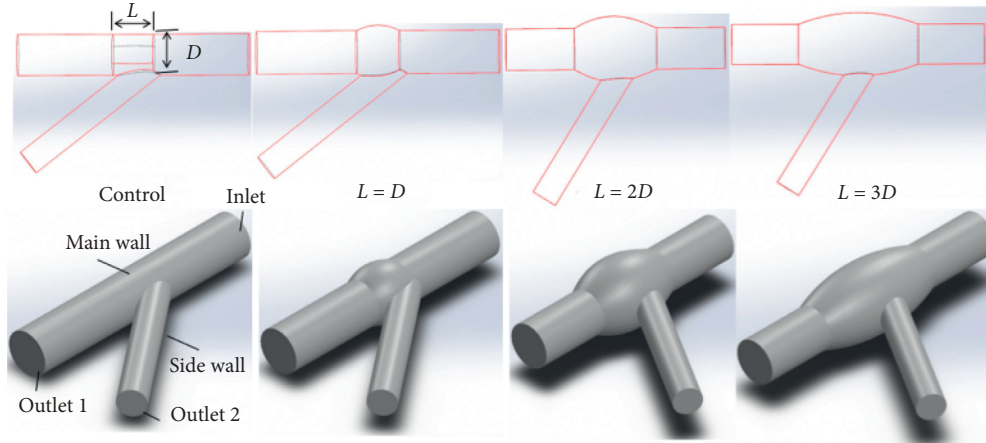
FIGURE 1: Schematic diagram of a vessel with enlarged segment at branch after the intervention of vascular stent.

TABLE 1: Geometry parameters of enlarged vessels.

Main vessel	D (mm) (from 5% to 30%)	L (mm)
Control	3	3
$L = D$	3.78/3.84/3.90/3.98/4.04/4.10	3
$L = 2D$	3.78/3.84/3.90/3.98/4.04/4.10	6
$L = 3D$	3.78/3.84/3.90/3.98/4.04/4.10	9

TABLE 2: Geometry parameters of side branches.

Side branch	Diameter (mm)	Length (mm)	Angle (°)
	1.9	10	52

continuity and Navier–Stokes equations specified in equations (2) and (3):

$$\rho\left(\frac{\partial \overrightarrow{v}}{\partial t} + (\overrightarrow{v} \cdot \nabla)\overrightarrow{v}\right) = -\nabla P + \nabla \tau, \tag{2}$$

$$\nabla \overrightarrow{v} = 0, \tag{3}$$

where $\overrightarrow{v}$ denotes the fluid velocity vector and P refers to the pressure. ρ denotes the blood density, which equals to $1050 \, \mathrm{kg/m}$,^{3} and τ denotes the stress tensor.

Set the inlet condition at the velocity of 0.36 m/s and outlet condition as "outflow," which assumes zero pressure at the outlets with 61.3% flow stream from the outlet 1 and 38.7% flow from outlet 2 based on clinical data of coronary blood flow. A pressure-based solver was incorporated with a second-order upwind computing method for momentum spatial discretization.

The residual continuity was assigned as value of 1.0×10^{-5}. Computational results of the hemodynamics parameter within initial vessel and each 6 vessels with the enlarged area length of $L = D$ to $L = 3D$ at different enlargement percentage of surface area varies from 5% to 30% at branches (in total as 19 enlarged vessels) were obtained through simulation.

2.5. Postprocessing in Ansys Fluent. Firstly, to guarantee the accuracy and reliability of the computed results, the Grid Independence Test (GIT) is done to calculate the pressure within same enlarged vessel at same location at different relevance value (respectively, are 0, 10, and 100). Relative error is calculated to examine if the computing process is independent of the meshing set, and 1.00% is chosen as the maximum limit of testifying standards towards relative error.

Secondly, due to the decrease in blood velocity, the WSS may fall below the alarming threshold at 0.5 Pa [23] that would cause atherosclerosis. Thus, the pressure at different parts (inlet, main wall, sidewall, and outlet 2) of the enlarged vessel is calculated to identify the improvement of blood supply, and the isosurface of pressure at 120 Pa is drawn to observe the existence of possible pressure concentration that may cause functional lapse of stent. Besides, WSS at different parts (main wall and sidewall) of the enlarged vessel is computed to determine the declining degree, and the isosurface of WSS at 0.5 Pa is drawn to figure out the potential risk for long-term atherosclerosis after implantation.

Thirdly, the average pressure between inlet and outlet 2 (recorded as A), the average pressure between main wall and outlet 2 (recorded as B), and the average pressure between main wall and sidewall (recorded as C) are computed and drawn in histogram to determine the superior design of stent enlargement parameters, which guarantees the maximum blood supply. The relevance of pressure fluctuation between Group A, Group B, and Group C is verified by T test.

In addition, the average WSS at main wall (recorded as E) and sidewall (recorded as F) is displayed in histogram to determine the superior design of enlargement parameters of stent with relatively higher value of WSS, which minimizes the danger of future atherosclerosis formation. The relevance of wall shear stress fluctuation between Groups E and F is verified by T test.

Finally, the optimized stent design with enlarged segment at branches to treat coronary bifurcation lesion is determined under the criteria of maximum blood pressure and WSS, minimum area of pressure concentration, and revealing limit of WSS under 0.5 Pa.
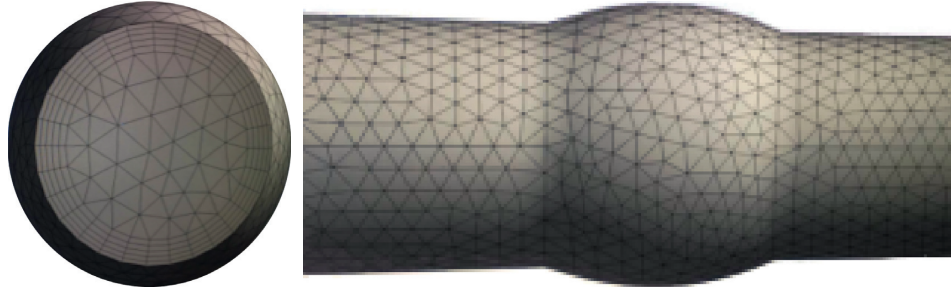
FIGURE 2: Mesh of "boundary layer" or prism layer drawn by Octree approach and mesh of enlarged vessel.

TABLE 3: Results of Grid Independence Test (GIT).

L	Relevance	A (Pa)	Error	B (Pa)	Error	C (Pa)	Error
	0	286.50	1.56%	233.86	2.29%	158.16	0.15%
$L = D$	10	289.68	0.47%	228.49	1.55%	158.39	0.11%
	100	291.05	NaN	230.22	NaN	158.32	NaN
	0	308.01	0.44%	261.99	0.15%	193.58	0.47%
$L = 2D$	10	308.01	0.44%	262.38	0.15%	193.58	0.47%
	100	309.38	NaN	262.38	NaN	194.49	NaN
	0	298.40	0.22%	254.24	0.42%	187.54	0.15%
$L = 3D$	10	297.73	0.54%	255.03	0.11%	186.83	0.53%
	100	296.79	NaN	255.32	NaN	187.82	NaN

3. Results

3.1. Pressure.
The average pressure between inlet and outlet 2 (A), main wall and outlet 2 (B), and main wall and sidewall (C) are listed in Table 4.

The distribution of pressure at side branches and main walls as well as the isosurface of pressure equals to 120 Pa is shown in Figure 3. It can be preliminarily inferred that the pressure at side branches and pressure concentration area follows the pattern that decreasing with the rising of proportion of enlarged area and the length of enlarged vessels due to lower flow speed and higher blood pressure.

In order to quantitatively analyze the enhancement of blood pressure supply at branches, the histogram of pressure in Group A, B, and C at different proportion of enlarged area at branches with length of the enlarged area varies from $L = D$ to $L = 3D$ is shown in Figure 4.

It can be roughly inferred that with the increasing of proportion of enlarged segment area and enlargement length, the average pressure between inlet and outlet 2, inlet and main wall, and main wall and sidewall correspondingly enhanced, which suggests the improvement of blood supply to downstream organs. The maximum growth ratio appears in the stent design with parameter of 10% enlargement of surface area and $L = 3D$. Meanwhile, the enlarged design at branches reduces the pressure concentration rate, which may contribute to the minimal danger of stent instability due to the exceeding of stent strength limit during balloon dilation.

The results of t-test ($\alpha = 0.01$) between pressure in Groups A, B, and C is shown in Table 5, which suggest that the fluctuating pattern of pressure between inlet and outlet 2, inlet and main wall, and main wall and sidewall has no significant statistical difference.

3.2. Wall Shear Stress.
The average WSS at main wall (E) and sidewall (F) is listed in Table 6.

The distribution of WSS at sidewall and main wall and the isosurface of WSS equals to 0.5 Pa is shown in Figure 5. It can be preliminarily inferred that the WSS at side branches decreases while the area of alarming threshold (WSS lower than 0.5 Pa, which may cause atherosclerosis) increases inevitably with the rising in proportion of enlarged area and the length of enlarged vessels due to higher blood pressure and lower flow speed (lower wall shear stress) as implied by Bernoulli's equation.

In order to quantitatively analyze the potential danger of atherosclerosis and plaque formation under the impact of decreasing WSS, the histogram of pressure in Groups E and F at different proportion of enlarged area at branches with length of the enlarged area varies from $L = D$ to $L = 3D$ is shown in Figure 6.

It can be roughly inferred that with the increasing of proportion of enlarged segment and length of enlarged main walls, the averaged WSS slightly goes down due to the declination of velocity and the area of WSS below alarming threshold, which may cause increasing danger of atherosclerosis is within controllable and reasonable levels. However, in some stent design, the value of WSS slightly goes up compared to the control group, which reduces the risk of embolism and compensates for the possible drawbacks of this design. The maximum growth ratio appears in the stent design with parameters at 30% enlargement of surface area and $L = D$ at sidewall and 10% enlargement of surface area and $L = 3D$ at main wall. Meanwhile, the enlarged design at branches inevitably increases the area of lower wall shear stress at the enlarged part but the total area of lower wall shear stress remains the same, which guarantees the stable control of potential risk of atherosclerosis.

The results of t-test ($\alpha = 0.01$) between pressure in Groups E and F are shown in Table 7, which suggest that the fluctuating pattern of wall shear stress between main wall and sidewall has no significant statistical difference.

4. Discussion

The stenting at branch arteries is currently a difficult clinical problem to handle. To solve this problem, we proposed a novel stent design with enlarged segment at side branches and incorporated hemodynamics study to evaluate the

TABLE 4: The average pressure at different locations (Groups A, B, and C).

	L = D			L = 2D			L = 3D		
	A (Pa)	B (Pa)	C (Pa)	A (Pa)	B (Pa)	C (Pa)	A (Pa)	B (Pa)	C (Pa)
Control	277.7	216.6	142.4	277.7	216.6	142.4	277.7	216.6	142.4
5%	291.1	233.9	158.2	309.4	262.0	194.5	298.4	255.3	187.8
10%	294.3	236.9	160.2	321.0	271.2	202.1	255.1	310.8	227.0
15%	295.5	238.1	161.1	329.3	277.1	277.1	311.9	266.5	196.3
20%	296.7	238.7	162.6	334.2	282.0	282.0	316.0	271.0	198.4
25%	300.0	242.0	164.6	345.6	290.3	290.3	321.2	275.0	202.6
30%	303.3	244.8	167.4	351.3	295.1	295.1	330.8	281.0	207.9
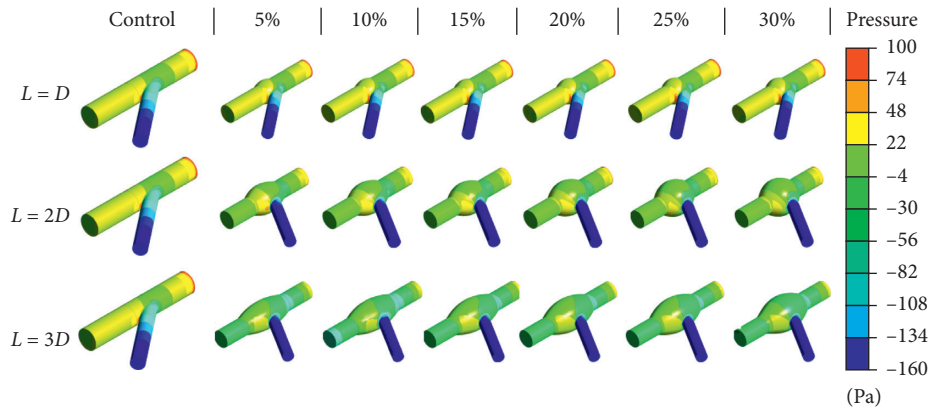
(a)
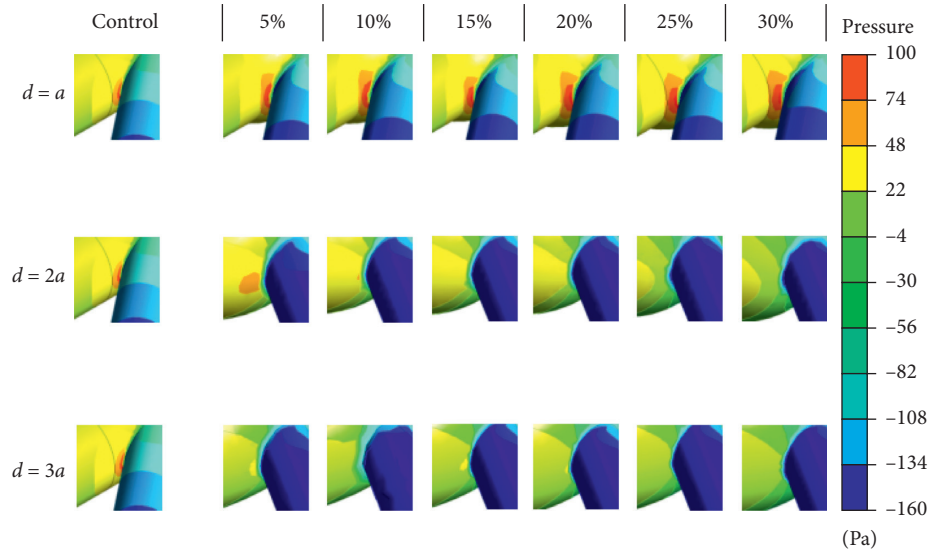
(b)

FIGURE 3: Continued.
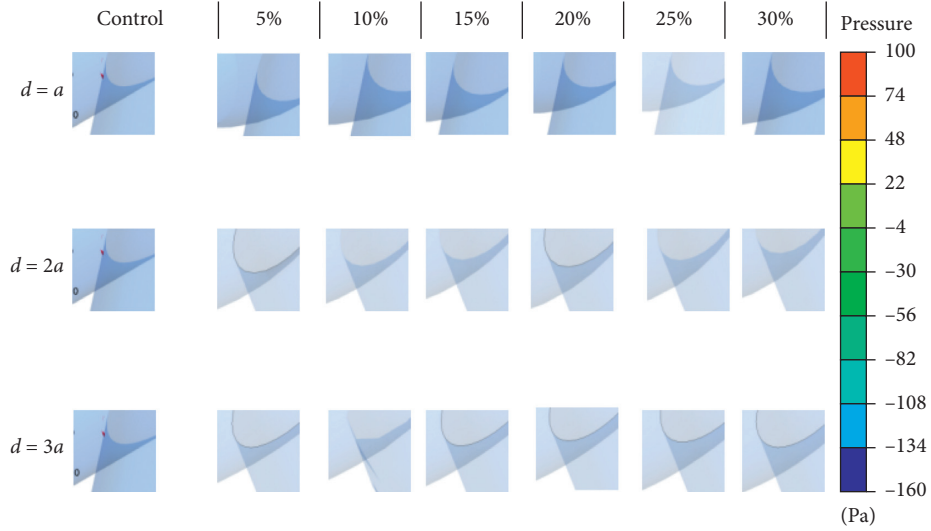
(c)

FIGURE 3: Pressure distribution. (a) Pressure distribution on the entire vessel. (b) Larger image of pressure distribution at the side branches and main walls. (c) Larger image of pressure distribution at the isosurface of pressure equals to 120 Pa.
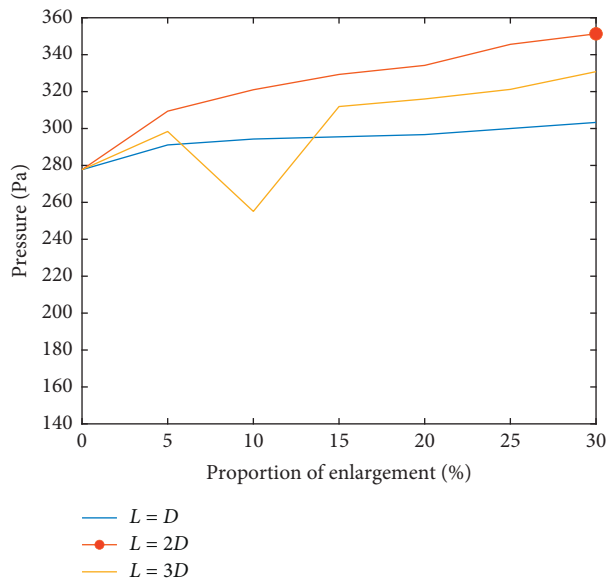
(a)
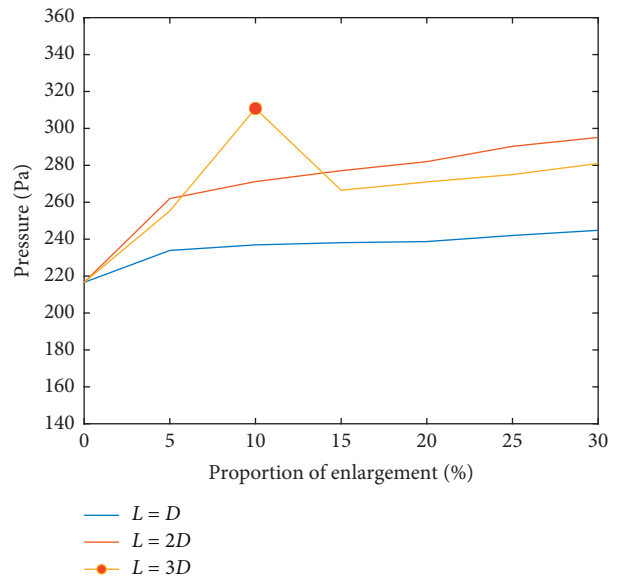
(b)

FIGURE 4: Continued.

(c)
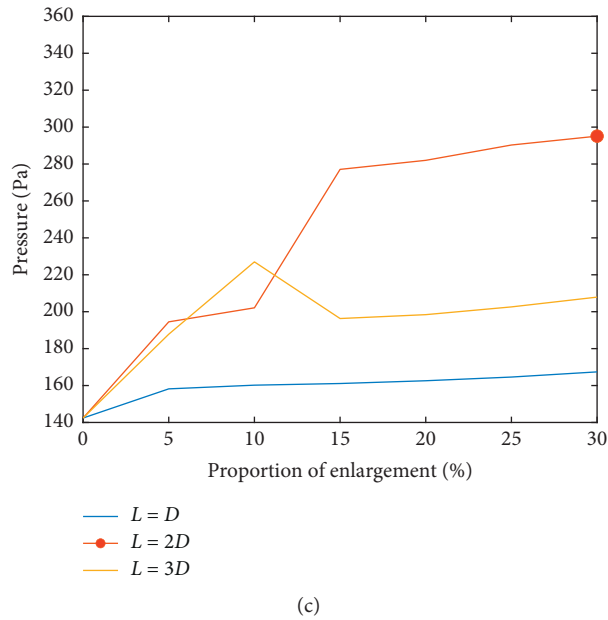
FIGURE 4: Pressure distribution (A, B, and C each shows pressure of different locations after implantation of enlarged vessels with different length of enlarged area varies from $L = D$ to $L = 3D$, the maximum pressure value within each group is marked by red circle). (a) Pressure (A). (b) Pressure (B). (c) Pressure (C).

TABLE 5: Individual T test results between Groups A, B, and C ($H = 1$ suggests the close interrelationship within pressure fluctuating pattern).

	$L = D$			$L = 2D$			$L = 3D$		
	AB	BC	CA	AB	BC	CA	AB	BC	CA
H	1	1	1	1	1	1	1	1	1
P	$3.09e-08$	$1.32e-09$	$8.58e-13$	$2.10e-03$	$3.73e-04$	$1.33e-06$	$5.50e-03$	$2.94e-04$	$1.12e-06$

TABLE 6: Raw data of average wall shear stress at different locations (Groups E and F).

	$L = D$		$L = 2D$		$L = 3D$	
	E (Pa)	F (Pa)	E (Pa)	F (Pa)	E (Pa)	F (Pa)
Control	2.42	6.54	2.42	6.54	2.42	6.54
5%	2.44	6.42	2.65	6.27	2.04	6.26
10%	2.49	6.45	2.67	6.39	2.06	7.14
15%	2.52	6.44	2.65	6.32	2.04	6.62
20%	2.57	6.38	2.55	6.46	1.99	6.78
25%	2.62	6.40	2.53	6.54	1.96	6.81
30%	2.68	6.41	2.46	6.68	2.03	6.84

hypothetical design. The results showed that the stent with enlarged segment improves blood supply pressure at side branches and enhances WSS at side branches. Meanwhile, the artery after implantation is in the absence of noticeable decrease in WSS at enlarged segment, and the pressure concentration problems at side branches are reduced due to the "Cushion" formed by the curvature segments. As a result, the hypothetical design guarantees adequate blood supply to side branches and minimal possibilities of atherosclerosis formation or blood blockage, ensuring the intervention stability during dilation with decreased pressure concentration.

The theoretical basis of the stent design in the present study is Bernoulli's equation, which is the fundamental energy conservation equation that applied to various research fields [24]. For instance, the wings of planes are designed as streamline structure to form levitated pressure with velocity on the bottom lower than the top [24, 25]. In the present study, we applied the energy conservation law to alter the partial segment shape of stent in order to enhance the perfusion pressure to side branches, which eliminates the adverse effects on physiological functions of downstream organs. The research results proved the accuracy and practical value of the hypothesis and are of significance to

(a)

(b)

(c)
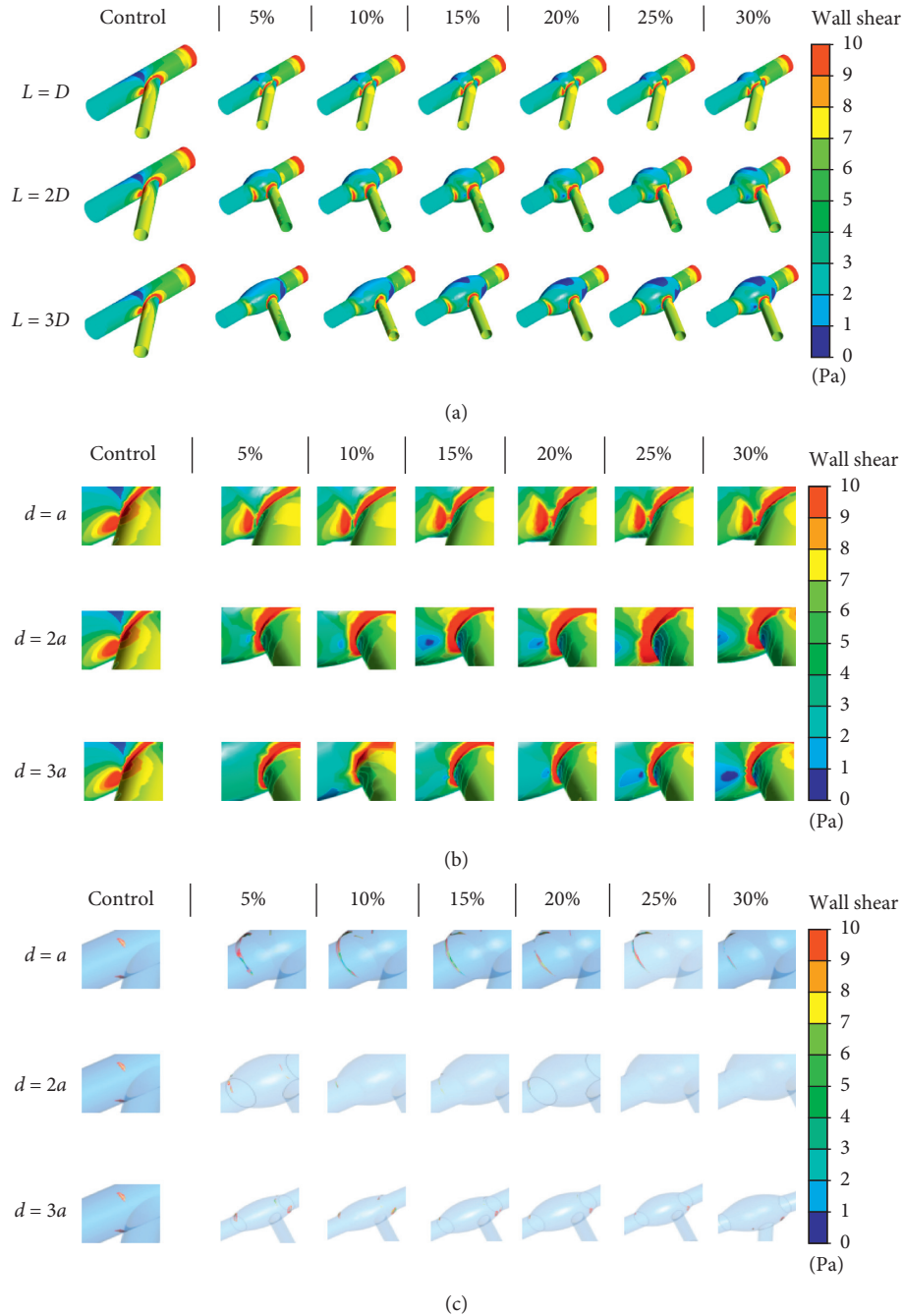
Figure 5: Wall shear stress distribution. (a) Wall shear stress distribution on the entire vessel. (b) Wall shear stress distribution at side branches and main walls. (c) Wall shear stress distribution on the side branches and main walls on isosurfaces at wall shear stress equals to 0.5 Pa.

future stent design and intervention treatments of coronary branch lesions. The varying flow resistance at distal coronary artery can be taken into consideration in the future research and simulation to achieve more accurate estimation of pressure increase among specific patients.

To sum up, the lifted pressure at side branches, decreased distribution area of pressure concentration, and decreased wall shear stress within controllable level have rewarding clinical significance. Adequate blood supply at side branches is guaranteed, and stability of stent intervention is improved

due to the pressure changes. Meanwhile, minimum decrease of wall shear stress on main enlarged walls and lifted wall shear stress after stent implantation may reduce the risk of atherosclerosis formation and restenosis rate.

Prior to future clinical applications, the hypothetical design can be further improved in materials and structural design like geometry shape of connecting ribs to obtain higher successful implantation rate, guaranteeing stent stability after balloon dilation, and minimizing the potential long-term risk caused by plaque shift and carinal shift.

(a)

(b)
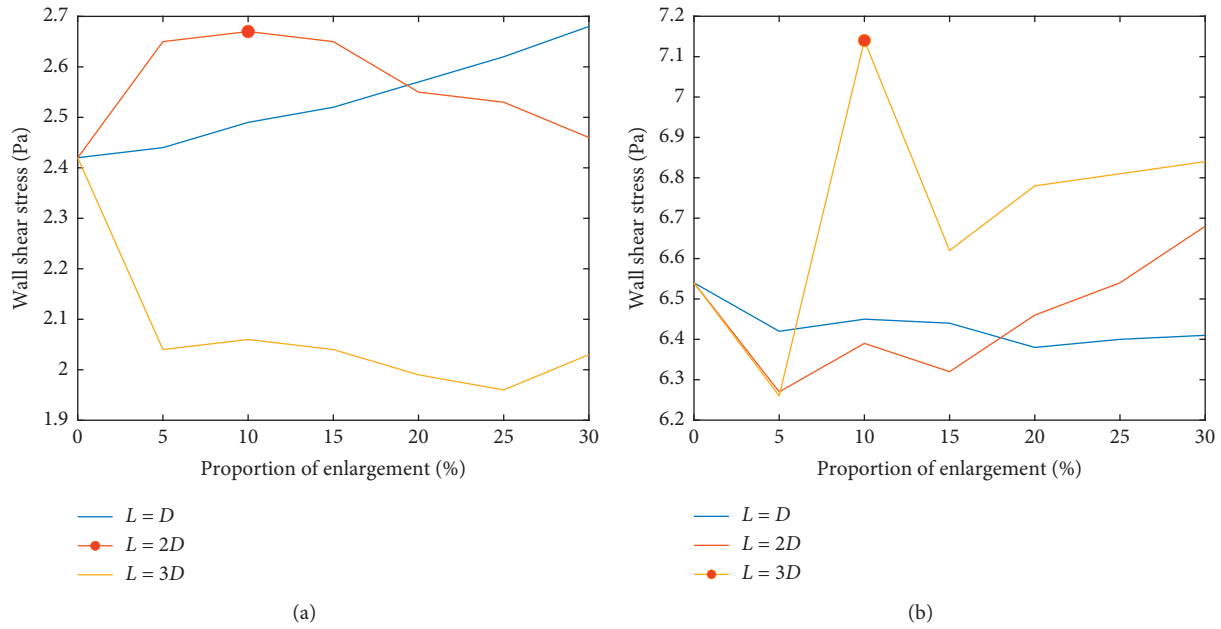
FIGURE 6: Wall shear stress distribution (E, F each shows wall shear stress at different locations of enlarged vessels with different length of enlarged area varies from $L = D$ to $L = 3D$, the maximum wall shear stress value at main wall and sidewall is marked by red circle). (a) Wall shear stress (E). (b) Wall shear stress (F).

TABLE 7: Individual T test results between Groups E and F ($H = 1$ suggests the close interrelationship within wall shear stress fluctuating pattern).

	$L = D$ EF	$L = 2D$ EF	$L = 3D$ EF
H	1	1	1
P	$1.19e - 18$	$3.42e - 16$	$5.58e - 14$

4.1. Limitations. As a preliminary study, we adopted idealized models to investigate the practical value of using stent with enlarged segment to treat coronary branch lesions while the vessel structure in vivo is of irregularity and individual difference. Meanwhile, the set of rigid vessel wall condition in simulation is different from the *in vivo* situation. But as a preliminary study, we are aiming at eliminating the impact brought by the individual difference to validate the accuracy of our hypotheses at universal level. Future studies will be focusing on designing personalized stent structure based on different vessel locations, different anatomical structures of arteries, and different narrowed type for branch lesions.

5. Conclusion

The results have practical value for solving the shortcomings of existing single-stent or double-stent intervention strategy. Firstly, the enhanced single-stent technique can significantly reduce the implantation difficulty of double-stent technique, ensuring that the stents fit snugly against the vessel wall without changing the initial shape of the branched vessel as well as reducing the risk of reformation of the plaque. Meanwhile, the enlarged design at side branches based on the principle of Bernoulli's equation can theoretically improve the blood flow pressure by reducing the blood flow velocity to increase inadequate blood supply at the bifurcation artery, preventing the sharp decrease in wall shear stress, and contributing to the decrease in pressure distribution, which guarantees the stable implantation of stents and possibly leads to the reduction in restenosis rate.

Data Availability

The hemodynamic simulation data used to support the findings of this study are included within the article.

Conflicts of Interest

The authors have no conflicts of interest to declare.

Acknowledgments

References

[1] L. Thuesen, T. Steigen, and A. Erglis, "Randomized study on simple versus complex stenting of coronary artery bifurcation lesions: 5-year follow-up in the Nordic Bifurcation Study," in *Proceedings of the Annual Meeting of the American College of Cardiology*, New Orleans, LA, USA, April 2011.

[2] G. Stankovic, T. Lefèvre, A. Chieffo et al., "Consensus from the 7th European bifurcation club meeting," *EuroIntervention*, vol. 9, no. 1, pp. 36–45, 2013.

[3] A. Colombo, A. Gaglione, S. Nakamura, and L. Finci, ""Kissing" stents for bifurcational coronary lesion," *Catheterization and Cardiovascular Diagnosis*, vol. 30, no. 4, pp. 327–330, 1993.

[4] R. W. Yeh, D. J. Kereiakes, P. G. Steg et al., "Lesion complexity and outcomes of extended dual antiplatelet therapy after percutaneous coronary intervention," *Journal of the American College of Cardiology*, vol. 70, no. 18, pp. 2213–2223, 2017.

[5] T. Miyoshi, K. Osawa, and H. Ito, "Coronary lesion characteristics influencing diagnostic accuracy of fractional flow reserve computed from ct in clinical practice," *Journal of the American College of Cardiology*, vol. 67, no. 13, p. 1675, 2016.

[6] T. Mäkikallio, N. R. Holm, M. Lindsay et al., "Percutaneous coronary angioplasty versus coronary artery bypass grafting in treatment of unprotected left main stenosis (NOBLE): a prospective, randomised, open-label, non-inferiority trial," *The Lancet*, vol. 388, no. 10061, pp. 2743–2752, 2016.

[7] H. von Korn, V. Stefan, R. van Ewijk et al., "Treatment of coronary bifurcation lesions: stent-covering of the side branch with and without PCI of the side branch: a retrospective analysis of all consecutive patients," *BMC Cardiovascular Disorders*, vol. 13, no. 1, p. 27, 2013.

[8] M. Maeng, N. R. Holm, A. Erglis et al., "Long-term results after simple versus complex stenting of coronary artery bifurcation lesions," *Journal of the American College of Cardiology*, vol. 62, no. 1, pp. 30–34, 2013.

[9] N. Sakamoto, Y. Hoshino, H. Mizukami et al., "Intravascular ultrasound predictors of acute side branch occlusion in coronary artery bifurcation lesions just after single stent crossover," *Catheterization and Cardiovascular Interventions*, vol. 87, no. 2, pp. 243–250, 2016.

[10] Y. Hikichi, M. Umezu, K. Node, and K. Iwasaki, "Reduction in incomplete stent apposition area caused by jailed struts after single stenting at left main bifurcation lesions: micro-CT analysis using a three-dimensional elastic bifurcated coronary artery model," *Cardiovascular Intervention and Therapeutics*, vol. 32, no. 1, pp. 12–17, 2017.

[11] A. Colombo, G. Stankovic, D. Orlic et al., "Modified T-stenting technique with crushing for bifurcation lesions: immediate results and 30-day outcome," *Catheterization and Cardiovascular Interventions*, vol. 60, no. 2, pp. 145–151, 2003.

[12] K. Nakabayashi, D. Sunaga, N. Kaneko et al., "Simple percutaneous coronary interventions using the modification of complex coronary lesion with excimer laser," *Cardiovascular Revascularization Medicine*, vol. 20, no. 4, pp. 293–302, 2019.

[13] C. K. Batchelor and G. K. Batchelor, *An Introduction to Fluid Dynamics*, Cambridge University Press, Cambridge, UK, 1967.

[14] I. Slottosch, O. Liakopoulos, E. Kuhn et al., "Outcome after coronary bypass grafting for coronary complications following coronary angiography," *Journal of Surgical Research*, vol. 210, pp. 69–77, 2017.

[15] P. W. Serruys, M.-C. Morice, A. P. Kappetein et al., "Percutaneous coronary intervention versus coronary-artery bypass grafting for severe coronary artery disease," *New England Journal of Medicine*, vol. 360, no. 10, pp. 961–972, 2009.

[16] R. Mulley, *Flow of Industrial Fluids: Theory and Equations*, CRC Press, Boca Raton, FL, USA, 2004.

[17] A. W. Wood, *Physiology, Biophysics, and Biomedical Engineering*, Taylor & Francis, Didcot, UK, 2016.

[18] N. Tomizawa, K. Yamamoto, S. Inoh, T. Nojo, and S. Nakamura, "Simplified Bernoulli formula to predict flow limiting stenosis at coronary computed tomography angiography," *Clinical Imaging*, vol. 51, pp. 104–110, 2018.

[19] K. Perktold and D. Hilbert, "Numerical simulation of pulsatile flow in a carotid bifurcation model," *Journal of Biomedical Engineering*, vol. 8, no. 3, pp. 193–199, 1986.

[20] F. Berntsson, M. Karlsson, V. Kozlov, and S. A. Nazarov, "A one-dimensional model of viscous blood flow in an elastic vessel," *Applied Mathematics and Computation*, vol. 274, pp. 125–132, 2016.

[21] Q. Liu, D. Zhang, H. Yang et al., "Influence of bifurcation angle to blocked side branches in PCI," *Chinese Vascular Magazine*, vol. 31, no. 2, pp. 108–112, 2016.

[22] P. Zhang, A. Sun, F. Zhan, J. Luan, and X. Deng, "Hemodynamic study of overlapping bare-metal stents intervention to aortic aneurysm," *Journal of Biomechanics*, vol. 47, no. 14, pp. 3524–3530, 2014.

[23] L. Boussel, V. Rayz, C. McCulloch et al., "Aneurysm growth occurs at region of low wall shear stress," *Stroke*, vol. 39, no. 11, pp. 2997–3002, 2008.

[24] R. C. Nelson, *Flight Stability and Automatic Control*, Vol. 2, WCB/McGraw Hill, New York, NY, USA, 1998.

[25] H. S. Badeer, "Elementary hemodynamic principles based on modified Bernoulli's equation," *Physiologist*, vol. 28, pp. 41–46, 1985.

Research Article

Profile of Endothelin-1, Nitric Oxide, and Prostacyclin Levels in Pulmonary Arterial Hypertension Related to Uncorrected Atrial Septal Defect: Results from a Single Center Study in Indonesia

Lucia Kris Dinarti ®,[1] Anggoro Budi Hartopo ®,[1] Dyah Wulan Anggrahini,[1] Ahmad Hamim Sadewa,[2] Budi Yuli Setianto,[1] and Abdus Samik Wahab[1,3]

[1]*Department of Cardiology and Vascular Medicine, Faculty of Medicine, Public Health and Nursing,*
 Universitas Gadjah Mada–Dr. Sardjito Hospital, Yogyakarta, Indonesia
[2]*Department of Biochemistry, Faculty of Medicine, Public Health and Nursing, Universitas Gadjah Mada, Yogyakarta, Indonesia*
[3]*Department of Child Health, Faculty of Medicine, Public Health and Nursing, Universitas Gadjah Mada–Dr. Sardjito Hospital,*
 Yogyakarta, Indonesia

Correspondence should be addressed to Lucia Kris Dinarti; kris_dinarti@ugm.ac.id

Background and Objectives. Pulmonary arterial hypertension (PAH) pathomechanism involves an increased plasma level of endothelin-1 and a reduced plasma level of prostacyclin and nitric oxide. Whether similar mechanisms prevail in PAH associated with atrial septal defect (ASD) is unclear. This study aimed to investigate the relationship of endothelin-1, prostacyclin, and nitric oxide with PAH in uncorrected ASD in Indonesian population. *Methods.* The study design was cross-sectional. The subjects were adult uncorrected secundum ASD with PAH. Pulmonary artery pressure was measured with right heart catheterization. Pulmonary venous blood was obtained during catheterization for measuring endothelin-1, prostacyclin, and nitric oxide. Correlation tests were performed to determine any association between biomarkers and mean pulmonary artery pressure (mPAP). The levels of biomarkers were compared based on the severity of PAH. Statistical significance was determined at $p < 0.05$. *Results.* Forty-four subjects were enrolled in this study. Endothelin-1 level and mPAP had significant moderate positive correlation ($r = 0.423$ and p value = 0.004). However, no significant correlation was observed between prostacyclin, nitric oxide levels, and mPAP. The pattern of endothelin-1, prostacyclin, and nitric oxide was distinctive. Levels of endothelin-1 were incrementally increased from mild, moderate, to severe PAH. The levels of prostacyclin and nitric oxide had similar pattern in association with the severity of PAH, which was increased in mild-to-moderate PAH but decreased in severe PAH. *Conclusions.* There was a distinctive pattern of endothelin-1, prostacyclin, and nitric oxide based on severity of PAH in adult uncorrected ASD. Significant correlations existed between endothelin-1 and the severity of PAH and mPAP.

1. Introduction

Pulmonary arterial hypertension (PAH) is an increase in mean pulmonary artery pressure (mPAP) exceeding 25 mmHg at rest with normal pulmonary artery wedge pressure (PAWP) and elevated pulmonary vascular resistance (PVR) by more than 3 Wood units, owing to the restriction in pulmonary vascular flow [1]. The pathomechanisms of PAH involve pulmonary vascular modification, i.e., intimal endothelial dysfunction, reduced apoptosis, and proliferation ratio of pulmonary artery smooth muscle cells in medial layers, and increased adventitial thickening [2]. These vascular changes produce vasoactive agents to facilitate pulmonary blood flow through pulmonary tissue. Increased production of vasoconstrictor agents, such as endothelin-1 and thromboxane, as well as a decreased production of vasodilator agents, such as prostacyclin and nitric oxide, are hallmarks of PAH [3].

Compared to idiopathic PAH, the dynamics of vasoactive biomarkers may have a different pattern in conditions with chronically elevated pulmonary flow, such as in congenital heart disease (CHD).

CHD with left-to-right shunt may cause PAH. The prevalence of PAH among CHD is varied and influenced by defect size and location [4]. Atrial septal defect (ASD) is a pretricuspid shunt which causes pulmonary blood overflow and leads to endothelial dysfunction and pulmonary vascular modification [5]. In uncorrected ASD, the functional disturbance precedes the anatomical defect of pulmonary vasculatures; therefore, PAH may develop later in adulthood [5]. Among CHD with left-to-right shunt and PAH, the proportion of ASD as the underlying defect is 30%, many of which is secundum ASD [6]. Unfortunately, secundum ASD is also the most commonly encountered CHD in adults, largely due to being undiagnosed in childhood.

Three main pathophysiological pathways have been recognized as the major components in the development of PAH, i.e., endothelin-1, nitric oxide, and prostacyclin pathways [7]. Interactions among these pathways influence the development and progression of PAH. However, the role and the dynamics of their vasoactive components in secundum ASD-associated PAH remain to be elucidated. The proposed mechanism of functional and anatomical disturbances of physiological pathways in PAH requires corroboration in the context of uncorrected secundum ASD-associated PAH. The study aimed to investigate the relation between vasoactive agents, such as endothelin-1, nitric oxide, and prostacyclin plasma levels, and severity of PAH in adult patients with uncorrected secundum ASD.

2. Methods

2.1. Subjects. We conducted a cross-sectional study using the COngenital HeARt Disease in adult and Pulmonary Hypertension Registry of Universitas Gadjah Mada, Dr. Sardjito Hospital, Yogyakarta, Indonesia (COHARD-PH Registry). The pilot study of this registry had been published elsewhere [8].

The inclusion criteria for the current study were as follows: (1) male and female patients aged ≥ 18 years old, (2) patients newly diagnosed with large secundum ASD (diameter of defect ≥ 20 mm), (3) patients diagnosed with PAH by right heart catheterization (RHC), and (4) patients gave informed consent to participate in the study. The exclusion criteria were as follows: (1) patients had underwent ASD closure (device or surgery), (2) patients have been treated with specific PAH medication, (3) patients with comorbidities, such as other CHDs, significant (moderate to severe) valvular heart disease (VHD), and chronic lung/respiratory disease, and (4) patients with creatinine level >2.0 mg/dL.

Patients gave informed consent and were enrolled consecutively. Transthoracal echocardiography (TTE) and transesophageal echocardiography (TOE) were conducted in the echo-lab of Dr. Sardjito Hospital to diagnose large secundum ASD, estimate probability of PH, and exclude other CHD(s) and VHD(s). Physical examination and chest

X-ray excluded patients with chronic lung/respiratory disease, such as chronic obstructive pulmonary disease, intermittent/persistent asthma bronchial, bronchiectasis, and pulmonary tuberculosis. Pulse oximetry measured peripheral O_2 saturation. Patients fulfilling research criteria were sent for right heart catheterization (RHC) procedure in the cath-lab of Dr. Sardjito Hospital to diagnose PAH and measure hemodynamic parameters. This study was approved by the Medical and Health Research Ethics Committee of the Faculty of Medicine Universitas Gadjah Mada, Dr. Sardjito Hospital.

2.2. Procedures. Experienced sonographer performed the TTE using Vivid 7GE (G.E. Healthcare, U.S.A). Two cardiology consultants validated the TTE results. Two-dimensional echocardiography was performed according to standard practice. Heart chamber dimension, right and left ventricular function, defect diameter and type, and flow direction were measured based on standard procedures [9]. Estimated right ventricle systolic pressure (RVSP) was calculated based on the summation of Doppler spectral tricuspid valvular regurgitant gradient (TVRG) and estimated right atrial pressure, which was calculated from inferior vena cava diameter and its collapsibility index [10].

Cardiology consultants examined the diameter, type, and size of the defect, anatomy of ASD, and concomitant CHDs or VHDs by TOE using Vivid 7GE (G.E. Healthcare, U.S.A). The cardiologist consultants had >80% agreement in interpreting the TTE and TOE results.

Patients underwent RHC in the cath-lab operated by cardiology consultant using Xper Cardio Physiomonitoring System 5 (Philips, The Netherlands). Following aseptic preparation and anesthetic application, multipurpose catheter was inserted into the right femoral vein to the right atrium via inferior vena cava and proceeded into the left atrium by crossing through the ASD and was placed in the pulmonary veins. The Swan-Ganz catheter was inserted into right femoral veins through the right atrium and into the right ventricle and was placed in the pulmonary arteries. Pressure and oxygen saturation (Avoximeter R 1000E, U.S.A) were measured in each of the cardiac chambers, great arteries, and veins in accordance with standard procedures. The mPAP and PAWP were measured with Swan-Ganz catheter. PAH was defined as mPAP value ≥ 25 mmHg, PAWP value < 15 mmHg, and PVR >3 Wood units. Cardiac output measurement was calculated using indirect Fick method based on estimated oxygen consumption per square body surface area [11]. The PVR and flow ratio were calculated with the standard formula [11]. Severity of PAH was arbitrarily grouped based on mPAP, i.e., mPAP 25–40 mmHg as mild PAH, mPAP 41–60 mmHg as moderate PAH, and mPAP >60 mmHg as severe PAH.

2.3. Blood Examination. Prior to RHC, the peripheral venous blood sample was collected to measure haemoglobin, hematocrit, and creatinine levels. The measurements were performed in the hospital central laboratory using the standard protocol. During RHC, blood samples from

pulmonary veins were collected into EDTA-containing polypropylene tubes. The sample was left in room temperature for 30 min and centrifuged at 4000 r.p.m for 10 min at 4°C. The supernatant was separated, stored, and pooled at −80°C until measurement of endothelin-1, prostacyclin, and nitric oxide. Endothelin-1 concentration was measured by ELISA and was read on the plate reader at 450 nm (Enzo, Japan). Because prostacyclin has a very short half-life, 6-keto-prostaglandin-F1α was measured as prostacyclin metabolites by EIA (Enzo, Japan). Nitric oxide concentration was measured based on Griess reaction based on colorimetrics (Enzo, Japan). All measurements were performed according to manufacturer's instructions.

2.4. Statistical Analysis. We described continuous data in means and standard deviation or median and interquartile range based on data distribution (data distribution normality was assessed with Kolmogorov–Smirnov test). We described categorical data in percentage. The correlation between continuous data was analyzed with Pearson correlation test (for normally distributed data) or Spearman correlation test (for nonnormally distributed data). We analyzed comparisons of continuous and categorical data among the groups with ANOVA and chi-square tests, respectively. The p value<0.05 was considered statistically significant. The statistical analysis was performed by using IBM SPSS 21 software package.

3. Results

3.1. Subject Characteristics. We conducted this study from January to November 2015 and enrolled forty-four subjects who met study criteria. The subjects had mean age of 39.5 ± 13.3 years old and largely comprised female (90.9%). The median peripheral O_2 saturation was 96%. Based on WHO functional class classification, the subjects were predominantly in WHO functional class II (79.5%), while only a minority (4.5%) was in functional class III. The mean haemoglobin level was 13.4 g/dL, and mean hematocrit concentration was 40%. The mean endothelin-1 level was 674.29 ± 405.28 pg/dL. The median prostacyclin level was 413.5 pg/dL. The mean nitric oxide level was 325.49 ± 77.56 μmol/L. Table 1 shows the clinical and laboratory characteristics of the subjects.

TTE and TOE showed that the mean minimum ASD diameter was 2.5 ± 0.6 cm, and maximum ASD diameter was 2.7 ± 0.9 cm. We detected enlargement of both right atrium (mean diameter 4.8 ± 0.7 cm) and right ventricle (mean diameter 4.7 ± 0.5 cm). Left heart dimensions were within normal limit. The majority of subjects has normal right ventricle function as indicated by mean TAPSE value of 2.5 ± 0.5 cm. An increase in pulmonary artery pressure was predicted with increased tricuspid valve regurgitant gradient (TVRG) (mean pressure 78.0 ± 28.5 mmHg) and right ventricular systolic pressure (mean pressure 85.4 ± 28.2 mmHg). The majority of subjects (61.4%) have left-to-right shunt across the defect, whereas 38.6% subjects have already developed bidirectional shunt with

predominant left-to-right shunt. Secondary tricuspid valve regurgitation was encountered in all subjects with various severities, with predominance of moderate regurgitation (54.5%). Table 1 shows the echocardiography parameters of the subjects.

The hemodynamic data from RHC showed that the mean mPAP was elevated (51.0 mmHg). The mean PAWP was normal, i.e., 8.0 ± 4.4 mmHg. The median of PVR was 12.7 Wood units, which was classified as high resistance. The median value of pulmonary-to-systemic flow ratio was 1.7. Based on mPAP cutoff point, 13 subjects (29.5 %) had mild PAH, 22 subjects (50%) had moderate PAH, and 9 subjects (20.5 %) had severe PAH. Table 1 shows the hemodynamic parameters recorded during RHC.

3.2. Correlation between Biomarkers and mPAP. Endothelin-1 level and mPAP had significant moderate positive correlation, with correlation coefficient (Pearson) $r = 0.423$ and p value = 0.004. In contrast, we observed no significant correlation between prostacyclin level and mPAP (Spearman, $r = -0.058$ and p value = 0.710) nor between nitric oxide levels and mPAP (Pearson, $r = 0.248$ and p value = 0.105). The scatter plots indicating these correlations are depicted in Figure 1.

3.3. Pattern of Biomarkers Based on PAH Severity. Based on mPAP value, the PAH severity was divided into three categories. The classification of PAH severity is depicted in Table 2. There was a statistically significant association between ages and PAH severities, with younger subjects associated with more severe PAH. Systolic blood pressure was significantly reduced in severe PAH, and diastolic blood pressure also tended to be lower. Peripheral O_2 saturation was significantly decreased in moderate and severe PAH compared with mild PAH. Haemoglobin and hematocrit were significantly elevated in severe PAH. The TTE calculation of TVRG and RVSP was heightened in the more severe PAH. Left atrial and ventricle dimensions were reduced in the more severe PAH. From RHC parameters, PVR was increased in the more severe PAH, whereas flow ratio was significantly depressed.

Further analysis on the pattern of biomarkers according to the severity of PAH revealed that the pattern of endothelin-1, prostacyclin, and nitric oxide was distinctive. The level of endothelin-1 constantly rose from subjects with mild PAH, moderate PAH, to severe PAH (mean ± SD: 587.52 ± 388.93 pg/dL, 613.57 ± 297.38 pg/dL to 948.09 ± 563.13 pg/dL, consecutively, p value = 0.071). The level of prostacyclin and nitric oxide had a similar pattern in association with severity of PAH. There was higher level of prostacyclin in subjects with mild-to-moderate PAH (median: 319.78 pg/dL to 453.76 pg/dL, respectively) and decreased level in subjects with severe PAH (median: 166.10 pg/dL) (Kruskal–Wallis test, p value = 0.128). Similar pattern was observed in the level of nitric oxide which was elevated in subjects with mild-to-moderate PAH (mean ± SD: 286.18 ± 88.42 μmol/L to 349.12 ± 65.86 μmol/L, respectively), whereas it was lowered in subjects with severe

Table 1: Clinical, laboratory, echocardiography, and hemodynamics characteristics of all subjects.

The characteristics	All subjects $n = 44$
Clinical and laboratory data	
Age (years), mean ± SD	39.5 ± 13.3
Sex, n (%)	
Male (%)	4 (9.1)
Female (%)	40 (90.9)
SBP (mmHg), median (IQR)	101 (95–120)
DBP (mmHg), median (IQR)	70 (70–80)
Peripheral O_2 saturation (%), median (IQR)	96 (93–98)
W.H.O functional class, n (%)	
I	7 (15.9)
II	35 (79.5)
III	2 (4.5)
Haemoglobin (g/dL), mean ± SD	13.4 ± 1.6
Hematocrit (%), mean ± SD	40.0 ± 4.8
Creatinine (g/dL), mean ± SD	0.8 ± 0.2
Endothelin-1 (pg/dL), mean ± SD	674.29 ± 405.28
Prostacyclin (pg/dL), median (IQR)	413.51 (190.13–1280.89)
Nitric oxide (μmol/L), mean ± SD	325.49 ± 77.56
Echocardiography data	
Minimum ASD diameter (cm), mean ± SD	2.5 ± 0.6
Maximum ASD diameter (cm), mean ± SD	2.7 ± 0.9
Right atrial dimension (cm), mean ± SD	4.8 ± 0.7
Right ventricle dimension (cm), mean ± SD	4.7 ± 0.5
Left ventricle ejection fraction (%), mean ± SD	71.2 ± 10.1
TAPSE (cm), mean ± SD	2.5 ± 0.5
TVRG (mmHg), mean ± SD	78.0 ± 28.5
RVSP (mmHg), mean ± SD	85.4 ± 28.2
Left atrial dimension (cm), median (IQR)	3.3 (2.9–3.7)
LVIDd (cm), median (IQR)	3.5 (3.1–3.8)
Tricuspid valve regurgitation, n (%)	
Mild	3 (6.8)
Moderate	24 (54.5)
Severe	17 (38.6)
Shunt direction, n (%)	
Left to right	27 (61.4)
Bidirectional	17 (38.6)
Hemodynamics RHC data	
Mean pressure (mmHg)	
Aorta, mean ± SD	103.6 ± 15.0
RV systolic, median (IQR)	86.0 (64.0–103.0)
Pulmonary artery, mean ± SD	51.0 ± 15.2
Pulmonary artery wedge pressure (mmHg)	8.0 ± 4.4
O_2 saturation (%)	
Aorta, median (IQR)	91.0 (85.0–94.0)
Mixed vein, median (IQR)	60.6 (55.0–64.0)
Left atrium, median (IQR)	90.5 (85.0–93.0)
Right atrium, mean ± SD	73.0 ± 9.4
Pulmonary vein, median (IQR)	95.5 (93.0–96.5)
Pulmonary artery, mean ± SD	77.0 ± 10.0
PVR (Woods unit), median (IQR)	12.7 (3.9–21.3)
Flow ratio, median (IQR)	1.7 (1.3–2.8)

Table 1: Continued.

The characteristics	All subjects $n = 44$
PAH severity, n (%)	10 (22.7)
Mild	13 (29.5%)
Moderate	22 (50.0%)
Severe	9 (20.5%)

IQR: interquartile range, SBP: systolic blood pressure, DBP: diastolic blood pressure, ASD: atrial septal defect, TAPSE: tricuspid annular plane systolic excursion, TVRG: tricuspid valve regurgitant gradient, RVSP: right ventricular systolic pressure, LVIDd: left ventricle internal diastolic diameter, RHC: right heart catheterization, PVR: pulmonary vascular resistance, mPAP: mean pulmonary artery pressure, PAH: pulmonary artery hypertension, and RV: right ventricle.

PAH (mean ± SD: 324.51 ± 71.92 μmol/L) (all differences p value = 0.064). Table 2 and Figure 2 show the distinctive pattern of endothelin-1, nitric oxide, and prostacyclin based on PAH severity.

3.4. Correlation between Other Parameters and mPAP. Table 3 shows the characteristics/parameters which associate with mPAP. Parameters with significant inverse/negative correlation with mPAP were age, systolic and diastolic blood pressure, peripheral O_2 saturation, left atrial dimension, LVIDd, and flow ratio. On the contrary, haemoglobin, TVRG, and RVSP had significant positive correlation with mPAP. Among these parameters, age and flow ratio had higher correlation coefficient, indicating stronger inverse/negative correlation with mPAP.

4. Discussion

To our knowledge, this is the first study to examine the profile of biomarkers in PAH related to uncorrected ASD. Our study revealed that among vasoactive agents, endothelin-1 has significant positive and moderate correlation with mPAP. Endothelin-1 level rises incrementally with PAH severity. Meanwhile, vasodilator substances, such as prostacyclin and nitric oxide, exhibit different fluctuation patterns. It increases in mild-to-moderate PAH, but decreases in severe PAH. It indicates that in PAH due to CHD with the left-to-right shunt, rising flow in the pulmonary vasculature will stimulate physiologic responses such as higher levels of the vasoconstrictor endothelin-1 and vasodilators such as nitric oxide and prostacyclin as a counterbalance. However, this physiologic response is blunted in severe PAH, indicated by discrepancy between vasoconstrictor and vasodilator interaction, possibly due to advanced pulmonary vascular remodeling.

We found a significant positive and moderate correlation between endothelin-1 level and mPAP. There was also an incremental increasing of endothelin-1 level in accordance with the severity of PAH, based on mPAP graded value. Li et al. [12] reported a similar result after investigating 30 healthy subjects and 58 PAH patients. Recent study comparing endothelin-1 level from 80 adults ASD and 19 healthy

(a)

(b)

(c)
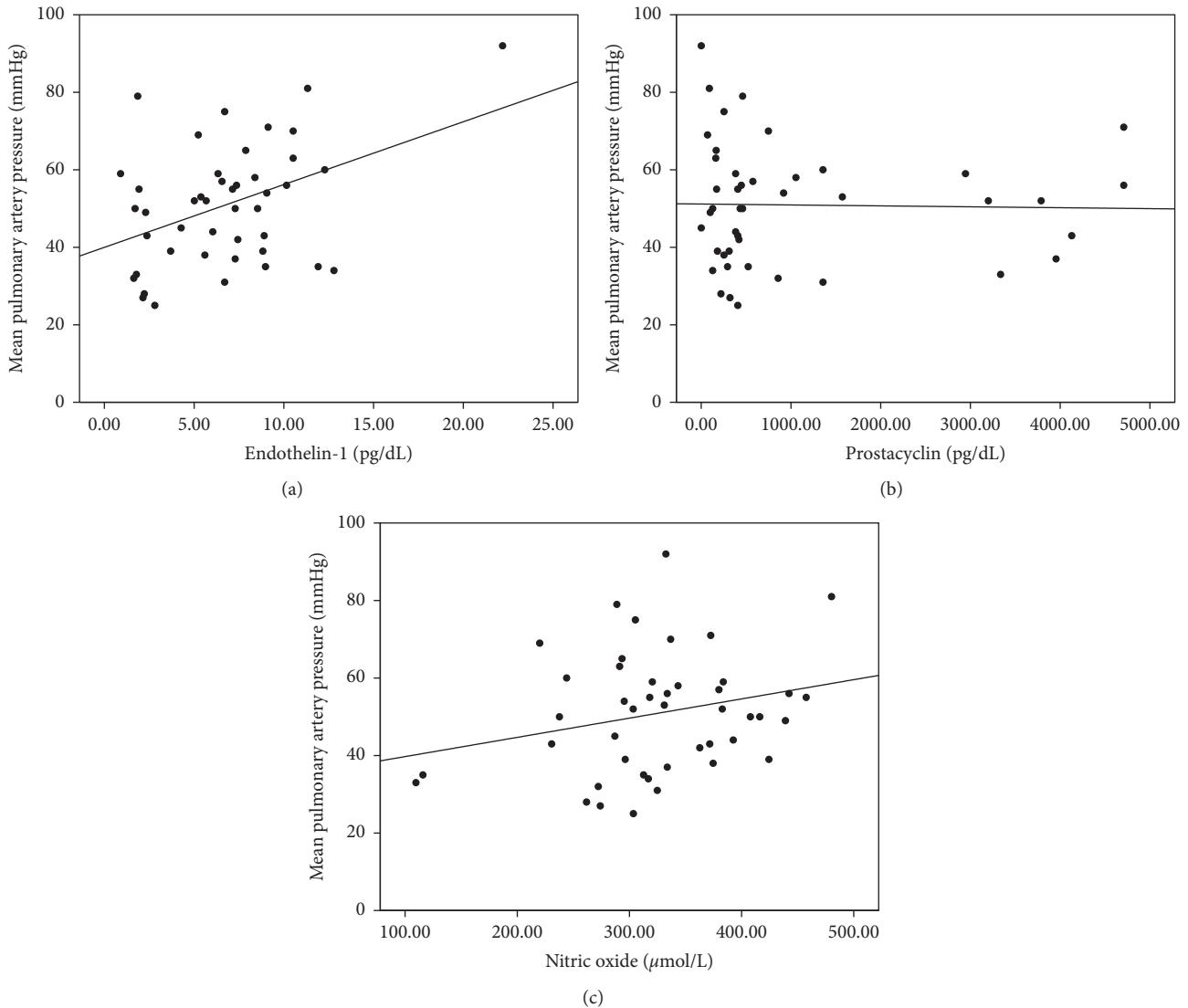
Figure 1: (a–c). Scatter plots indicate the significantly moderate positive correlation between endothelin-1 level and mPAP ($r = 0.423$ and p value = 0.004) (Figure 1(a)). No significant correlation is observed between prostacyclin and mPAP ($r = -0.058$ and p value = 0.710) (Figure 1(b)) and nitric oxide and mPAP ($r = 0.248$ and p value = 0.105) (Figure 1(c)).

subjects found that endothelin-1 level was significantly higher in unclosed ASD than in that with closed defects [13].

In this study, prostacyclin level was not significantly correlated with mPAP. Prostacyclin level was higher in mild and moderate PAH before declining in severe PAH. In an experimental study, Li et al. [14] investigated the effect of blood flow on the mediator release including prostacyclin and showed similar pattern as in our human study. In contrast to physiological shear stress, pathological shear stress (both low and high flow) diminished release of prostacyclin in circulation [14]. This finding revealed that physiological flow shear stress stimulates vasodilator release, whereas low or high pathological flow shear stress lessens vasodilator release. The balance between vasoconstrictors and vasodilators is disrupted by pathological flow. Moreover, Tuder et al. [15] proved that CHD results in more fluctuating production of prostacyclin synthase in three

different diameters of pulmonary arteries. This study demonstrated that severe PAH patients expressed significantly lower levels of prostacyclin enzyme. Therefore, the reduced or absence of prostacyclin production might be the marker for severe PAH [15]. We suggest that advanced pulmonary vascular remodeling contributes to reduced prostacyclin synthase enzymes and subsequently lower prostacyclin level.

We found that nitric oxide levels did not significantly correlate with mPAP. Nitric oxide has a propensity to be higher in mild-to-moderate PAH. Strikingly, it dropped in severe PAH. Similar pattern was seen in that of prostacyclin. Consistently, Kiettisanpipop et al. [16] reported differences in nitric oxide levels between severe and nonsevere PAH (cutoff point 60 mmHg). Nitric oxide level was strongly correlated with mild and moderate PAH but was lowered in subjects with severe PAH [16].

Table 2: Clinical, echocardiography, and hemodynamics characteristics of the subjects based on PAH Severity.

The characteristics	Mild PAH $n = 13$	Moderate PAH $n = 22$	Severe PAH $n = 9$	p value*
Clinical and laboratory data				
Age (years), mean ± SD	48.3 ± 10.9	38.2 ± 13.1	30.1 ± 9.4	0.030
Sex, n (%)				0.467
Male (%)	2 (15.4)	2 (9.1)	0 (0)	
Female (%)	11 (84.6)	20 (90.9)	9 (100)	
SBP (mmHg), median (IQR)	115.1 ± 14.2	105.1 ± 15.4	97.0 ± 7.4	0.014
DBP (mmHg), median (IQR)	74.1 ± 9.8	73.2 ± 13.2	68.3 ± 9.7	0.488
O$_2$ saturation (%), median (IQR)	97.6 ± 1.7	93.5 ± 3.6	93.0 ± 4.4	0.002
W.H.O functional class, n (%)				0.005
I	5 (38.5)	2 (9.1)	0 (0)	
II	8 (61.5)	20 (90.9)	7 (77.8)	
III	0 (0)	0 (0)	2 (22.2)	
Haemoglobin (g/dL), mean ± SD	13.5 ± 1.3	13.4 ± 2.1	15.5 ± 2.4	0.029
Hematocrit (%), mean ± SD	40.8 ± 3.6	40.4 ± 6.7	46.3 ± 7.5	0.053
Creatinine (g/dL), mean ± SD	0.8 ± 0.3	0.8 ± 0.2	0.8 ± 0.1	0.917
Endothelin-1 (pg/dL), mean ± SD	587.52 ± 388.93	613.57 ± 297.38	948.09 ± 563.13	0.071
Prostacyclin (pg/dL), median (IQR)	319.78 (236.20–319.82)	453.76 (383.01-1572-44)	166.10 (85.14-900-31)	0.128
Nitric oxide (μmol/L), mean ± SD	286.18 ± 88.42	349.12 ± 65.86	324.51 ± 71.92	0.064
Echocardiography data				
Minimum ASD diameter (cm), mean ± SD	2.4 ± 0.5	2.5 ± 0.6	2.6 ± 0.7	0.761
Maximum ASD diameter (cm), mean ± SD	2.5 ± 0.9	2.6 ± 1.0	2.8 ± 0.7	0.620
Right atrial dimension (cm), mean ± SD	4.8 ± 0.5	4.9 ± 0.8	4.3 ± 0.4	0.065
Right ventricle dimension (cm), mean ± SD	4.5 ± 0.3	4.8 ± 0.6	4.8 ± 0.5	0.263
Ejection fraction (%), mean ± SD	68 ± 11	71 ± 9	74 ± 11	0.398
TAPSE (cm), mean ± SD	2.6 ± 0.6	2.4 ± 0.5	2.3 ± 0.5	0.375
TVRG (mmHg), mean ± SD	50.5 ± 16.7	82.6 ± 19.9	106.2 ± 27.1	<0.001
RVSP (mmHg), mean ± SD	58.0 ± 16.4	90.1 ± 19.2	113.3 ± 27.1	<0.001
Left atrial dimension (cm), mean ± SD	3.9 ± 0.8	3.3 ± 0.6	3.0 ± 0.6	0.009
LVIDd (mm), mean ± SD	3.9 ± 0.8	3.5 ± 0.5	3.2 ± 0.4	0.020
Tricuspid valve regurgitation, n (%)				0.065
Mild	2 (15.4)	1 (4.5)	0 (0)	
Moderate	10 (76.9)	9 (40.9)	5 (55.6)	
Severe	1 (7.7)	12 (54.5)	4 (44.4)	
Shunt direction, n (%)				0.021
Left to right	12 (92.3)	10 (45.5)	5 (55.6)	
Bidirectional	1 (7.7)	12 (54.5)	4 (44.4)	
Hemodynamics RHC data				
Mean pressure (mmHg)				
Aorta, mean ± SD	114.4 ± 22.5	100.9 ± 14.9	95.1 ± 12.3	0.028
RV systolic, mean ± SD	56.8 ± 11.3	89.9 ± 14.4	111.8 ± 22.8	<0.001
Pulmonary artery, mean ± SD	33.6 ± 4.6	51.6 ± 6.0	73.9 ± 9.0	<0.001
Pulmonary artery wedge pressure (mmHg)	11.6 ± 6.5	7.7 ± 4.7	10.8 ± 5.4	0.094
O$_2$ saturation (%)				
Aorta, mean ± SD	93.3 ± 1.5	87.5 ± 6.1	85.2 ± 7.4	0.004
Mixed vein, mean ± SD	61.2 ± 19.3	55.5 ± 13.5	58.4 ± 4.2	0.530
Left atrium, mean ± SD	85.7 ± 25.9	83.6 ± 19.4	89.1 ± 5.6	0.784
Right atrium, mean ± SD	81.6 ± 5.9	71.2 ± 9.4	68.3 ± 7.1	0.001
Pulmonary vein, mean ± SD	95.5 ± 1.3	93.2 ± 6.1	94.1 ± 4.2	0.461
Pulmonary artery, mean ± SD	86.7 ± 4.9	74.8 ± 8.5	71.3 ± 7.9	<0.001
PVR (Woods unit), mean ± SD	3.2 ± 1.6	15.6 ± 3.2	26.8 ± 12.4	<0.001
Flow ratio, mean ± SD	3.4 ± 1.4	1.8 ± 0.8	1.5 ± 0.9	<0.001

*One-way ANOVA or Kruskal–Wallis test for continuous variables or chi-squared test for categorical variable, comparison among PAH severity. QR: interquartile range, SBP: systolic blood pressure, DBP: diastolic blood pressure, ASD: atrial septal defect, TAPSE: tricuspid annular plane systolic excursion, TVRG: tricuspid valve regurgitant gradient, RVSP: right ventricular systolic pressure, LVIDd: left ventricle internal diastolic diameter, PVR: pulmonary vascular resistance, and mPAP: mean pulmonary artery pressure.

In an experimental study using the aortocaval shunt model to mimic left-to-right shunt defect and PAH, there was a prominent rise of eNOS production in the animal model with aortocaval shunt compared with the control [17]. It indicates that eNOS, as well as nitric oxide, was produced as a consequence of continuous overflow to the pulmonary artery [17]. Another study with a similar model and observation of 12 weeks showed a significant increase of eNOS

(a)

(b)

(c)
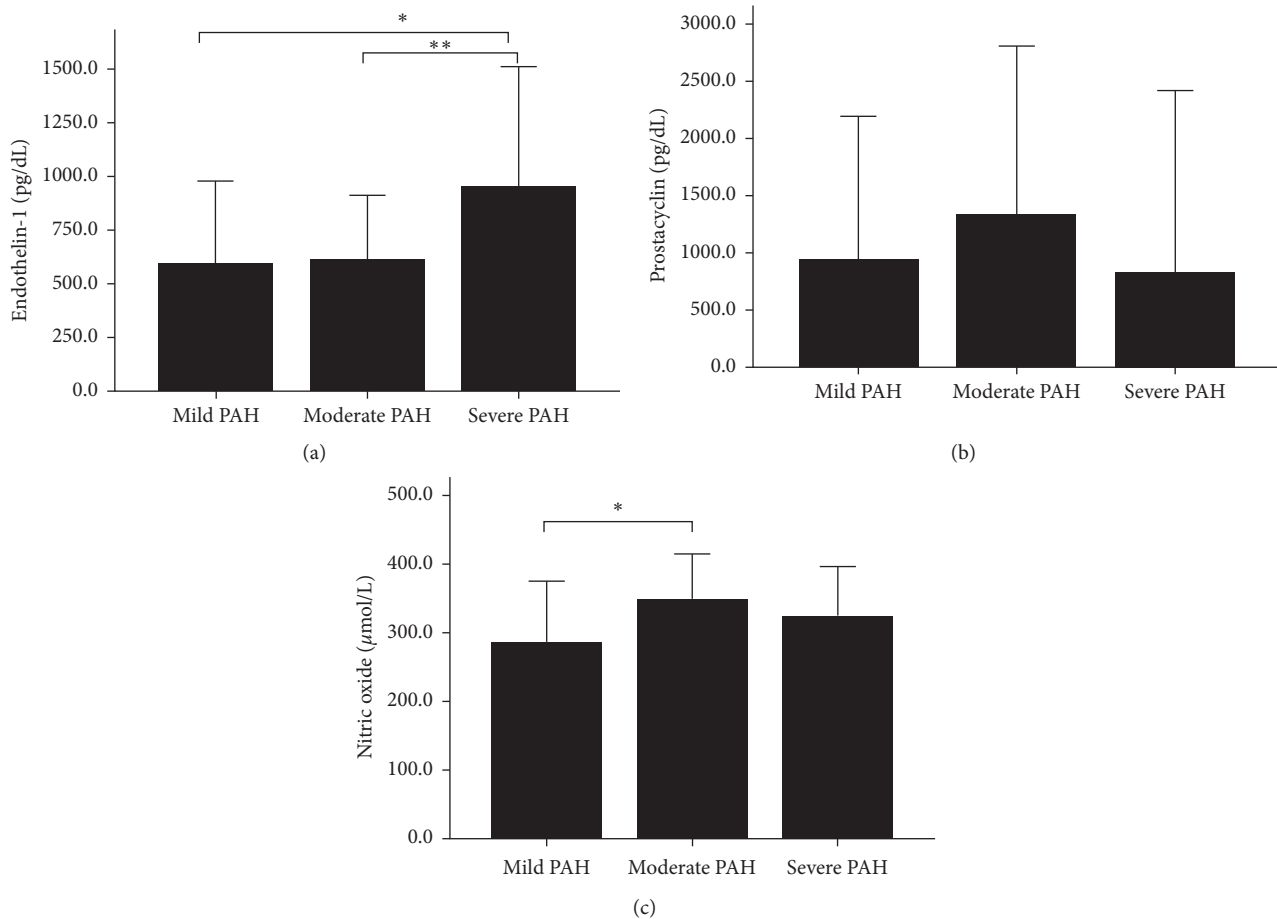
FIGURE 2: (a–c). Bar graphs indicate the distinctive pattern of biomarkers, i.e., endothelin-1, prostacyclin, and nitric oxide, according to the severity of PAH. Endothelin-1 is constantly increased from mild, moderate to severe PAH (Figure 2(a)). Post hoc analysis shows significant increase in endothelin-1 level in severe PAH as compared with mild ($p = 0.039$) and moderate PAH ($p = 0.036$). There was an increased level of prostacyclin in mild-to-moderate PAH and decreased level in severe PAH (Kruskal–Wallis, p value = 0.128) (Figure 2(b)). Similar pattern was observed in the level of nitric oxide which was increased in mild-to-moderate PAH, whereas decreased in severe PAH (one-way ANOVA, p value = 0.064) (Figure 2(c)). Post hoc analysis showed significant increase from mild to moderate PAH ($p = 0.020$).

compared with sham controls [18]. The result proved that eNOS greatly participates in remodeling process of pulmonary vascular before PAH development. An *in vitro* study reported that acute changes in flow or shear stress contribute to the activation of eNOS and nitric oxide [14]. Tworetzky et al. [19] investigated the acute effect of pulmonary flow alteration in humans. Nitric oxide levels were measured in ASD patients before and after closure by device [19]. It confirmed that nitric oxide levels decreased after defect closure. It was demonstrated that nitric oxide levels were significantly higher in children with congenital heart disease and PAH compared with non-PAH children [20]. Nevertheless, nitric oxide level based on the severity of PAH was not investigated.

Our study intended to elucidate the role of three biomarkers, namely, endothelin-1, prostacyclin, and nitric oxide, in the occurrence of PAH in ASD. Prostacyclin and nitric oxide levels were higher in mild and moderate PAH due to physiological response of pulmonary vasculatures as a consequence of continuous shear stress, though their levels decline as mPAP rises above 60 mmHg. On the contrary, vasoconstrictor endothelin-1 steadily and incrementally increased along with rising pulmonary artery pressure.

Among biomarkers, there are interactions in CHD and PAH. Shear stress due to overflow inevitably triggers nitric oxide production as well as endothelin-1 inhibition from endothelium. Between endothelin-1 and nitric oxide, an interaction is linked through several mechanisms such as cGMP and ET_B receptor activation [21]. The sustained interaction between endothelin-1 and ET_B receptors will generate deleterious effects on cell function even though it may initially produce nitric oxide in the early stage of PAH [21]. Endothelin-1 stimulates prostanoid formation, including prostacyclin, through the cyclooxygenase-dependent mechanism in endothelial cells via the ET_A receptor [22]. Prostacyclin triggers pulmonary artery relaxation by stimulating nitric oxide release and synergistically interacts with nitric oxide in smooth muscle cells. However, we did not find significant correlation among biomarkers in mild, moderate, or severe PAH, indicating more complex mechanisms in the pathobiology of CHD and PAH.

TABLE 3: The correlation between mPAP with other parameters.

Parameters	r value*	p value*
Age	−0.497	0.001
Systolic blood pressure	−0.462	0.002
Diastolic blood pressure	−0.316	0.037
Peripheral O_2 saturation	−0.460	0.002
Haemoglobin	0.300	0.048
Hematocrit	0.281	0.065
Creatinine	0.000	0.997
Minimum ASD diameter	0.103	0.513
Maximum ASD diameter	0.105	0.496
Right atrial dimension	−0.263	0.092
Right ventricle dimension	0.112	0.479
Left ventricle ejection fraction	0.249	0.104
TAPSE	−0.277	0.069
TVRG	0.673	<0.001
RVSP	0.676	<0.001
Left atrial dimension	−0.330	0.029
LVIDd	−0.375	0.012
Flow ratio	−0.508	<0.001

*Pearson correlation or Spearman correlation if applicable. ASD: atrial septal defect, TAPSE: tricuspid annular plane systolic excursion, TVRG: tricuspid valve regurgitant gradient, RVSP: right ventricular systolic pressure, and LVIDd: left ventricle internal diastolic diameter.

Interestingly, we found that female patients were predominant, and younger age was associated with more severe PAH. In this study, female subjects accounted for 90.9% of all ASD subjects, in line with previous studies showing that ASD was more prevalent in women. The CONCOR registry reported 62% of ASD patients were females [23]. Humenberger et al. [24] stated that women comprise 69.5% of all ASD patients. This female predominance is also recognized by Euro Heart Survey from 1998 to 2004 (68%) [25]. In our database, i.e., COHARD-PH Registry, among 350 adult ASD patients, 86% have been diagnosed PAH and 86% of those are women (unpublished data). Badesch et al. [26] from REVEAL Registry and Mair et al. [27] independently reported that 79.5% of PAH patients were females and were four times more susceptible to PAH than male patients. The inverse correlation between age and mPAP may indicate other factors contribute to the development of PAH in ASD patients. The presence of concomitant genetic background may predispose some patients to the development of PAH [28]. The pulmonary overflow due to the chronic left-to-right shunt is the triggering factor for development of PAH.

Given the distinctive patterns of three key biomarkers of PAH in our study, we speculate that in the early phase of PAH (mild-to-moderate PAH), the physiologic response of endothelin-1 still exists, such that the therapy with endothelin-1 receptor antagonists is important to reduce pulmonary artery pressure in early PAH. In the case of uncorrected ASD, the reduced pulmonary artery resistance, i.e., decreased mPAP and PVRI, may lead to the possibility of defect closure. On the contrary, prostacyclin analogue and PDE-5 inhibitor have their most impact in the later phase of PAH, as endogenous prostacyclin level is diminished.

5. Limitation of the Study

The statistical power of this study can be increased by adding more subjects. Causality between the biomarkers profile and pulmonary hypertension in unrepaired ASD is still unknown as this is a cross-sectional study. Further investigation with prospective cohort design could produce a more representative pattern of each biomarker and its relation with PAH severity.

6. Conclusion

In conclusion, there is a distinctive pattern among endothelin-1, nitric oxide, and prostacyclin in correlation with the severity of PAH in adult uncorrected ASD. A significantly positive correlation exists between endothelin-1 and the severity of PAH and mPAP. Meanwhile, nitric oxide and prostacyclin are increased in mild-to-moderate PAH then decreased in severe PAH. The flow ratio and age are inversely correlated with the severity of PAH.

Data Availability

The raw data and data set used to support the findings of this study have not been made available because of the confidentiality policy in our department. However, authors are open to any discussions regarding this research.

Additional Points

All authors assume responsibility for all aspects of the reliability and freedom from bias of the data presented and their discussed interpretation.

Disclosure

This manuscript is part of the dissertation for Doctoral Degree submitted by L.K.D to Doctoral Programme Faculty of Medicine Universitas Gadjah Mada, Yogyakarta, Indonesia, in the year 2016. The full dissertation manuscript is deposited in the University Repository.

Conflicts of Interest

The authors declare that they have no conflicts of interest.

Acknowledgments

References

[1] V. V. McLaughlin, S. L. Archer, D. B. Badesch et al., "ACCF/ AHA 2009 expert consensus document on pulmonary hypertension," *Journal of the American College of Cardiology*, vol. 53, no. 17, pp. 1573–1619, 2009.

[2] H. Faber and J. Loscalzo, "Mechanism of disease: pulmonary arterial hypertension," *The New England Journal of Medicine*, vol. 351, pp. 1655–1665, 2004.

[3] B. W. Christman, C. D. McPherson, J. H. Newman et al., "An imbalance between the excretion of thromboxane and prostacyclin metabolites in pulmonary hypertension," *New England Journal of Medicine*, vol. 327, no. 2, pp. 70–75, 1992.

[4] N. Galiè, M. M. Hoeper, M. Humbert et al., "Guidelines for the diagnosis and treatment of pulmonary hypertension," *European Heart Journal*, vol. 30, pp. 2493–2537, 2009.

[5] I. Adatia, S. S. Kothari, and J. A. Feinstein, "Pulmonary hypertension associated with congenital heart disease," *Chest*, vol. 137, no. 6, pp. 52S–61S, 2010.

[6] M. G. J. Duffels, P. M. Engelfriet, R. M. F. Berger et al., "Pulmonary arterial hypertension in congenital heart disease: an epidemiologic perspective from a Dutch registry," *International Journal of Cardiology*, vol. 120, no. 2, pp. 198–204, 2007.

[7] M. Humbert, O. Sitbon, and G. Simonneau, "Treatment of pulmonary arterial hypertension," *New England Journal of Medicine*, vol. 351, no. 14, pp. 1425–1436, 2004.

[8] L. Krisdinarti, A. B. Hartopo, D. W. Anggrahini, A. H. Sadewa, A. S. Wahab, and B. Y. Setianto, "Clinical characteristics of adult uncorrected secundum atrial septal defect: a pilot study," *Journal of Thee Medical Sciences (Berkala Ilmu Kedokteran)*, vol. 48, no. 2, pp. 89–97, 2016.

[9] R. M. Lang, L. P. Badano, V. Mor-Avi et al., "Recommendations for cardiac chamber quantification by echocardiography in adults: an update from the American Society of Echocardiography and the European Association of Cardiovascular Imaging," *Journal of the American Society of Echocardiography*, vol. 28, no. 1, pp. 1–39, 2015.

[10] L. G. Rudski, W. W. Lai, J. Afilalo et al., "Guidelines for the echocardiographic assessment of the right heart in adults: a report from the American society of echocardiography," *Journal of the American Society of Echocardiography*, vol. 23, no. 7, pp. 685–713, 2010.

[11] M. J. Kern, "Hemodynamic data and basic electrocardiography," in *The Cardiac Catheterization Handbook*, M. J. Kern, Ed., pp. 91–144, Elsevier Saunders, Philadelphia, PA, USA, 2011.

[12] X. Li, J. Qiu, M. Pan et al., "Correlation between congenital heart disease complicated with pulmonary artery hypertension and circulating endothelial cells as well as endothelin-1," *International Journal of Clinical and Experimental Pathology*, vol. 8, no. 8, pp. 10743–10751, 2015.

[13] M. Komar, J. Podolec, W. Płazak et al., "Elevated level of plasma endothelin-1 in patients with atrial septal defect," *Journal of Cardiovascular Ultrasound*, vol. 12, p. 31, 2014.

[14] M. Li, K. R. Stenmark, R. Shandas, and W. Tan, "Effects of pathological flow on pulmonary artery endothelial production of vasoactive mediators and growth factors," *Journal of Vascular Research*, vol. 46, no. 6, pp. 561–571, 2009.

[15] R. M. Tuder, C. D. Cool, M. W. Geraci et al., "Prostacyclin synthase expression is decreased in lungs from patients with severe pulmonary hypertension," *American Journal of Respiratory and Critical Care Medicine*, vol. 159, no. 6, pp. 1925–1932, 1999.

[16] P. Kiettisanpipop, P. Lertsapcharoen, P. Chotivittayatarakorn, and Y. Poovorawan, "Plasma levels of nitric oxide in children with congenital heart disease and increased pulmonary blood flow," *Journal of the Medical Association of Thailand = Chotmaihet Thangphaet*, vol. 90, no. 90, pp. 2053–2057, 2007.

[17] C.-F. Lam, T. E. Peterson, A. J. Croatt, K. A. Nath, and Z. S. Katusic, "Functional adaptation and remodeling of pulmonary artery in flow-induced pulmonary hypertension," *American Journal of Physiology-Heart and Circulatory Physiology*, vol. 289, no. 6, pp. H2334–H2341, 2005.

[18] D. Zen-Kong, T. Mian-Shin, C. Chee-Yin, I. J. Chen, A. Y. Jeng, and J. R. Wu, "Effects of increased pulmonary flow on the expression of endothelial nitric oxide synthase and endothelin-1 in the rat," *Clinical Science*, vol. 103, pp. 289S–293S, 2002.

[19] W. Tworetzky, P. Moore, J. M. Bekker, J. Bristow, S. M. Black, and J. R. Fineman, "Pulmonary blood flow alters nitric oxide production in patients undergoing device closure of atrial septal defects," *Journal of the American College of Cardiology*, vol. 35, no. 2, pp. 463–467, 2000.

[20] Y. Ikemoto, M. Teraguchi, J. Takaya, S. Nogi, and Y. Kobayashi, "Plasma levels of nitric oxide products and endothelin in pulmonary hypertension with congenital heart disease," *Acta Paediatrica*, vol. 87, no. 6, pp. 715-716, 1998.

[21] S. L. Bourque, S. T. Davidge, and M. A. Adams, "The interaction between endothelin-1 and nitric oxide in the vasculature: new perspectives," *American Journal of Physiology-Regulatory, Integrative and Comparative Physiology*, vol. 300, no. 6, pp. R1288–R1295, 2011.

[22] O. Baretella and P. Vanhoutte, "Endothelium-dependent contractions: prostacyclin and endothelin-1, partners in crime?," *Advances in Pharmacology*, vol. 77, pp. 177–208, 2016.

[23] C. L. Verheugt, C. S. P. M. Uiterwaal, E. T. van der Velde et al., "Gender and outcome in adult congenital heart disease," *Circulation*, vol. 118, no. 1, pp. 26–32, 2008.

[24] M. Humenberger, R. Rosenhek, H. Gabriel et al., "Benefit of atrial septal defect closure in adults: impact of age," *European Heart Journal*, vol. 32, no. 5, pp. 553–560, 2011.

[25] P. M. Engelfriet, M. G. J. Duffels, T. Moller et al., "Pulmonary arterial hypertension in adults born with a heart septal defect: the Euro Heart Survey on adult congenital heart disease," *Heart*, vol. 93, no. 6, pp. 682–687, 2007.

[26] D. B. Badesch, G. E. Raskob, C. G. Elliott et al., "Pulmonary arterial hypertension," *Chest*, vol. 137, no. 2, pp. 376–387, 2010.

[27] K. M. Mair, A. K. Z. Johansen, A. F. Wright, E. Wallace, and M. R. MacLean, "Pulmonary arterial hypertension: basis of sex differences in incidence and treatment response," *British Journal of Pharmacology*, vol. 171, no. 3, pp. 567–579, 2014.

[28] M. W. Geraci, T. M. Bull, and R. M. Tuder, "Genomics of pulmonary arterial hypertension: implications for therapy," *Heart Failure Clinics*, vol. 6, no. 1, pp. 101–114, 2010.

Research Article

The Autonomic Regulation of Circulation and Adverse Events in Hypertensive Patients during Follow-Up Study

Oleg V. Mamontov [1,2] **Andrey V. Kozlenok,[1] Alexei A. Kamshilin** [3] **and Evgeny V. Shlyakhto[1,2]**

[1]*Dept. of Circulation Physiology, Almazov National Medical Research Centre, St. Petersburg 197341, Russia*
[2]*Dept. of Departmental Therapy, Pavlov First Saint Petersburg State Medical University, St. Petersburg 197022, Russia*
[3]*Faculty of Applied Optics, ITMO University, St. Petersburg 197101, Russia*

Correspondence should be addressed to Oleg V. Mamontov; mamontoffoleg@gmail.com

Purpose. Comprehensive study of autonomic regulation assessed during follow-up could provide new detailed information about the risks stratification for hypertensive patients. Therefore, we investigated the associations of these indices with death, stroke, and revascularization during the follow-up observation of 55 patients. *Methods*. All patients were with target organ damage, and 27 of them had associated clinical conditions (ACC). Mean age of patients with and without ACC was 62.6 ± 4.2 and 51.9 ± 9.9 (mean ± SD) years, respectively. Follow-up was from 66 to 95 months. At entry, autonomic regulation was assessed by the tilt test, Valsalva maneuver, hand-grip test, and cold-stress vasoconstriction. Hemodynamic parameters were measured by continuous blood pressure monitoring, occlusion plethysmography, and electrocardiography. Re-examination of patients was carried out by questioning and physical and laboratory examination. *Results*. We found that fatal outcomes were associated with a lower Valsalva index (1.34 ± 0.16 vs. 1.69 ± 0.37, $P < 0.05$) and depressed cold vasoconstriction (0.20 ± 0.02 vs. $0.39 \pm 0.16\%$, $P < 0.05$) but with higher peripheral resistance (1.36 ± 0.19 vs. 0.89 ± 0.25, $P < 0.001$) and respiratory-range blood pressure variability (BPV) (18.2 ± 14.2 vs. 6.2 ± 4.2 mmHg, $P < 0.001$). Higher total-range BPV (103 ± 51 vs. 65 ± 45 mmHg, $P < 0.05$) in patients who had a stroke was observed. Initial diastolic orthostatic hypertension (6.6 ± 10.8 vs. 0.4 ± 6.3 mmHg, $P < 0.05$) and lower Valsalva index (1.36 ± 0.11 vs. 1.82 ± 0.37, $P < 0.05$) in patients who suffered a new ACC were important findings as well. *Conclusions*. This study shows that such autonomic regulation indices as Valsalva index, blood pressure dynamics in the tilt test, cold-stress vasomotor reactivity, and BPV are important for prognosis of hypertension course.

1. Introduction

Hypertension is the most important factor worsening the prognosis and survival of patients with cardiovascular diseases [1]. However, it is known that not all hypertensive patients have equal chances for disease progression [2]. The factors of cardiometabolic risk are the most thoroughly investigated: a number of systemic publications are devoted to study of the prognosis of these factors for patients with cardiovascular diseases in developed countries [3]. At the same time, there are often studies in which autonomic regulation and parameters of hemodynamic were studied resulting in inclusion of respective indicators in the

management for sudden death issued by the American Heart Association [4]. However, the prognosis of the patients was studied most often after the development of complications and concerned, as a rule, sudden death. In the vast majority of these studies, the markers that relate mainly to the regulation of the heart rhythm, such as the cardiac component of the arterial baroreflex, heart rate variability, heart rate turbulence, and alteration of the T-wave, were used [5]. Probably, these markers were selected due to commonly accepted study design in which the indices of the state of autonomous regulation were extracted from the data obtained in either the emergency or hospital.

The prognostic value of more specific markers of autonomic regulation, such as the reuptake of norepinephrine, using scintigraphy with iodine-123 meta-iodobenzylguanidine, has been studied only in a small number of papers [6, 7]. Basic information about significance of the autonomic nervous system for prognosis was obtained from the analysis of heart rate variability, concentration catecholamine measurement, and arterial baroreflex in patients with heart failure and myocardial infarction [8, 9]. However, vasomotor regulation of blood circulation has a major role in maintaining systemic hemodynamics, changes in which are also associated with a prognosis worsening. Munhoz et al. found that patients with chronic heart failure significantly more likely died during an 18-month follow-up if they had high muscle tone of the sympathetic nerve and low peripheral blood flow [10].

There are studies in which indicators relating to both cardiac and vasomotor neurogenic reactivity in patients with hypertension during follow-up were analyzed in the presence of diabetes [11] or with autonomic failure [12]. However, we have not found any work devoted to comprehensive study of prognostic value of the autonomic regulation in patients with essential hypertension but in absence of significant diabetic autonomic neuropathy and autonomic or heart failure. Nevertheless, prognosis of the increased mortality risk, the risk of developing cardiovascular complications associated with the progression of the hypertension, and a decrease in quality of patient life is very important.

The aim of this research was to evaluate the prognostic significance of the indices of autonomic regulation and hemodynamic parameters in hypertensive patients with target organ damage and with associated clinical conditions in the course of the follow-up observation.

2. Methods

2.1. Patients. This study enrolled 55 patients with essential hypertension. All patients underwent either inpatient or outpatient examinations at the Almazov National Medical Research Center, St. Petersburg. The criteria for inclusion of the patient in the study were his stable condition and regular therapy for at least 10 days. The exclusion criterion was the presence of a severe concomitant disease that was proven to affect the prognosis. The study plan was approved by the research ethical committee of the Almazov National Medical Research Center prior to the examinations. All patients provided their informed consent in the written form for participation in the study.

At the time of the initial examination, all subjects were classified as patients with target organ damage. About half of them had associated clinical conditions (ACCs). The average time of the follow-up observation was 7.1 ± 2.2 years (from 5.5 to 7.9 years). Average age of hypertensive patients with and without ACC was 62.6 ± 4.2 and 51.9 ± 9.9 years, respectively. Dominating associated clinical conditions for patients included in the study is given in Table 1. Most patients with associated conditions had coronary artery disease, including myocardial infarction and previous myocardial revascularization. Two patients had significant atherosclerosis of the brachycephalic arteries, and two patients had a stroke.

2.2. Autonomic Testing. During the initial examination, all patients underwent cardiac examination including echocardiogram recording and evaluation of cardiometabolic risk factors. Moreover, a comprehensive assessment of autonomic regulation of blood circulation was carried out for all patients according to the following sequence of tests:

(1) Tilt test of a shortened protocol (10 min. at rest and 10 min. in orthostasis)
(2) Valsalva maneuver
(3) Hand-grip test
(4) Cold stress-induced vasoconstriction for evaluation reaction of the forearm vessels while cooling the skin of the upper chest for 2 minutes

In addition, the spontaneous arterial baroreflex (ABR) and the spectral power of variability of both the heart rate and arterial blood pressure (BP) were estimated. Hemodynamic parameters were measured continuously by means of a BP monitor Finometer-Pro (Finapres Medical Systems, The Netherlands) with parallel electrocardiogram (ECG) recording. The forearm blood flow was measured by venous occlusion plethysmography using a Dohn air-filled cuff.

The secondary examination of the patients enrolled in the study was done by interviewing, physical examination, and reviewing medical records obtained on the basis of inpatient and outpatient analyses performed in the last three months before censoring. In the event of patient's death, a survey of his relatives was conducted. The questionnaire is shown in Table 2. The analysis of the relationship between the indices autonomous regulation at the time of the survey and outcomes based on the results of the questionnaire survey was carried out after interviewing and forming a database.

2.3. Statistical Analysis. To estimate the difference in the measured hemodynamic parameters or autonomic regulation indices between patient samples, we used the nonparametric Mann–Whitney test. Difference in qualitative and categorical signs was assessed by analyzing the contingency tables (Pearson criterion χ^2). The level of $P < 0.05$ was considered as significant, whereas the level of $0.05 < P < 0.1$ was considered as a tendency. The statistical analysis of the measured data was carried out by using the software Statistica 10 (StatSoft Russia).

3. Results

The study revealed that both the Valsalva index and diastolic blood pressure were significantly different in groups of patients with and without ACC. In addition, it was found that the parameter of cold vasoconstriction and heart rate are tended to differ as it is shown in Table 3.

Table 1: Clinical characteristics of patients included in the study.

Associated clinical condition (ACC)	Occurrence (%) (number of cases)	Mean age ± SD (years)
All ACC	28 (51)	62.6 ± 4.2
Coronary heart disease	25 (45)	63.5 ± 4.2
Myocardial infarction	14 (25)	64.7 ± 5.7
Myocardial revascularization	13 (24)	60.8 ± 5.7
Stroke	2 (4)	63.0 ± 8/4
Severe atherosclerosis of brain arteries	2 (4)	57.5 ± 3.5
Chronic kidney disease stage IV	1 (2)	84
Without ACC	27 (49)	51.9 ± 9.9

Table 2: Questionnaire of the secondary examinations of patients.

	Question	Possible answer
1	Is patient alive?	Yes, no
Have there been cardiovascular complications in the time that has elapsed since the examination?		
2	Myocardial infarction	Yes, no
3	Stroke	Yes, no
4	Revascularization	Yes, no
5	New cases of diabetes mellitus	Yes, no
Accepted therapy:		
6	Regular use of antihypertensive drugs	Yes, no
7	The number of antihypertensive drugs, pcs	Value
8	Regular use of statins	Yes, no
The therapy efficacy:		
9	Subjective assessment of well-being	From 1 to 5
10	BP measurements at home: the mean of three last measures, mmHg	Value
11	The presence of hypertensive crises during the last three months	Yes, no
12	The level of total cholesterol in the last examination, mmol/l	Value

Table 3: Indices of systemic hemodynamics and autonomous regulation in patients with and without ACC during the initial examination.

Parameter	Without ACC	With ACC	P
Systolic BP (mmHg)	132 ± 16	134 ± 22	0.79
Diastolic BP (mmHg)	71 ± 11	65 ± 18	0.043
Heart rate (beat/min)	71 ± 11	66 ± 12	0.084
Valsalva index (rel. un.)	1.8 ± 0.4	1.51 ± 0.3	0.046
Hand grip (mmHg)	16.6 ± 6.7	14.1 ± 5.3	0.18
Cold vasoconstriction (rel. un.)	0.42 ± 0.15	0.29 ± 0.12	0.054
ABR (ms/mmHg)	7.8 ± 6.3	6.4 ± 4.0	0.31

In the course of questioning, it was found that five patients died during the follow-up (see Table 4). All deceased patients at the time of the initial examination had ACC, $\chi^2 = 4.46$; $P < 0.05$. In all cases, the primary cause of the death was cardiovascular disease progression. Only three patients had a new myocardial infarction: two of them initially had hypertension with ACC, whereas three patients had target organ damage only. New stroke was registered in six patients: four with ACC and two without. The revascularization of the coronary arteries has been performed to seven patients of whom six patients with ACC and one without,

$\chi^2 = 3.05$; $P < 0.08$. At the time of enrollment, nine patients had concomitant type 2 diabetes mellitus. At the secondary examination, new cases of diabetes were identified in four patients, three of them with ACC, and one without.

Therefore, out of 27 hypertensive patients with target organ damage only, four patients have experienced ACC. Patients with ACC died and underwent revascularization more often, whereas there were no difference in the number of new cases of cardiovascular complications between patients with and without ACC.

3.1. Hemodynamics and Autonomic Regulation Associated with Fatal Outcome. Since all the dead during the observation period had ACC at the time of initial examination, the comparative analysis was performed only in the group of hypertensive patients with ACC. When assessing the relationship between baseline clinical data, autonomic regulation parameters, and hemodynamic parameters in groups with different outcomes, it was found that patients who had died by the time of the second examination/survey was elder than survivors: 77.4 ± 14.5 versus 61.3 ± 14.3 years; $P = 0.02$.

Patients at the time of enrollment to the study had no signs of clinically significant heart failure, and only one patient had initial cardiomegaly, whereas the grade of chronic heart failure was estimated as I functional class (New York Heart Association). At the same time, the left ventricle ejection fraction was comparable in the group with fatal outcome ($57.0 \pm 5.4\%$) and in the group of survivors ($59.6 \pm 11.6\%$); $P > 0.05$. However, the total peripheral resistance (TPR) was observed (during the initial examination) to be significantly higher among the patients who had died: 1.36 ± 0.19 versus 0.86 ± 0.25 rel. un., $P < 0.001$. Moreover, there were a number of differences in the indices of autonomic regulation of blood circulation in deceased patients at the time of the initial examination. Patients of this group had a more pronounced decrease of diastolic BP in the orthostasis (-7.8 ± 8.0 mmHg) in contrast to the expected increase (1.5 ± 6.6 mmHg) in the group of survivors, $P = 0.011$. Note that difference between the groups in the dynamics of diastolic BP was most clearly manifested in the initial period of the orthostasis (the first minute): -13.0 ± 2.5 versus -2.2 ± 8.6 mmHg, $P = 0.011$. Moreover, variability of BP in the high-frequency (respiratory) range was much higher in the group of deceased patients as compared to another group: 18.2 ± 14.2 and 6.2 ± 4.2 mmHg^2, respectively.

Contrary to expectations, deceased patients did not demonstrate a significant reduction in the magnitude of

TABLE 4: Outcomes of monitoring hypertensive patients with and without ACC in the course of the follow-up observation.

Outcome	Target organ damage ($n = 28$)	With associated clinical conditions ($n = 28$)	Significance of differences
Death	0	5	$P < 0.05$
Myocardial infarction	1	2	$P > 0.05$
Stroke	2	4	$P > 0.05$
Revascularization	1	5	$P < 0.05$
New cases of diabetes mellitus	1	3	$P > 0.05$
Progression of hypertension	4	—	

spontaneous ABR compared to the group of survivors: 4.4 ± 3.0 and 7.5 ± 6.5 ms/mmHg, respectively, $P > 0.05$. This was most likely due to insufficient sample size of the former group. However, the Valsalva index was smaller in the group of deceased patients: 1.34 ± 0.16 versus 1.69 ± 0.37 rel. un., $P < 0.05$. Moreover, weakening of cold vasoconstriction of the forearm vessels was observed in this group: 0.20 ± 0.02 versus 0.39 ± 0.16 rel. un., $P < 0.05$. The data indicate a high risk of death in the group with a decrease in cardiac and vasomotor efferent reactivity against a background of increased both peripheral vascular resistance at rest and BP variability in the respiratory range.

3.2. Hemodynamics and Autonomic Regulation Associated with New Stroke.

It should be noted that none of the patients who had undergone stroke during the observation had this diagnosis at the time of the initial examination. Therefore, the analysis was performed only in a group of patients who had no stroke or hemodynamic significant atherosclerosis of brachiocephalic arteries previously. Four patients who died during the observation period did not have reliable data on the stroke. Therefore, they were excluded from the analysis. Consequently, 47 patients were analyzed. It was found that the age of stroke patients had a tendency to be higher than in the comparison group: 65.8 ± 13.8 versus 55.2 ± 13.2, $P = 0.07$.

In addition, six patients who suffered stroke during the follow-up had specific reaction of BP on the orthostasis. The systolic BP increase in the orthostasis was observed in the stroke group, whereas it was the expected decrease of this parameter in the comparison group (41 patients): 8 ± 16 and -8 ± 12 mmHg, respectively, $P < 0.01$. It is worth noting that variability of the total systolic BP was higher in the group of patients suffered of stroke than in the comparison group (103 ± 51 and 65 ± 45 mmHg, $P < 0.05$), which was mainly due to very low-frequency spectral component (<0.04 Hz): 67 ± 40 and 37 ± 32 mmHg, respectively, $P < 0.05$. Therefore, the increased risk of stroke development is associated with aging, as well as with the hypertensive response on the orthostasis and high BPV.

3.3. Predictors of Hypertension Progression.

As seen in Table 4, progression of the hypertension, which was defined as the appearance of associated clinical conditions in patients who did not have their previously, was noted in four cases.

By using comparative analysis, we have found that patients who transferred to the disease stage with ACC (four patients) were comparable by age with other patients in the group without ACC (twenty-three patients): 54.5 ± 9.3 versus 50.2 ± 13.7 years, respectively, $P = 0.55$. In spite of comparable values of initial BP (130 ± 11 and 133 ± 15 mmHg, $P > 0.05$), patients with progressive of disease had significant increase of both diastolic BP and TPR in the initial period of orthostasis as it is shown in Table 5.

Moreover, the Valsalva index was smaller in patients of the group with progressive course of disease: 1.36 ± 0.11 and 1.82 ± 0.37 rel. un., $P < 0.05$ Therefore, sympathoadrenal hyperactivity, manifested as a significant increase in BP and TPR in response to the orthostasis against the decrease in efferent cardiac reactivity manifested in a decrease in the Valsalva index, is a predictor of the likely progression of hypertension.

3.4. Factors of New Case Development of Diabetes Mellitus.

The analysis was carried out among patients who do not suffer from diabetes at the time of the first examination. There were four patients classified as having diabetes mellitus during the follow-up. The control group included 37 subjects considering that deceased patients and those who had diabetes before study were excluded from the analysis. It was found that all patients with newly developed diabetes regularly took statins, whereas only 15 patients (or 41%) took statins in the control group, $\chi^2 = 5.13$, $P < 0.05$. No hemodynamic parameters and indices of autonomic regulation were different between the groups.

4. Discussion

The course of our local one-center follow-up observation has shown that the prognosis for hypertensive patients depends on initial hemodynamic parameters and indices of autonomic regulation that are not taken to routine study in patients with cardiovascular diseases. We have found that in patients with the most severe prognosis, weaker efferent regulatory function on the heart and blood vessels and decreased neurogenic reactivity in response to physiological challenges against the background of the initial increase in peripheral vascular tone were observed. These data are consistent with the results of studies demonstrating a decrease in norepinephrine reuptake in myocardium [13] and an increase in TPR [10] in patients at high risk of sudden death. It is worth noting that the results in references [10, 13] were obtained in patients with significant heart failure, whereas in our study, neither drop in ejection fraction nor cardiomegaly was observed in any patient. Apparently, impairment of neurogenic control, which may occur in response to a decrease cardiac output, could be of independent significance for prognosis in patients with preserved left ventricular contractility.

TABLE 5: Dynamics of arterial BP and TPR during 1 minute of the orthostasis in hypertensive patients without ACC at the time of initial examination.

	Progressive disease ($n = 4$)	Nonprogressive disease ($n = 24$)	P
Change of diastolic BP (mmHg)	6.64 ± 10.8	0.40 ± 6.3	0.05
Total peripheral resistance (rel. un.)	0.49 ± 0.80	0.05 ± 0.21	0.028

In this study were performed easily reproducible and relatively simple tests that appear as clinical equivalent of more complex and expensive procedures. Thus, the Valsalva maneuver is a method for assessing the safety of the cardiac neurogenic regulation and can partly repeat such a complex method as myocardial scintigraphy with MIBG. Vasomotor function and sympathoadrenal reactivity reflect the cold vasoconstriction, the assessment of short-term BPV and tilt test. It is worth noting that most of the studies, which included the tilt test, were devoted to the study of orthostatic insufficiency, while an excessive increase in blood pressure in the upright position was ignored. Not enough attention was paid to assessment of the short-term BP during continuous BP recording. Nevertheless, an increase of this parameter in the respiratory range is associated with mortality risk, whereas its increase in the low-frequency range is a risk marker of the stroke.

The importance of higher BP variability in the respiratory range in patients with a negative prognosis of death from cardiovascular pathology remains insufficiently understood. However, most probable explanation of the revealed phenomenon is impairment of the autonomic nervous system function that provides diminishing of BP during breathing (the so-called cardiorespiratory conjugation). This impairment reflects heaviness of autonomic dysfunction.

Most likely, a negative prognosis regarding the development of stroke is associated with uncontrolled crisis type course of the arterial hypertension that is a consequence of two factors: increased vasomotor reactivity of BP and inadequate therapy of the disease. Evident markers of the negative prognosis are such simple indicators as orthostatic hypertension and increased variability of BP, the detection of which should alarm both the doctor and patient. Similar data describing the increase of short-term variability were also reported [14]. In this case, vasomotor reactivity may be one of the reasons for insufficient control of BP, thus requiring the use of individual approaches in the selection of therapy and disease control [15]. At the same time, strict control of blood pressure can improve the prognosis in patients with severe hypertension [16, 17] that is likely to be sought in this group of patients. Notably, the amount of antihypertensive drug groups prescribed for the treatment of stroke patients was the same as for others despite the higher BP and BPV in the former group.

It is worth pointing out that patients with negative prognosis characterized by reduced index Valsalva (which is a measure of cardiac reactivity), with orthostatic hypertension, and high BPV have high probability of hypertension progression. Therefore, they require increased attention from cardiologists to provide them with the best possible treatment. Probably, such a combination of indicators of

autonomic control should alert the attending doctor to require careful control of risk factors. It is noteworthy that all patients received not only optimal antihypertensive, but also lipid-lowering therapy and amount and dose of drugs prescribed for the treatment of patients who did not significantly differ in groups with a more severe and normal prognosis. Moreover, there was no difference in the level of cholesterol between these groups.

Despite the fact that new cases of diabetes mellitus are associated with taking statins, which is consistent with the literature data [18], this condition is not accompanied by the development of severe complications of the hypertension over a sufficiently long period of observation. Considering that dyslipidemia contributes to the hypertension progression (which is especially pronounced under conditions of changes in cardiac and vascular reactivity), taking statins is justified for this group of patients with an unfavorable combination of risk factors in spite of the threat of the development of diabetes mellitus.

5. Perspectives

In this study, we have shown that along with well-known factors, such as hypercholesterolemia and high blood pressure level, the prognosis of hypertensive patients is influenced by regulatory and hemodynamic parameters. Variations of the indicators of autonomic regulation (such as diminished Valsalva indices and vasomotor reactivity, inadequate orthostatic reaction, increased BPV, and total peripheral resistance, especially in combination with high blood pressure and cholesterol level) are associated with the development of life-threatening complications in hypertensive patients as well. Although these indicators are very informative, they are not evaluated during the routine examination of patients with cardiovascular diseases. The cause of unfavorable changes of autonomic regulation of blood circulation in these patients remains unclear; nonetheless, their use as indicators of disease prognosis could be of great practical importance and serve as a signal for intensification of therapy. These changes require both the closer control of blood pressure and prescription of cholesterol-decreasing medicine. The main limitation of the study is that it was carried out in a small cohort of hypertensive patients. Therefore, further investigation of the observed phenomena should be performed in a larger population by multicenter study. Moreover, detailed research aimed to understand the reasons of unfavorable changes of systemic hemodynamic and autonomic regulation is to be carried out. It is also necessary to conduct a research, the purpose of which would be to study the long-term effects of adequate correction of hemodynamic parameters and lipid metabolism in terms of autonomic

regulation and their relationship to outcomes in patients with hypertension not complicated by severe myocardial dysfunction.

Abbreviations

ABR: Arterial baroreflex
ACC: Associated clinical conditions
BP: Blood pressure
BPV: Blood pressure variability
ECG: Electrocardiogram
TPR: Total peripheral resistance.

Data Availability

The data sets supporting the conclusions of this article are included within the article.

Conflicts of Interest

The authors declare that they have no conflicts of interest.

References

[1] World Health Organization, *Mortality and Burden of Disease Attributable to Selected Major Risks*, World Health Organization (WHO), Geneva, Switzerland, 2009.

[2] H. Kanegae, T. Oikawa, K. Suzuki, Y. Okawara, and K. Kario, "Developing and validating a new precise risk-prediction model for new-onset hypertension: the Jichi Genki hypertension prediction model (JG model)," *The Journal of Clinical Hypertension*, vol. 20, no. 5, pp. 880–890, 2018.

[3] N. J. Nokoff, S. Scarbro, E. Juarez-Colunga, K. L. Moreau, and A. Kempe, "Health and cardiometabolic disease in transgender adults in the United States: behavioral risk factor surveillance system 2015," *Journal of the Endocrine Society*, vol. 2, no. 4, pp. 349–360, 2018.

[4] J. J. Goldberger, M. E. Cain, S. H. Hohnloser et al., "American heart association/American College of Cardiology foundation/heart rhythm society scientific statement on noninvasive risk stratification techniques for identifying patients at risk for sudden cardiac death," *Circulation*, vol. 118, no. 14, pp. 1497–1518, 2008.

[5] H. J. J. Wellens, P. J. Schwartz, F. W. Lindemans et al., "Risk stratification for sudden cardiac death: current status and challenges for the future," *European Heart Journal*, vol. 35, no. 25, pp. 1642–1651, 2014.

[6] M. J. Boogers, C. J. W. Borleffs, M. M. Henneman et al., "Cardiac sympathetic denervation assessed with 123-iodine metaiodobenzylguanidine imaging predicts ventricular arrhythmias in implantable cardioverter-defibrillator patients," *Journal of the American College of Cardiology*, vol. 55, no. 24, pp. 2769–2777, 2010.

[7] A. F. Jacobson, R. Senior, M. D. Cerqueira et al., "Myocardial iodine-123 meta-iodobenzylguanidine imaging and cardiac events in heart failure," *Journal of the American College of Cardiology*, vol. 55, no. 20, pp. 2212–2221, 2010.

[8] A. Bauer, "Identifying high-risk post-infarction patients by autonomic testing—below the tip of the iceberg," *International Journal of Cardiology*, vol. 237, pp. 19–21, 2017.

[9] M. T. La Rovere, G. D. Pinna, R. Maestri et al., "Prognostic implications of baroreflex sensitivity in heart failure patients in the beta-blocking era," *Journal of the American College of Cardiology*, vol. 53, no. 2, pp. 193–199, 2009.

[10] R. T. Munhoz, C. E. Negrão, A. C. P. Barretto et al., "Microneurografia e pletismografia de oclusão venosa na insuficiência cardíaca: correlação com prognóstico," *Arquivos Brasileiros de Cardiologia*, vol. 92, no. 1, pp. 46–53, 2009.

[11] Y. Zhou, S.-J. Ke, X.-P. Qiu, and L.-B. Liu, "Prevalence, risk factors, and prognosis of orthostatic hypotension in diabetic patients: a systematic review and meta-analysis," *Medicine (Baltimore)*, vol. 96, no. 36, p. e8004, 2017.

[12] A. C. Arnold and I. Biaggioni, "Management approaches to hypertension in autonomic failure," *Current Opinion in Nephrology and Hypertension*, vol. 21, no. 5, pp. 481–485, 2012.

[13] K. Nishisato, A. Hashimoto, T. Nakata et al., "Impaired cardiac sympathetic innervation and myocardial perfusion are related to lethal arrhythmia: quantification of cardiac tracers in patients with ICDs," *Journal of Nuclear Medicine*, vol. 51, no. 8, pp. 1241–1249, 2010.

[14] A. J. S. Webb, S. Mazzucco, L. Li, and P. M. Rothwell, "Prognostic significance of blood pressure variability on beat-to-beat monitoring after transient ischemic attack and stroke," *Stroke*, vol. 49, no. 1, pp. 62–67, 2018.

[15] Y. Tao, J. Xu, B. Song et al., "Short-term blood pressure variability and long-term blood pressure variability: which one is a reliable predictor for recurrent stroke," *Journal of Human Hypertension*, vol. 31, no. 9, pp. 568–573, 2017.

[16] A. de Simoni, W. Hardeman, J. Mant et al., "Trials to improve blood pressure through adherence to antihypertensives in stroke/TIA: systematic review and meta-analysis," *Journal of the American Heart Association*, vol. 2, no. 4, Article ID e000251, 2013.

[17] C. L. Roumie, A. J. Zillich, D. M. Bravata et al., "Hypertension treatment intensification among stroke survivors with uncontrolled blood pressure," *Stroke*, vol. 46, no. 2, pp. 465–470, 2015.

[18] M. Ruscica, C. Macchi, B. Morlotti, C. R. Sirtori, and P. Magni, "Statin therapy and related risk of new-onset type 2 diabetes mellitus," *European Journal of Internal Medicine*, vol. 25, no. 5, pp. 401–406, 2014.

Research Article

Advances in Hemodynamic Analysis in Cardiovascular Diseases Investigation of Energetic Characteristics of Adult and Pediatric Sputnik Left Ventricular Assist Devices during Mock Circulation Support

Alexander A. Pugovkin (ID),[1,2] **Aleksandr G. Markov,**[2] **Sergey V. Selishchev,**[1] **Leonie Korn,**[3] **Marian Walter,**[3] **Steffen Leonhardt,**[3] **Leo A. Bockeria,**[4] **Olga L. Bockeria,**[4] **and Dmitry V. Telyshev**[1,2]

[1]*Institute for Biomedical Systems, National Research University of Electronic Technology, Zelenograd 124498, Moscow, Russia*
[2]*Institute for Bionic Technologies and Engineering, I. M. Sechenov First Moscow State Medical University, 119991 Moscow, Russia*
[3]*Medical Information Technology, RWTH Aachen, 52074 Aachen, Germany*
[4]*Bakulev Center for Cardiovascular Surgery, 121552 Moscow, Russia*

Correspondence should be addressed to Alexander A. Pugovkin; pugovkin@bms.zone

The need to simulate the operating conditions of the human body is a key factor in every study and engineering process of a bioengineering device developed for implantation. In the present paper, we describe in detail the interaction between the left ventricle (LV) and our Sputnik left ventricular assist devices (LVADs). This research aims to evaluate the influence of different rotary blood pumps (RBPs) on the LV depending on the degree of heart failure (HF), in order to investigate energetic characteristics of the LV-LVAD interaction and to estimate main parameters of left ventricular unloading. We investigate energetic characteristics of adult Sputnik 1 and Sputnik 2 LVADs connected to a hybrid adult mock circulation (HAMC) and also for the Sputnik pediatric rotary blood pump (PRBP) connected to a pediatric mock circulation (PMC). A major improvement of the LV unloading is observed during all simulations for each particular heart failure state when connected to the LVAD, with sequential pump speed increased within 5000–10000 rpm for adult LVADs and 6000–13000 rpm for PRBP with 200 rpm step. Additionally, it was found that depending on the degree of heart failure, LVADs influence the LV in different ways and a significant support level cannot be achieved without the aortic valve closure. Furthermore, this study expands the information on LV-LVAD interaction, which leads to the optimization of the RBP speed rate control in clinics for adult and pediatric patients suffering from heart failure. Finally, we show that the implementation of control algorithms using the modulation of the RBP speed in order to open the aortic valve and unload the LV more efficiently is necessary and will be content of further research.

1. Introduction

Nowadays, about 8 million people in Russia suffer from heart failure (HF), and among them, approximately 2.5 million have acute HF (classes III and IV of the New York Heart Association (NYHA) classification of heart failure), which tends to be the most widespread cause for hospitalization and lethal outcome of heart diseases [1–3].

Left ventricular assist devices (LVADs) were designed as a therapeutic option to treat end stage HF patients in response to the large patient populations with acute HF along with limited number of donor hearts. Initially, LVADs were designed as pulsatile blood pumps to support or replace the native ventricle. Eventually, LVADs evolved to rotary blood pumps (RBPs) providing continuous flow to maintain temporary and permanent circulatory support [4, 5].

Implantation of a LVAD leads to a dynamic interaction between the cardiovascular system and the LVAD, where the LVAD is unloading the ventricle via undertaking part of the load and in some cases causing its recovery. In its turn, the ventricle function influences the performance of the LVAD [6]. In order to evaluate this interaction, in particular ventricular unloading and recovery, the following energetic characteristics are described in the literature: stroke work (SW), hydraulic pump work, and cardiac mechanical efficiency [7–9].

Investigation of in vitro dynamic of LVAD is of importance due to its influence on the LVAD patients' outcome. It has been shown that the introduction of energetic parameters could lead to improved cardiac mechanical efficiency [10]. Moreover, proper assessment of LVAD dynamic leads to decreased LV afterload and improved LV mechanical performance (i.e., increased ejection fraction, stroke volume, cardiac output, and maximum elastance) [11]. Finally, there have been made investigations of pulsatile operating conditions which showed that there is a variable phase relationship between LVAD differential pressure and LVAD flow, which is important for clinical use [12].

The clinical importance of pulsatility is a recurring topic of debate in mechanical circulatory support. Lack of pulsatility has been identified as a possible factor responsible for adverse events and has also demonstrated a role in myocardial perfusion and cardiac recovery. Moreover, additional benefits of pulsatile ventricular assist devices (VADs) over continuous-flow systems are the greater likelihood of aortic valve opening. Investigation on the dynamics and characteristics of the LVAD and the pulmonary artery pulsatile index is also of importance due to the possibility to predict the risk of the gastrointestinal bleeding in patients with LVAD [13]. This issue of gastrointestinal bleeding (GIB) occurs primarily from arteriovenous malformations or ulcers [14].

The interaction between the left ventricle (LV) and the RBP can be examined via pressure-volume (P-V) diagram of the ventricle as the stroke work can be expressed by the area inside P-V diagram. In addition, dynamic head pressure-bypass flow (H-Q) curves of the pump are a strong tool for the evaluation of the LV-LVAD interaction, since dynamic H-Q curves describe RPB behavior during the cardiac cycle [15]. Also, the stroke work of the ventricle expressed by the area inside the P-V diagram strongly correlates with the area inside dynamic H-Q curves [6].

In this study, the interaction between different Sputnik LVADs and the LV with various degrees of HF was investigated. The evaluated LVADs are the adult Sputnik 1 and Sputnik 2, and furthermore, the Sputnik pediatric RBP (PRBP) was engineered for pediatric patients with a body weight between 12 and 40 kg. This research is aimed (i) to evaluate the Sputnik LVADs and Sputnik PRBP influence on the LV depending on the HF degree, (ii) to estimate main parameters of the LV unloading, (iii) to investigate energetic characteristics of the LV-LVAD interaction for the adult Sputnik LVADs and for the Sputnik PRBP, and finally (iv) to compare this between two generations of adult LVADs. This research is intended to expand the information on LV-LVAD interaction in order to optimize the choice of RBP speed rate control in the clinic regarding the degree of heart failure in adult and pediatric patients.

2. Materials and Methods

In this work, energetic characteristics of (i) Sputnik 1 and (ii) Sputnik 2 connected to a hybrid adult mock circulation (HAMC) [5] and (iii) Sputnik PRBP connected to a pediatric mock circulation (PMC) [16] were investigated.

Herein, in this work, we describe two various mock loops with two different working fluids. The dynamic viscosity of the fluid in the HAMC is around 2.5 MPa s at 298.15 K, whereas the dynamic viscosity of the fluid in the PMC is 2.38 MPa s at 299.25 K. Both are within the physiological range of blood viscosity, so the results are comparable.

2.1. Sputnik LVAD of Generation 1. The Sputnik 1 LVAD configuration is based on an axial-flow blood pump with nonpulsatile flow. This device can provide a flow rate up to 10 l/min.

The profile of the blood pump is provided in Figure 1. The pump consists of two major parts: (i) a hydraulic and (ii) an electric. The hydraulic machine in its turn consists of an impeller (a rotor with 4 blades), a flow straightener with three blades, and a diffuser. An external power supply is used to drive the pump. This driving unit has two wearable batteries. The driver unit is connected to the pump by a percutaneous cable. An impeller with a permanent NdFeB magnet actuated by a brushless DC motor provides the blood flow through the Sputnik 1 LVAD. A stator is enclosed in a thin-walled titanium housing. The blood flow is directed by three inlet blades to the rotating impeller blades, minimizing the whirl flows. After this, blood flows into the diffuser. A diffuser consists of 3 twisted blades located at the pump outlet. These inlet and outlet elements have two different needle bearings: the inlet and the outlet. An impeller is suspended between these bearings.

The length of Sputnik 1 LVAD pump is 82 mm, the maximum pump diameter is 34 mm, the flow channel diameter is 16 mm, the impeller diameter is 15.6 mm, and finally the weight of the construction is 246 g [17].

2.2. Sputnik LVAD of Generation 2. Eventually, the Sputnik 1 LVAD was modified into Sputnik 2 LVAD. The bearing mountings of the flow straightener and diffuser were reduced significantly. The design of the diffuser was changed in order to exclude the rotor taper unit expansion and also to reduce the weight and the size of the pump. The distance between the impeller and the diffuser was changed from 20 mm to 3.6 mm. The pressure head, as a result, was increased with the decrease in distance [18]. The overall changes bring the possibility to decrease the pump's length. The rotor was tightened by 2 repelling magnets in the outlet bearing. Therefore, during on and off states of the device, a permanent surface contact is formed. Schematic and geometry of the diffuser of the first and second generations of
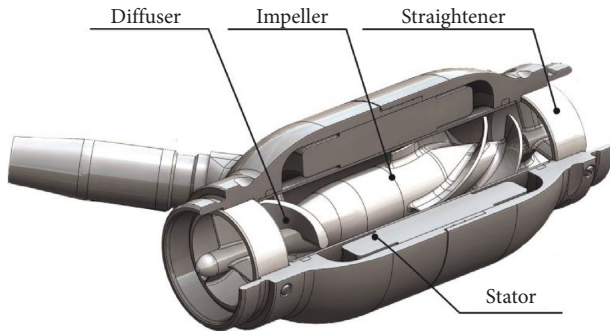
FIGURE 1: Profile of the Sputnik LVAD first-generation model. Four major parts of the device: (i) a straightener, (ii) a stator, (iii) an impeller, and (iv) a diffuser.

FIGURE 2: Schematic (bottom) and geometry (top) of the hydraulic part of the Sputnik PRBP.

the Sputnik LVADs are demonstrated in the work of Selishchev and Telyshev [19].

The implantable pump length was decreased from 81 mm (the HMII and HA5 lengths are 81 and 71 mm, respectively) to 66 mm. The maximum diameter was decreased from 34 mm (the HMII and HA5 maximum diameters are 43 and 30 mm, respectively) to 29 mm [20]. The diameter of the impeller was decreased from 15.6 mm to 13.8 mm, and the pump weight from 246 g to 205 g. Finally, a new geometry of the diffuser and the modification of the rotor design allowed to reduce the energy consumption of the device.

2.3. Sputnik PRBP.

The necessity to develop a device for pediatric patients imposed many obstacles. Therefore, the first phase of the Sputnik PRBP design involved the detailed elaboration of requirements for the pediatric patients, which significantly differed from the adult group [21]. The two main differences of the cardiovascular system in pediatric patients compared to adults are (i) a higher heart rate and (ii) lower arterial blood pressure. Another key factor is the cardiac output, which is noticeably increased in adult patients [22].

The working principle and design features of Sputnik PRBP are described in detail in the work of Dr. Telyshev et al [23]. Herein, we follow the methods of Dr. Telyshev to list these features. A construction scheme that was successfully used for development of the two adult Sputnik LVADs was utilized as a basis for the Sputnik PRBP development. As shown in Figure 2, hydraulic part of the Sputnik PRBP consists of a fixed flow tube containing the main components of the pump: (i) a fixed flow straightener at the input, (ii) an impeller with an embedded magnet allocating a rotational speed of several thousands of revolution per minute (rpm), and (iii) a fixed diffuser at the output. The flow straightener has three blades arranged at an angle of 120° to each other. To reduce the residence time of blood cells in the pump, the distance between the back edge of the impeller blades and the front edge of the diffuser blades was decreased from 20 mm (Sputnik 1 LVAD) to 6.5 mm. It is presumed that with a reduction of the residence time of blood in the pump, the risk of blood trauma decreases and, therefore, the pump's biocompatibility increases. The lowest hemolysis
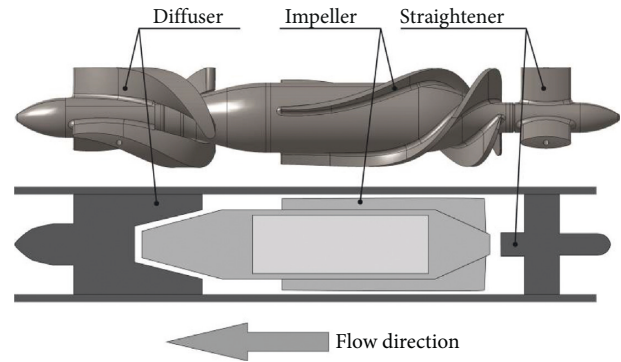
index was observed when the distance between the impeller and diffuser was 2 mm or 6 mm. A flow rate of 2.4 l/min is defined as an operating point of the Sputnik PRBP. The use of the adult Sputnik LVAD at this operating point unavoidably leads to decreased velocity of blood cells in the pump [18] and hence to an increased residence time, providing increased probability of blood cell trauma. The Sputnik PRBP has the following geometrical specifications: flow unit length of 51.5 mm, flow unit diameter of 10 mm, and spacing between the rotor blades and housing of 0.1 mm.

The main parts of the pump are made of titanium alloy, whereas the bearings used in the pump are made of CoMoCr alloy, as in the adult Sputnik LVADs. Moreover, the rotor of the Sputnik PRBP contains a permanent NdFeB magnet actuated by a brushless DC motor, the same as used in the first and second generations of the adult Sputnik LVADs.

Thus, Sputnik PRBP is suitable for pediatric patients with body weight of 12–40 kg.

2.4. Hybrid Adult Mock Circulation.

For the study of the adult Sputnik LVADs, a mock circulation loop [5] based on a numerical cardiovascular model for adults was used [24]. In the experiment, the device is connected to a real-time computer (DS1103, dSPACE GmbH, Paderborn, Germany) via a hydrodynamic interface using the Hardware in the Loop (HIL) concept. High-bandwidth actuators are used to control the left ventricular and the aortic pressure in the test bench while the pump flow is fed back into the numerical simulation (Figure 3).

In comparison to classical mock circulation loops, herein the heart and the cardiovascular system are exclusively modeled in the numerical domain and transferred into the physical domain as set points for the pump inlet and outlet. The cardiovascular system simulation is implemented as a simplified version of the model from [24] in the software Simulink. Eight ordinary differential equations and eight state variables are used to model an actively contracting LV, including both the atrium and the ventricle. The control input is set to appear between a certain maximum and minimum flow level. Frank–Starling autoregulation mechanism of the heart is reproduced during the simulation. Physiological control loops like the baroreceptor reflex are
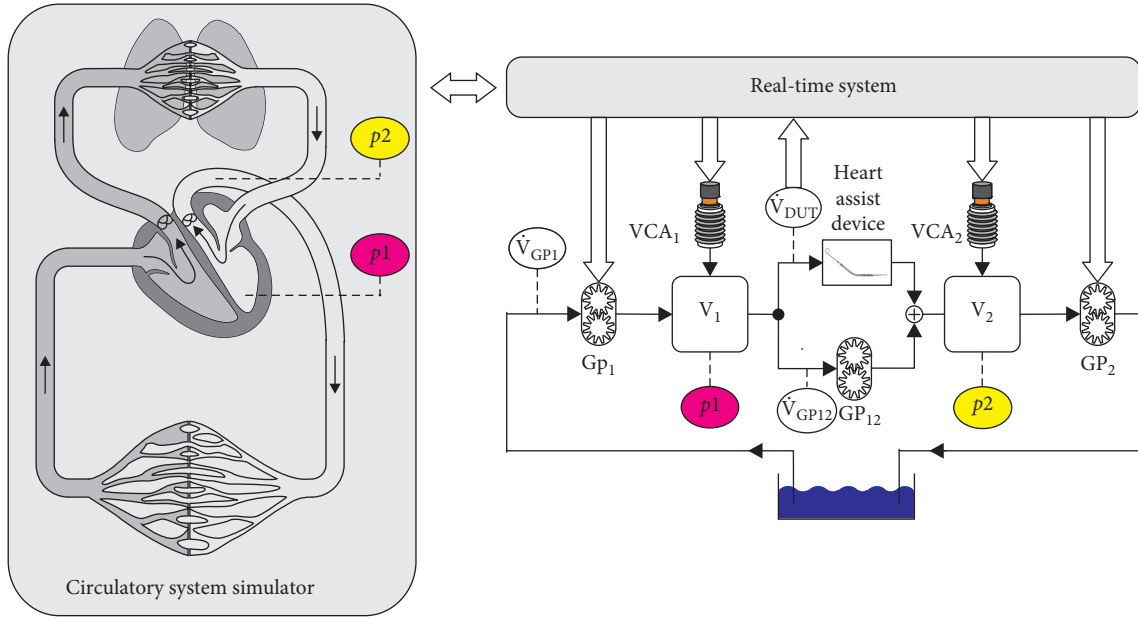
(a)
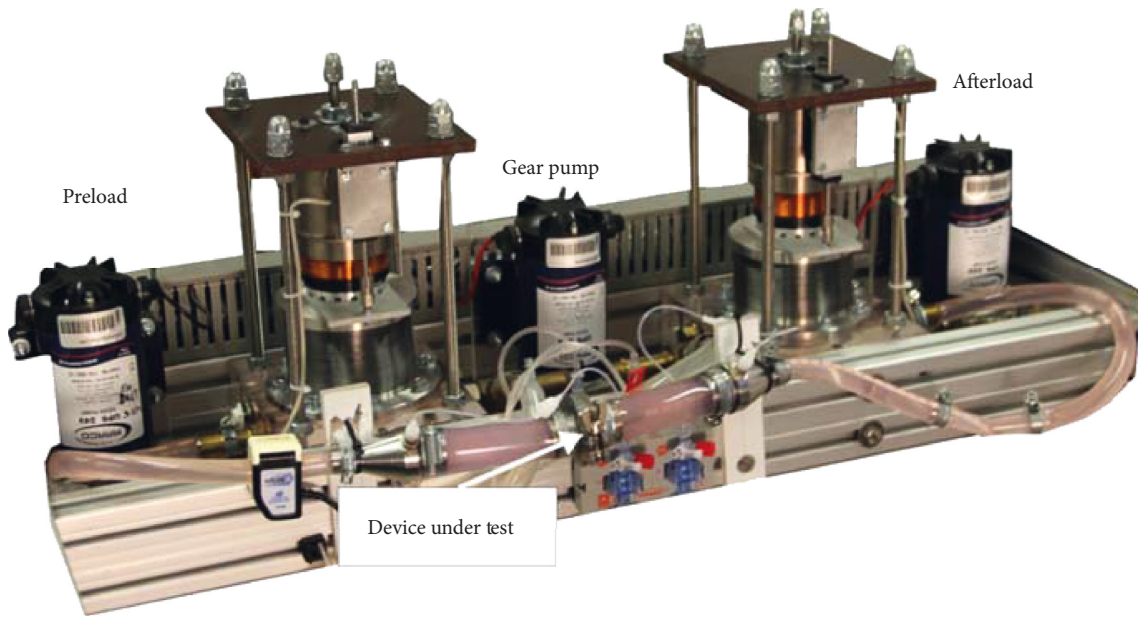
(b)

FIGURE 3: (a) Hydrodynamic system simulator (right) coupled to the circulatory system simulation (left). The left ventricular pressure p1 (preload) and the aortic arch pressure p2 (afterload) are calculated via the simulation and used as reference values for the hybrid adult mock circulation. Measured values in the experimental setup are indicated by ellipsoids, modified from the literature values. (b) Photo of the hybrid adult mock circulation (HAMC). The preload and afterload pressure compartments with the attached voice coil actuators can be seen as well as the three gear pumps providing the flow balance in the system. The device under test is mounted in the fixation in front. A detailed description of the system can be found in [3].

also modeled. The control of the cardiovascular system is responsible for the adaptation of the heart rate and the contractility of the ventricle. The transition between the end-diastolic and the end-systolic pressure to the volume $(P_{ed}(V), P_{es}(V))$ is modeled by chamber-specific time-varying elasticity functions $e(t)$, that result in the function of pressure $p(V, t)$ for each chamber.

$$p(V, t) = e(t) \cdot P_{es}(V) + (1 - e(t)) \cdot P_{ed}(V);$$
$$P_{es}(V) = \text{VCF} \cdot E_{es} \cdot (V(t) - V_u), \tag{1}$$

where E_{es} describes the chamber-specific elasticity and can be modified by the nondimensional contractility factor $0 < \text{VCF} \le 1$ and V_u describes the volume when the transmural

pressure is equal to zero and can be set individually for each chamber.

The hardware part of the mock circulation loop contains mainly two compartments made of polymethyl methacrylate and does not contain any valves, compliance chambers, or flow resistances. The chambers are actuated via voice coil actuators (VCAs) to reproduce fast pressure changes, whereas three gear pumps generate directed flow to keep the VCAs in the operating range. The adult mock circulation loop is capable to achieve an accuracy of ±1 mmHg and a settling time less than 20 ms. Invasive blood pressure sensors (Xtrans, CODAN pvb Critical Care GmbH, Forstinning, Germany) are used to measure pressures in two compartments, whereas an ultrasonic flow probe is utilized to determine the pump flow (H11XL, Transonic Systems Inc., Ithaca, USA). In addition, the hydrodynamic properties of blood are emulated with a glycol/water mixture (Glysofor N, Wittig Umweltchemie GmbH, Grafschaft-Ringen).

2.5. Pediatric Mock Circulation.

For the test under dynamic conditions with the Sputnik PRBP, a conventional pediatric mock circulation (see Figure 4) allowing for the simulation of physiological cardiovascular characteristics was utilized [16]. The simulation was automatized using NI cDAQ hardware and NI LabVIEW software. This system being a physical-based model of pediatric circulation reproduces the Frank–Starling autoregulation mechanism of the heart, which regulates the cardiac output depending on the ventricle preload. This can be expressed as end-diastolic pressure (EDP) or end-diastolic volume (EDV). The numerical model of the cardiovascular system was not used during trials of the Sputnik PRBP considering its inconsistence for pediatric conditions by the moment of trials.

The system in Figure 4 allows to simulate and control the cardiovascular circulation and consists of a pediatric systemic circulation loop (PSCL), a pneumatic system, and the data acquisition system. The PSCL consists of an artificial ventricle (AV) (Medos LVAD; Medos Medizintechnik AG, Stolberg, Germany), two containers reproducing lumped vascular parameters, and an adjustable clamp to reproduce the systemic vascular resistance. All components of the PSCL are connected in series with flexible polyvinyl chloride laboratory tubes (TYGON E-3603; Compagnie de Saint-Gobain, Courbevoie, Ile-de-France, France), with an inner diameter of 12.7 mm.

The left pulsatile AV has a nominal volume of 72 ml corresponding to a dilated pediatric ventricle volume. It is a pump pneumatically driven by a membrane that simulates the heartbeat using the pneumatic control system. The pulsatile AV has an inlet and an outlet valve to prevent reverse flow of fluid into the hydraulic circuit. A 32% aqueous glycerol solution is used in the PSCL as the model fluid. This configuration of the mock circulation allows simulating normal pediatric systemic circulation and heart failure state. It should be clarified here that under the normal state, we mean summation of LV failure state with connected LVAD, and this applies to both flow and work. The left AV also has a second outlet providing the connection between the Sputnik PRBP inlet and the ventricle. The Sputnik PRBP outlet is connected to the aortic container. Before testing the Sputnik PRBP behavior and its influence on the system, the pump connection line was closed with a special flow restrictor.

The pneumatic system including a pneumatic station and a pneumatic control unit is used to control the AV contraction through an electronic control system based on combined NI cDAQ-9174 and NI 9264 hardware implemented with the NI LabVIEW software (National Instruments Corporation, Austin, Texas, USA). The contractility level of the pulsatile AV can be varied by altering the control signal amplitude and frequency. The Frank–Starling mechanism is reproduced by using EDP as a preload parameter in feedback.

The data acquisition system consists of a pressure measurement system, a flow measurement system, and a data processing system based on combined NI cDAQ-9174 and NI 9205 hardware and NI LabVIEW software.

2.6. Characteristics Analysis.

Adult LVADs characteristics were analyzed in two operation modes of the HAMC. Each operation mode is characterized by nondimensional ventricle contractility factors (VCFs) of 0.5 and 0.25. These two operation modes correspond to mild and congestive heart failure states, respectively. An acute heart failure state in pediatric patient with the body mass of 15.2 kg [25] was simulated on PMC to investigate the energetic characteristics of the Sputnik PRBP.

The energetic characteristics of Sputnik 1 and Sputnik 2 LVADs were obtained in a speed range of 5000–10000 rpm increasing in steps of 200 rpm. Sputnik PRBP operation was analyzed in the speed range of 6000–13000 rpm in steps of 200 rpm.

The left ventricular stroke work, LVAD hydraulic work, and total work investigated from the energetic characteristics can be described as follows:

$$A_{LV} = \oint P_{LV} dV_{LV}, \tag{2}$$

where P_{LV} is the left ventricular pressure and V_{LV} is the left ventricular volume.

$$A_{VAD} = \int (P_{out} - P_{in}) Q_{VAD} dt, \tag{3}$$

where P_{out} is the LVAD outlet pressure, P_{in} is the LVAD inlet pressure, and Q_{VAD} is the LVAD flow rate.

$$A_{Total} = A_{LV} + A_{pump}. \tag{4}$$

Left ventricular stroke work represents the area inside the closed contour formed by the left ventricular pressure-volume relationship. The LVAD hydraulic work, in its turn, is the time integral of the LVAD head pressure and flow rate product. Total work is the sum of the A_{LV} and A_{VAD}.

Also, the mean LVAD flow rate, the mean aortic valve flow rate, the end-diastolic volume, and the relationship between left ventricular stroke work and the LVAD hydraulic work were utilized to describe all simulated
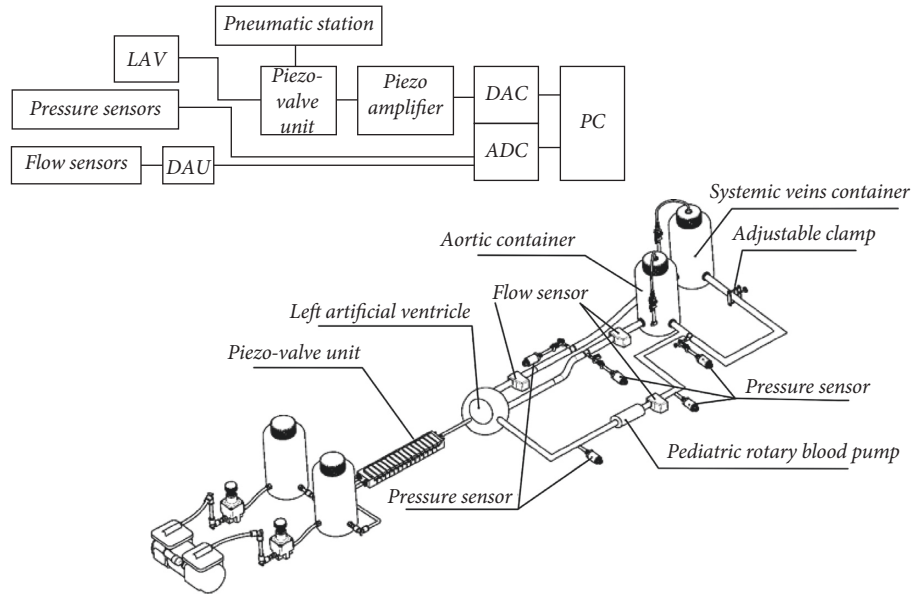
(a)
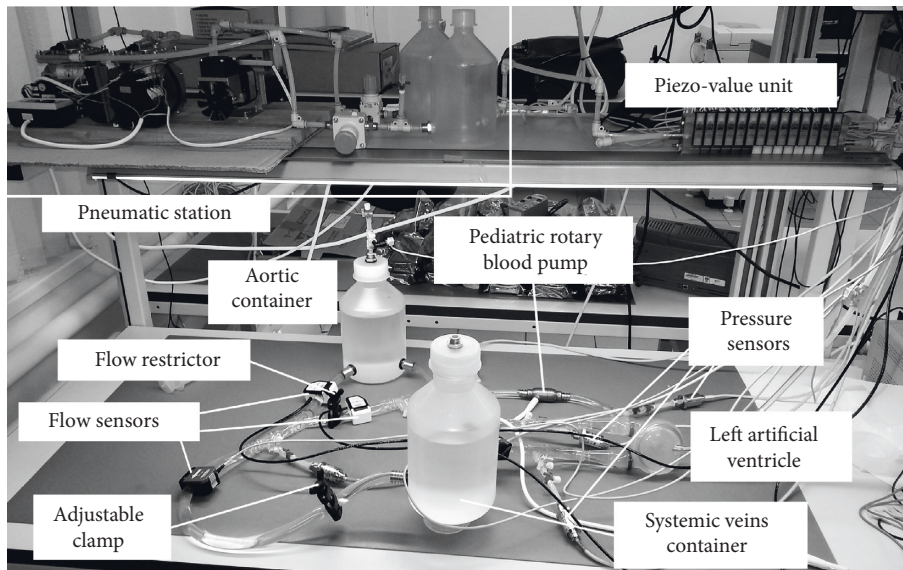
(b)

FIGURE 4: (a) Schematics of PMC showing main functional hardware blocks. LAV, left artificial ventricle; DAU, data acquisition unit; ADC, analog-to-digital converter; DAC, digital-to-analog converter; PC, personal computer. (b) Image of the pediatric mock circulation (PMC) simulating the acute heart failure with the Sputnik PRBP support. The flow direction is shown via an arrow.

conditions. The characteristics were calculated for each cardiac cycle on a sample of obtained experiment data and were averaged over all cardiac cycles in each simulated condition.

Furthermore, pulsatility indices of pump flow rates were analyzed:

$$PI_{Q_{\text{pump}}} = \frac{Q_{\text{pump}}^{\max} - Q_{\text{pump}}^{\min}}{Q_{\text{pump}}^{\text{av}}}, \tag{5}$$

where $Q_{\text{pump}}^{\max}$, $Q_{\text{pump}}^{\min}$, and $Q_{\text{pump}}^{\text{av}}$ are maximum, minimum, and average pump flow rates.

3. Results

Figures 5(a) and 5(c) represent average levels of LV stroke work, the hydraulic work of the Sputnik 1 LVAD, and the total work during support of the LV with VCFs of 0.5 and 0.25, respectively. Figures 5(b) and 5(d) show bar graphs of the average aortic valve and pump flow rates for the operation modes of the LV with VCFs of 0.5 and 0.25, respectively, in the pump speed range of 5000–10000 rpm increasing in steps of 200 rpm. Normal and heart failure state levels of stroke work and the aortic valve flow rate are also presented for comparison at the left side of each figure.
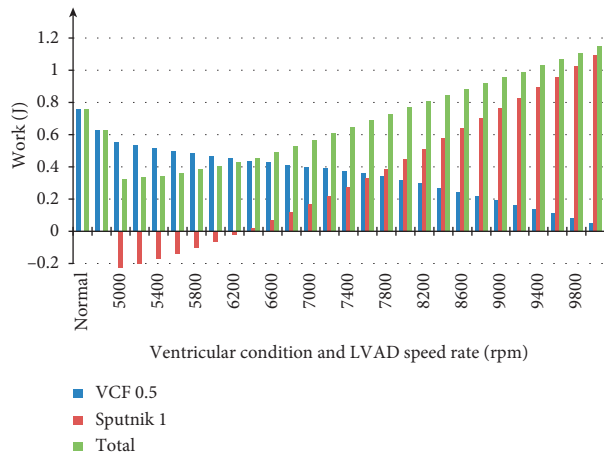
(a)
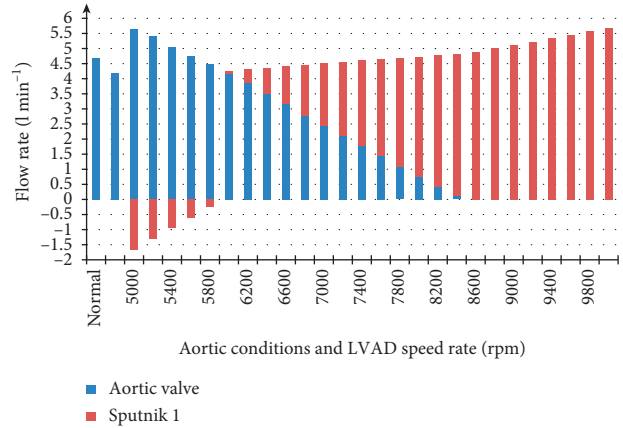
(b)
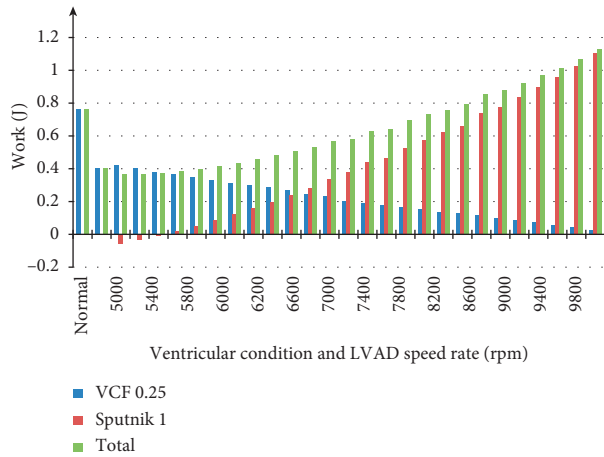
(c)
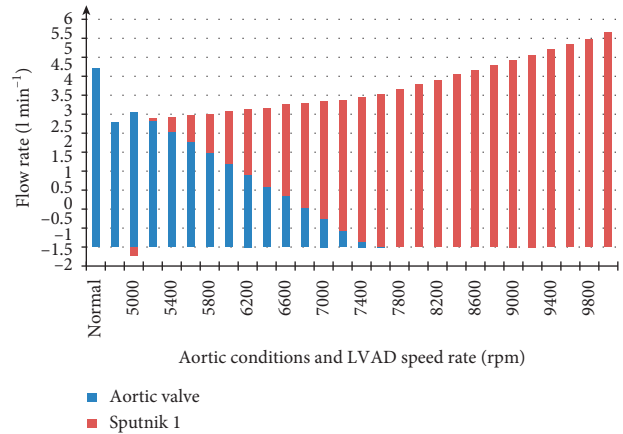
(d)

FIGURE 5: (a, c) Average levels of left ventricular stroke work, hydraulic pump work, and total work for Sputnik 1 LVAD supporting the adult LV with ventricular contractility factors (VCFs) of 0.5 and 0.25, respectively, in the pump speed range of 5000–10000 rpm with 200 rpm step. (b, d) Average aortic valve and pump flow rates with respect to normal, heart failure, and supported states in the pump speed ranges specified for Sputnik 1 LVAD supporting LV with VCFs of 0.5 and 0.25, respectively. Stroke work and aortic valve flow rates in normal and heart failure states are presented for comparison.

The work of the Sputnik 1 pump intersects with zero in the speed range of 6200–6400 rpm for a VCF of 0.5 and at 5400–5600 rpm for a VCF of 0.25 (Figures 5(a) and 5(c)). The total work reaches a value of the normal LV work equal to 0.76 J at 8000 rpm and 8400 rpm for VCFs of 0.5 and 0.25, respectively.

Figures 5(b) and 5(d) show that the total average flow rates for VCFs of 0.5 and 0.25 are equal to the normal LV flow rate in the speed ranges of 7800–8000 rpm and 8600–8800 rpm, respectively. While the ventricle is still actively pumping, partial support takes place as it changes to full support when the aortic valve closes and the ventricle stops pumping. This happens at 8600 rpm and 7600 rpm for VCFs of 0.5 and 0.25, respectively.

Figures 6(a) and 6(c) represent the average levels of left ventricular work, the hydraulic work of the Sputnik 2 LVAD, and the total work during support of the LV with VCFs of 0.5

and 0.25, respectively. Figures 6(b) and 6(d) show bar graphs of the average aortic valve and pump flow rates for LV operation modes with VCFs of 0.5 and 0.25 with respect to each figure. The pump speed range has been set to 5000–10000 rpm increased by 200 rpm per step.

Sputnik 2 pump work intersects with zero in the speed ranges of 6400–6600 rpm and 5600–5800 rpm for VCFs of 0.5 and 0.25, respectively (Figures 6(a) and 6(c)). The total work equals to the LV work in normal state at 7800 rpm and 8400 rpm for a VCF of 0.5 and 0.25, respectively.
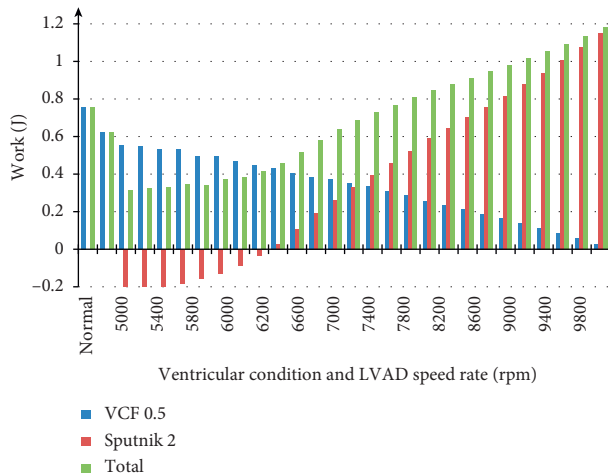
Figures 6(b) and 6(d) show that the total average flow rates equal to the normal LV flow rate in the speed ranges of 7600–7800 rpm and 8400–8600 rpm, respectively. The partial support state of the Sputnik 2 LVAD changes to full support state at 8400 and 7400 rpm for VCFs of 0.5 and 0.25, respectively.

(a)
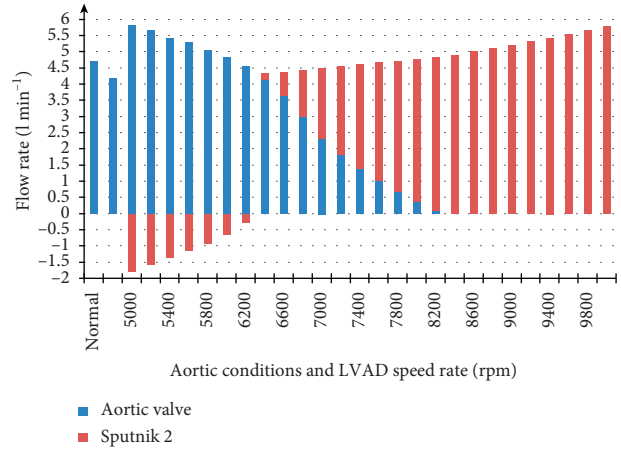
(b)
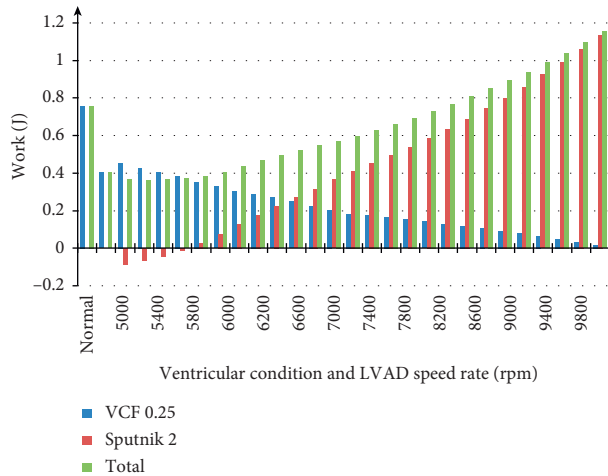
(c)
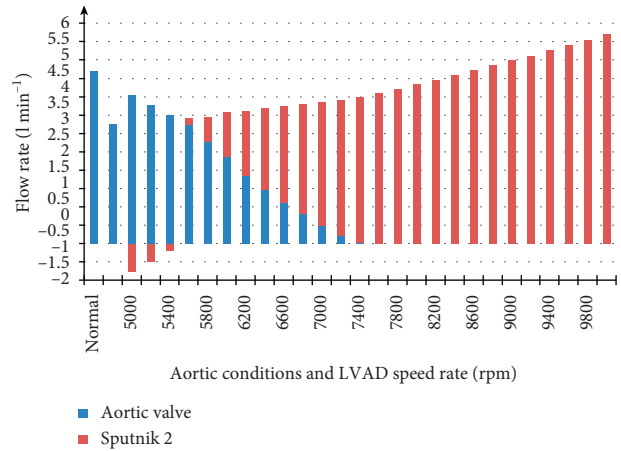
(d)

FIGURE 6: (a, c) Average levels of left ventricular work, hydraulic pump work, and total work during Sputnik 2 LVAD support with ventricle contractility factors (VCFs) of 0.5 and 0.25, respectively, in the pump speed range of 5000–10000 rpm with 200 rpm step. (b, d) Average aortic valve and pump flow rates with respect to normal, heart failure, and supported states in the pump speed ranges specified for Sputnik 2 LVAD supporting LV with VCFs of 0.5 and 0.25, respectively. Stroke work and aortic valve flow rates in normal and heart failure states are presented for comparison.

We chose one of the Medos VAD ventricles the aortic valve leaflets of which are prolapsed as an overload on the aortic valve increase. Thus, aortic back flow is reached after a certain pump speed.

Figure 7 represents the average levels of LV work, the hydraulic work of the Sputnik PRBP, and the total work. In addition, a bar graph of the average aortic valve and pump flow rates simulated in the PMC with an acute heart failure state in the pediatric patient with a body mass of 15.2 kg is shown in the pump speed range of 6000–13000 rpm with 200 rpm step.

Figure 7(a) shows that Sputnik PRBP hydraulic work intersects with zero in a pump speed range of 6800–7000 rpm. The total work reaches the normal LV work at 11200 rpm. Figure 7(b) shows that the total average flow rate equals to the normal LV flow rate at a pump speed of

11400 rpm. Sputnik PRBP partial support state changes to full support at a speed of 9400 rpm. The aortic back flow appears at a speed of 9400 rpm and the maximum of aortic back flow is reached at 13000 rpm.

Figure 8(a) represents the relationship between average stroke and pump work for Sputnik 1 and Sputnik 2 LVADs supporting the LV with VCFs of 0.5 and 0.25 and the Sputnik PRBP supporting the pediatric LV in the acute heart failure state. Figure 8(b) shows the relationship between the end-diastolic volume (EDV) and the average stroke work for adult and pediatric LVs during support. Figure 8(c) represents pump flow rate pulsatility indices for Sputnik 1 and Sputnik 2 LVADs supporting the adult LV with VCFs of 0.5 and 0.25 in the speed range of 7000–10000 rpm in steps of 200 rpm. Furthermore, the Sputnik PRBP support in failing pediatric LV in the speed range of 7000–13000 rpm with
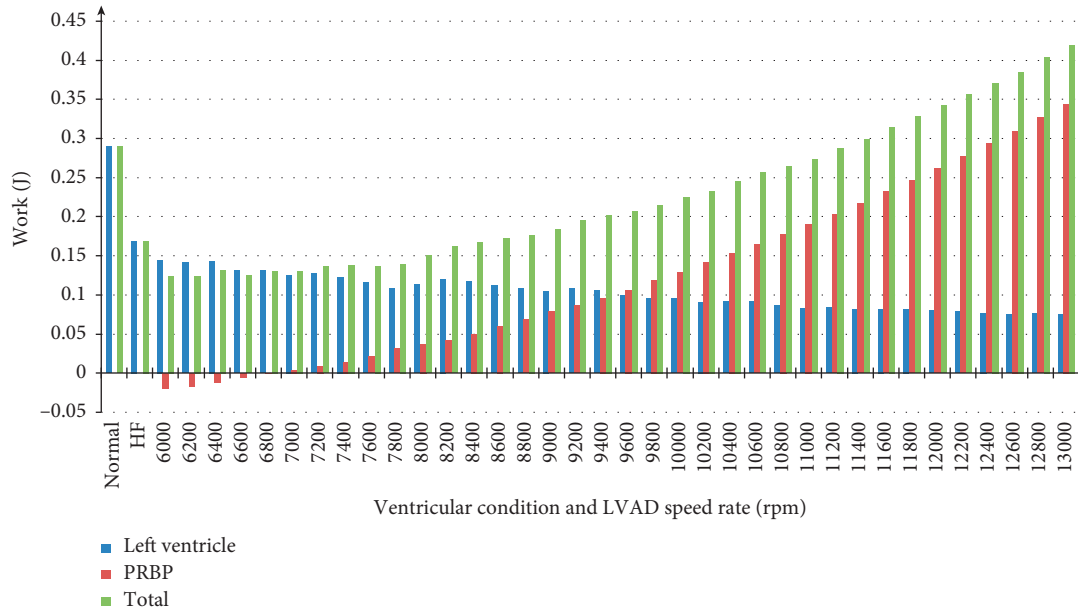
(a)
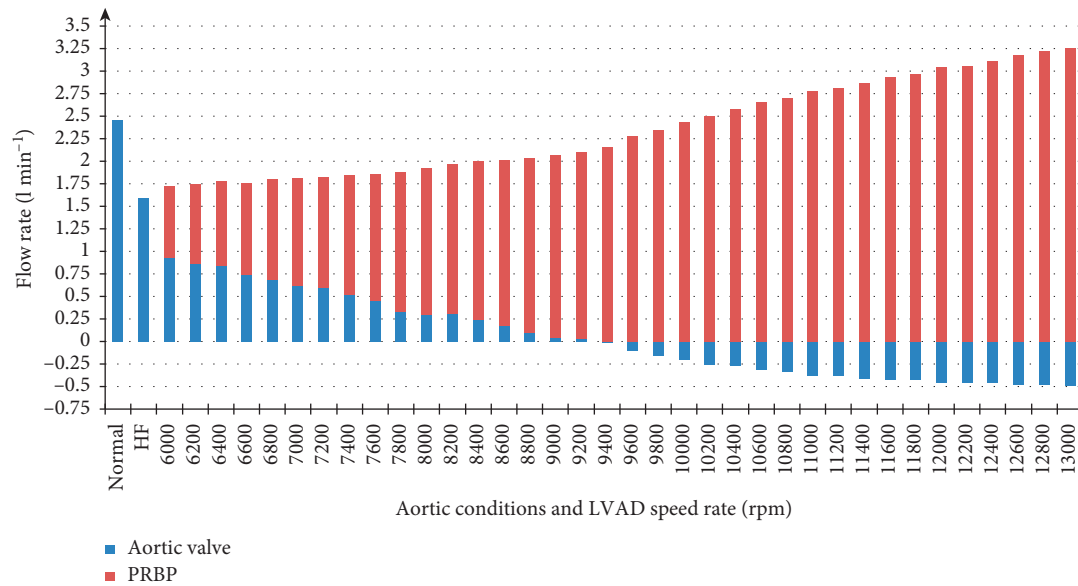
(b)

FIGURE 7: (a) Average levels of left ventricle work, PRBP work, and total work for simulated state of acute heart failure in 2-year-old pediatric patient with mass of 15.2 kg in the pump speed range of 6000–13000 rpm with 200 rpm step. Levels of left ventricle work in normal and heart failure states are also represented for comparison. (b) Average aortic valve and pump flow rates with respect to normal state, heart failure, and states in the pump speed range specified.

200 rpm steps is depicted. Also, Figure 8(d) shows EDV of the left ventricle during support by Sputnik 1 and Sputnik 2 LVADs in a speed range of 5000–10000 rpm (steps of 200 rpm) and Sputnik PRBP in the speed range of 6000–13000 rpm (steps of 200 rpm), respectively.

Relations represented in Figure 8 are almost the same for Sputnik 1 and Sputnik 2 LVADs in corresponding ventricular states with VCFs of 0.5 and 0.25. Figure 8(a) shows that the stroke work may depend on pump work as they are inversely proportional. Figure 8(b) shows that EDV increases with stroke work. All pump flow rate pulsatility indices and the EDV decrease with pump speed for all presented RBPs.

Figure 9 represents time courses of the LV pressure and volume and the aortic pressure for moderate and congestive heart failure states simulated in the HAMC with and without the support of the adult Sputnik LVADs. It is shown that for Sputnik 1 (Figures 9(a) and 9(b) and Sputnik 2 (Figures 9(c) and 9(d)), as the rotor speed increases, the systolic pressure in the ventricle decreases and the volume curve moves towards decreasing end-systolic and end-diastolic volume. In addition, the aortic pressure increases, but the pulse pressure
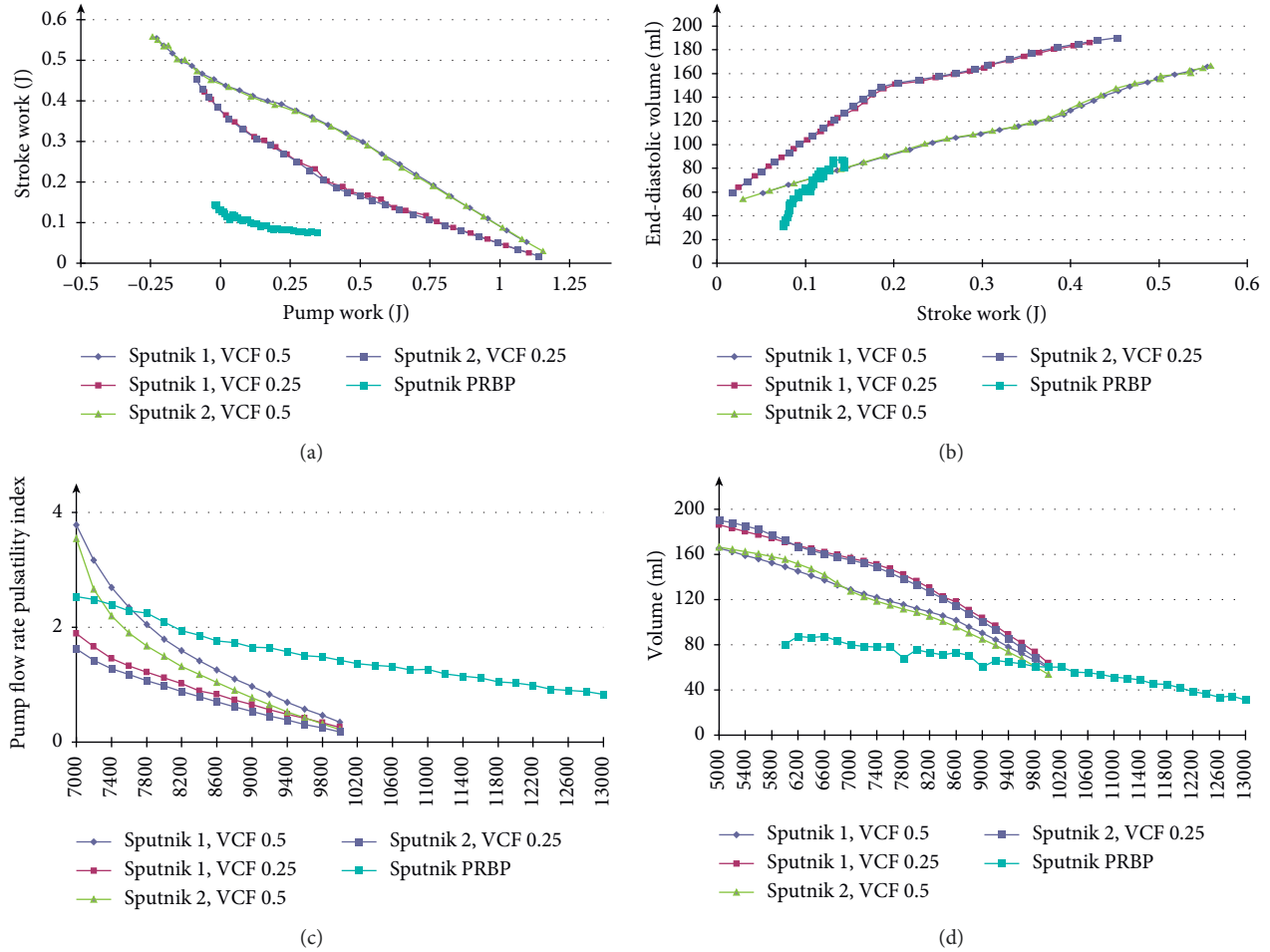
(a)

(b)

(c)

(d)

Figure 8: (a) Relationship between average stroke work and average hydraulic pump work for Sputnik 1 and Sputnik 2 LVADs supporting left ventricle with ventricle contractility factors (VCFs) of 0.5 and 0.25 and for Sputnik PRBP supporting pediatric left ventricle. (b) Relationships between end-diastolic volume and average stroke work for adult and pediatric LV supported by Sputnik 1, Sputnik 2 LVADs, and Sputnik PRBP, respectively. (c) Pump flow rate pulsatility indices for Sputnik 1 and Sputnik 2 LVADs supporting left ventricle with ventricle contractility factors (VCFs) of 0.5 and 0.25 and Sputnik PRBP supporting pediatric left ventricle in the speed ranges of 7000–10000 rpm and 7000–13000 rpm, respectively, with 200 rpm step. (d) End-diastolic volumes of left ventricle during support by Sputnik 1 and Sputnik 2 LVADs and Sputnik PRBP in the speed ranges of 5000–10000 rpm and 6000–13000 rpm, respectively, with 200 rpm step.

decreases with increasing pump speed due to its constancy. These changes indicate the unloading of the ventricle and the improvement of hemodynamics due to an increase in the average pressure in the aorta.

Figure 10 represents the time courses of the LV pressure and volume and the aortic pressure for acute HF in pediatric patients with and without the support of the Sputnik PRBP. Overall, the reproduced state of the pediatric cardiovascular system is very similar to the state of an adult blood circulation during heart failure. The comparison of partial and full support with the condition without support of the Sputnik PRBP shows that the systolic pressure in the ventricle decreases, the ventricular volume decreases, and the pressure in the aorta increases, which leads to unloading of the ventricle and an improvement of general hemodynamics.

Figure 11 represents dynamic H-Q curves of Sputnik 1 (Figure 11(a)) and Sputnik 2 (Figure 11(b)) LVADs supporting moderate and congestive HF states of the LV at pump speeds of partial-to-full support change and total work attainment of the

normal LV stroke work level. Figure 12 represents dynamic H-Q curves of the Sputnik PRBP in corresponding states. In Figure 11, it is shown that, during the filling of the ventricle, the pressure in the pump remains constant (top flat area of the figure) with changing flow in the pump, whereas its value approximately corresponds to the average aortic pressure of about 100 mmHg. A similar observation can be made in Figure 12. The flow rate and the pressure increases with higher rpm. However, in this case, the mean aortic value corresponds to the average value of the pressure head during the ventricular filling phase. The pressure during the filling phase becomes less stable in comparison to the adult models (Figure 11), due to limitations imposed by the miniaturization of the device for pediatric patients.

4. Discussion

The unloading tendency of the LV is observed in all simulations for all heart failure states with a connected LVAD,

(a)

(b)

(c)

(d)
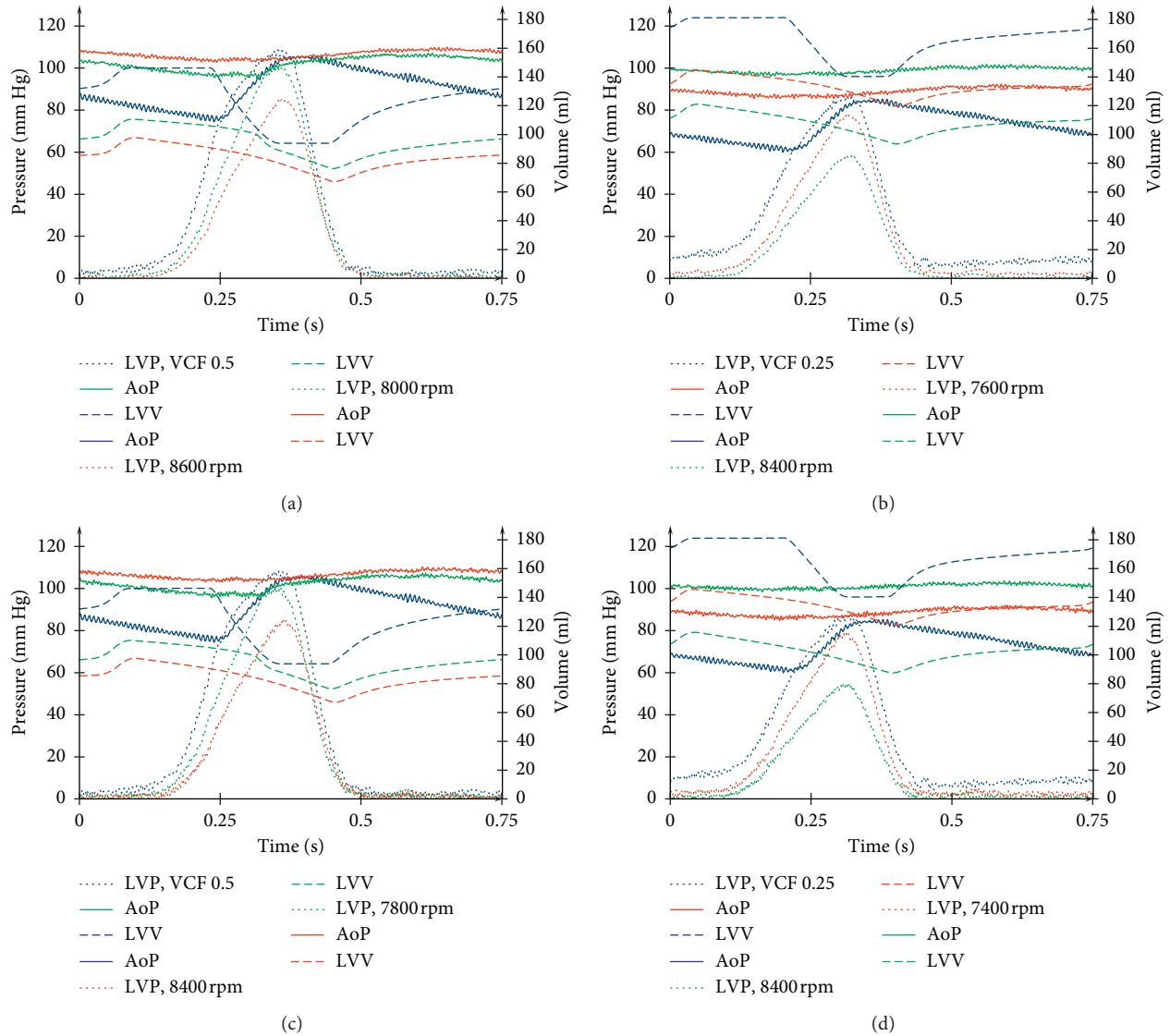
FIGURE 9: Time courses of the left ventricular (LV) pressure, the volume, and the aortic pressure for moderate and congestive heart failure states simulated with the HAMC at the pump speeds of aortic valve closure (red) and total work attainment of a normal LV stroke work level (green): (a) and (b) during Sputnik 1 LVAD support; (c) and (d) during Sputnik 2 LVAD support. Blue lines represent time courses of condition characteristics simulated without support. Dot lines demonstrate the left ventricle pressure, single lines demonstrate the aortic pressure, and dash lines represent the left ventricle volume.

when the pump speed increases within a certain range. This, coupled with an increased average hydraulic pump work, leads to a systemic circulation performance improvement. This is also clearly indicated by the development of the average total work and the average total flow rate of the LV and the LVAD. The change from the partial support to full support is accompanied by the aortic valve closure followed by an aortic back flow. This behavior occurs at a certain operation mode for each LVAD and depends on the residual LV contractility. Thus, based on this operation mode, the LVAD becomes the only fluid actuator in the circulatory system.

Figures 4–6 show that characteristics of the total average work of the LV and LVAD linearly increase with pump speed. This happens also in the speed ranges of 5000–6200 rpm and

5000–5400 rpm for Sputnik 1 LVAD at VCFs of 0.5 and 0.25, respectively, and 5000–6400 rpm and 5000–5600 rpm for Sputnik 2 LVAD at VCFs of 0.5 and 0.25, respectively. If the average hydraulic pump work is negative, the pumps do not provide any significant support for the LV. This is observed in the pump flow rates within specified speed ranges, which are negative as well. Further pump speed increase causes the hydraulic pump work to become higher. Moreover, the total work of the LV and LVAD grows leading to more significant support and unloading of the LV.

In the case of the Sputnik PRBP, an average hydraulic pump work is negative in the speed range of 6000–7800 rpm, although the flow rates are positive. Also, there is an obvious correlation between the average aortic valve flow rate and the average hydraulic pump work, i.e., the hydraulic pump work
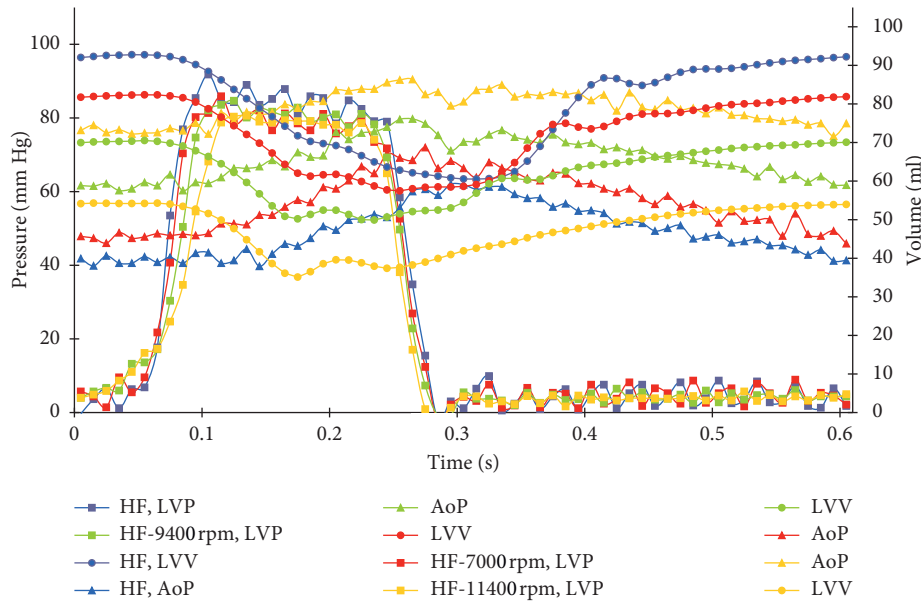
FIGURE 10: Time courses of the left ventricular (LV) pressure and volume; aortic pressure for acute heart failure in pediatric patient with body weight of 15.2 kg at the various pump speeds for partial support (red), partial-to-full support change (green), and total work attainment of a normal LV stroke work level (yellow). Blue lines represent time courses of condition characteristics simulated without support.
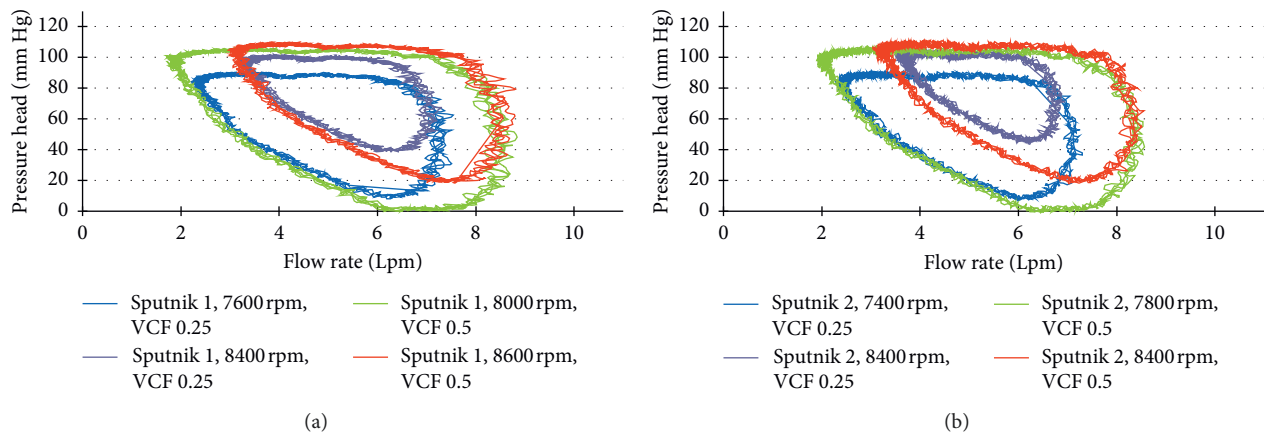
FIGURE 11: Dynamic pressure head-flow rate curves of Sputnik 1 and Sputnik 2 LVADs supporting LV in the moderate and the congestive heart failure state at the pump speeds of partial-to-full support change (blue and red) and full support state (green and purple).

exceeds the LV stroke work right after the aortic valve closure. This correlation does not match the adult Sputnik LVADs tendency, as the hydraulic pump work overshoots the LV stroke work before the aortic valve closes.

The dependencies between the EDV and the stroke work for the Sputnik 1 and Sputnik 2 LVADs at a VCF of 0.25 have an inflection point, which corresponds to an aortic valve closure. At this point, the slope of the EDV becomes steeper as the stroke work decreases.

Due to improvements in the design, the Sputnik 2 LVAD allows to achieve LV normal state characteristics slightly quicker than Sputnik 1 LVAD, i.e., at lower pump speed. An exception needs to be done for the LV and LVAD total work at a VCF of 0.25 which is achieved at the same speed as the Sputnik 1 LVAD. Almost simultaneously, the normal state work and the flow rate are achieved by the Sputnik 1 and Sputnik 2 LVADs, i.e., at similar pump speeds. In the case of the Sputnik PRBP, a normal level of the total work is achieved at a slightly lower speed in comparison to the normal flow rate. However, the speed difference is only 200 rpm. Thus, obtaining the normal average flow rate during a support with the Sputnik PRBP, it can be seen that the total work of a normal state along with sufficient LV unloading is achieved.

EDV is another indicator of the LV unloading, since it decreases with increasing pump speed (Figure 8(d)). The correlation between EDV and the pump speed for VCFs of 0.5 and 0.25 is almost equal for Sputnik 1 and Sputnik 2 LVADs. Also, the relationship between the average stroke work and the average hydraulic pump work is very similar for Sputnik 1 and Sputnik 2 LVADs at corresponding VCFs. It can be concluded that the results of the experiments for
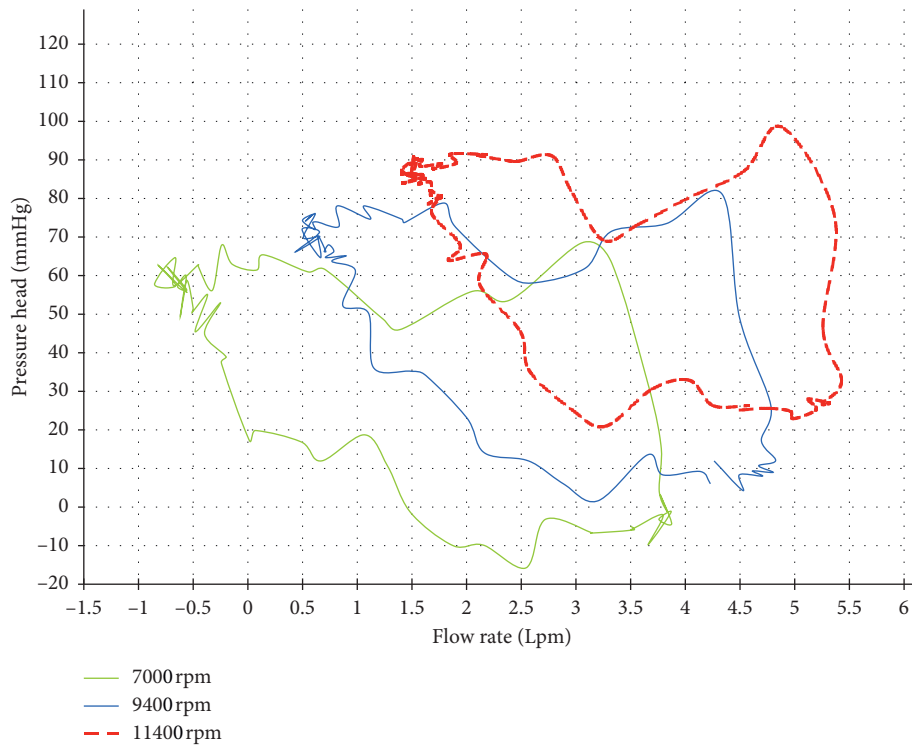
FIGURE 12: Dynamic pressure head-flow rate curves of Sputnik PRBP supporting failing pediatric LV at the pump speeds for the partial support state (green), the partial-to-full support change (blue), and the full support state (red) with the total work attaining normal LV stroke work level.

Sputnik 1 and Sputnik 2 LVADs show very strong interrelations in spite of constructive differences.

All pump flow rate pulsatility indices of the adult Sputnik LVADs for different VCFs converge to zero at high pump speeds (over 9000 rpm). This behavior is most likely brought by the fact that the LV, as the only pulsatile element of the entire system, ceases to pulse being unloaded with an increase in pump speed. Therefore, all characteristics including the pump flow rate become less pulsatile. The flow rate pulsatility index of the Sputnik PRBP shows the same but more gradual trend with respect to pump speed.

The presented research shows that RBPs differently influence the LV depending on heart failure degree. Thus, significant support levels cannot be obtained for a VCF of 0.25 in the HAMC and for pediatric LV in the PMC without an aortic valve closure in comparison to a VCF of 0.5 in the HAMC. To solve this problem, the implementation of control algorithms providing a modulation of the LVAD speed in order to open the aortic valve and to unload the LV more efficiently is needed. Moreover, the importance of maintaining pulsatility has been suggested in many journals. There are restrictions for mechanical support when a patient's health is in a very poor condition. Algorithms of the physiological control may be exceptionally useful to overcome this issue. Ando et al. has recently created a pulsatile mode for continuous-flow left ventricular assist devices which can produce pulsatility comparable to the physiological pulsatile flow [26]. Bozkurt et al. showed that it is possible to obtain more physiological pulsatile hemodynamics in the arteries by applying output-driven varying

speed control to a CF-LVAD [27]. Soucy et al. conducted a research where it was shown that pump speed modulation increases pulsatility and improves cardiac function and endorgan perfusion [28]. The same applies to investigation conducted regarding pulsation generation [29]. For instance, Vincent et al. showed that the modulation of von Willebrand factor levels could explain the relationship between pulsatility and bleeding observed in CF-MCS recipients [30]. Whereas, Edwards et al. showed that low pulsatility index is associated with an increased hazard of overt gastrointestinal bleeding in their cohort of HeartMate II recipients [31].

4.1. Limitations. An absence of the aortic back flow in the HAMC should be considered as a limitation of the presented study, since this condition is frequently observed in patients during LVAD support on relatively high speeds and its presence could lead to more accurate results for the adult Sputnik LVADs.

The Frank–Starling mechanism is simulated according to equations for ventricular pressure and volume. It should be noted that there is no automated feedback mechanism simulating Frank–Starling mechanism in the pediatric mock circulatory system in this study. However, in our case, the Frank–Starling mechanism is implemented according to previously manually selected parameters of contractility and finite diastolic volume.

5. Conclusion

The present work underlines the importance to simulate operating conditions of the human body during the

development of a bioengineering device designed for implantation. The significance of pulsatility is highlighted in this work in addition to its importance in clinical applications (i.e., the cardiac recovery in patients and possibility to predict the risk of the gastrointestinal bleeding in patients with LVAD). In this work, we investigated the interaction between different Sputnik LVADs and the LV with different degrees of HF. We evaluated various LVADs: adult Sputnik 1, Sputnik 2, and Sputnik pediatric RBP (PRBP) engineered for pediatric patients with body a weight between 12 kg and 40 kg. We show the influence of the Sputnik LVADs on the LV depending on the HF degree by the estimation crucial parameters of LV unloading and investigation energetic characteristics of the LV-LVAD interaction for adult and pediatric Sputnik LVADs. Finally, we state that since significant support levels cannot be obtained for a VCF of 0.25 in the HAMC and for pediatric LV in the PMC without the aortic valve closure in comparison to a VCF of 0.5 in the HAMC, it is necessary to investigate control algorithms providing a modulation of the LVAD speed in order to open the aortic valve and unload the LV more efficiently.

Data Availability

All the data used to support the findings of this study are available from the corresponding author upon request.

Conflicts of Interest

The authors declare that there are no conflicts of interest regarding the publication of this paper.

Acknowledgments

References

[1] J. T. Vuong, S. A. Jacob, K. M. Alexander et al., "Mortality from heart failure and dementia in the United States: CDC WONDER 1999-2016," *Journal of Cardiac Failure*, vol. 25, no. 2, pp. 125–129, 2019.

[2] R. L. Kormos, J. Cowger, F. D. Pagani et al., "The society of thoracic surgeons intermacs database annual report: evolving indications, outcomes, and scientific partnerships," *The Annals of Thoracic Surgery*, vol. 107, no. 2, pp. 341–353, 2019.

[3] A. Murphy, C. O. Johnson, G. A. Roth et al., "Ischaemic heart disease in the former soviet union 1990–2015 according to the global burden of disease 2015 study," *Heart*, vol. 104, no. 1, pp. 58–66, 2018.

[4] G. A. Giridharan, T. J. Lee, M. Ising et al., "Miniaturization of mechanical circulatory support systems," *Artificial Organs*, vol. 36, no. 8, pp. 731–739, 2012.

[5] B. J. E. Misgeld, D. Rüschen, S. Schwandtner, S. Heinke, M. Walter, and S. Leonhardt, "Robust decentralised control of a hydrodynamic human circulatory system simulator," *Biomedical Signal Processing and Control*, vol. 20, pp. 35–44, 2015.

[6] S. E. Jahren, G. Ochsner, F. Shu, R. Amacher, J. F. Antaki, and S. Vandenberghe, "Analysis of pressure head-flow loops of

pulsatile rotodynamic blood pumps," *Artificial Organs*, vol. 38, no. 4, pp. 316–326, 2014.

[7] R. Amacher, A. Weber, H. Brinks et al., "Control of ventricular unloading using an electrocardiogram-synchronized Thoratec paracorporeal ventricular assist device," *The Journal of Thoracic and Cardiovascular Surgery*, vol. 146, no. 3, pp. 710–717, 2013.

[8] T. Asou, M. Oe, R. Tominaga et al., "Optimal timing for application of ventricular assist devices in patients who cannot be weaned from cardiopulmonary bypass: an experimental study," *ASAIO transactions/American Society for Artificial Internal Organs*, vol. 34, no. 3, pp. 466–469, 1988.

[9] F. Moscato, M. Vollkron, H. Bergmeister, G. Wieselthaler, E. Leonard, and H. Schima, "Left ventricular pressure? Volume loop analysis during continuous cardiac assist in acute animal trials," *Artificial Organs*, vol. 31, no. 5, pp. 369–376, 2007.

[10] A. Di Molfetta, G. Ferrari, R. Iacobelli et al., "Ventricular energetics in pediatric left ventricular assist device patients," *ASAIO Journal*, vol. 63, no. 6, pp. 815–823, 2017.

[11] C. Kontogiannis, D. Aravantinos, I. Nanas et al., "Salutary effects of the PULVAD, a novel implantable counterpulsation assist device, on cardiac mechanoenergetics," *ASAIO Journal*, vol. 65, no. 5, pp. 473–480, 2019.

[12] M. R. Noor, C. H. Ho, K. H. Parker, A. R. Simon, N. R. Banner, and C. T. Bowles, "Investigation of the characteristics of HeartWare HVAD and thoratec heartmate II under steady and pulsatile flow conditions," *Artificial Organs*, vol. 40, no. 6, pp. 549–560, 2016.

[13] L. Cunningham, S. George, A. M. E. Banayosy, and D. Horstmanshof, "Pulmonary artery pulsatile index (PAPi) score may predict risk of gastrointestinal bleeding in patients with left ventricular assist device," *The Journal of Heart and Lung Transplantation*, vol. 38, no. 4, p. S195, 2019.

[14] A. Critsinelis, J. Kraus, H. Lamba et al., "Gastrointestinal bleeding ceases after heart transplantation in patients bridged on continuous-flow LVAD support," *The Journal of Heart and Lung Transplantation*, vol. 38, no. 4, p. S196, 2019.

[15] Y. Yokoyama, O. Kawaguchi, T. Kitao, T. Kimura, U. Steinseifer, and S. Takatani, "Prediction of the external work of the native heart from the dynamic H-Q curves of the rotary blood pumps during left heart bypass," *Artificial Organs*, vol. 34, no. 9, pp. 766–777, 2010.

[16] D. V. Telyshev, A. A. Pugovkin, and S. V. Selishchev, "A mock circulatory system for testing pediatric rotary blood pumps," *Biomedical Engineering*, vol. 51, no. 2, pp. 83–87, 2017.

[17] S. V. Selishchev and D. V. Telyshev, "Ventricular assist device sputnik: description, technical features and characteristics," *Trends in Biomaterials & Artificial Organs*, vol. 29, no. 3, pp. 207–210, 2015.

[18] J. Yu and X. Zhang, "Hydrodynamic and hemolysis analysis on distance and clearance between impeller and diffuser of axial blood pump," *Journal of Mechanics in Medicine and Biology*, vol. 16, no. 2, Article ID 1650014, 2016.

[19] S. V. Selishchev and D. V. Telyshev, "Optimisation of the sputnik-VAD design," *The International Journal of Artificial Organs*, vol. 39, no. 8, pp. 407–414, 2016.

[20] W.-C. Chiu, G. Girdhar, M. Xenos et al., "Thromboresistance comparison of the heartmate II ventricular assist device with the device thrombogenicity emulation-optimized HeartAssist 5 VAD," *Journal of Biomechanical Engineering*, vol. 136, no. 2, Article ID 021014, 2014.

[21] D. V. Telyshev, M. V. Denisov, and S. V. Selishchev, "The Effect of rotor geometry on the H−Q curves of the sputnik

implantable pediatric rotary blood pump," *Biomedical Engineering*, vol. 50, no. 6, pp. 420–424, 2017.

[22] F. Huang, X. Ruan, J. Zou, W. Qian, and X. Fu, "A fast building and effective hydraulic pediatric mock circulatory system for the evaluation of a left ventricular assist device," *ASAIO Journal*, vol. 59, no. 6, pp. 575–585, 2013.

[23] D. Telyshev, M. Denisov, A. Pugovkin, S. Selishchev, and I. Nesterenko, "The progress in the novel pediatric rotary blood pump sputnik development," *Artificial Organs*, vol. 42, no. 4, pp. 432–443, 2018.

[24] S. Heinke, C. Pereira, S. Leonhardt, and M. Walter, "Modeling a healthy and a person with heart failure conditions using the object-oriented modeling environment Dymola," *Medical & Biological Engineering & Computing*, vol. 53, no. 10, pp. 1049–1068, 2015.

[25] G. Ferrari, A. Di Molfetta, K. Zieliński et al., "Control of a pediatric pulsatile ventricular assist device: a hybrid cardiovascular model study," *Artificial Organs*, vol. 41, no. 12, pp. 1099–1108, 2017.

[26] M. Ando, T. Nishimura, Y. Takewa et al., "Electrocardiogram-Synchronized rotational speed change mode in rotary pumps could improve pulsatility," *Artificial Organs*, vol. 35, no. 10, pp. 941–947, 2011.

[27] S. Bozkurt, F. N. van de Vosse, and M. C. M. Rutten, "Improving arterial pulsatility by feedback control of a continuous flow left ventricular assist device via in silico modeling," *The International Journal of Artificial Organs*, vol. 37, no. 10, pp. 773–785, 2014.

[28] K. G. Soucy, G. A. Giridharan, Y. Choi et al., "Rotary pump speed modulation for generating pulsatile flow and phasic left ventricular volume unloading in a bovine model of chronic ischemic heart failure," *The Journal of Heart and Lung Transplantation*, vol. 34, no. 1, pp. 122–131, 2015.

[29] B. Ji and A. Undar, "An evaluation of the benefits of pulsatile versus nonpulsatile perfusion during cardiopulmonary bypass procedures in pediatric and adult cardiac patients," *ASAIO Journal*, vol. 52, no. 4, pp. 357–361, 2006.

[30] F. Vincent, A. Rauch, V. Loobuyck et al., "Arterial pulsatility and circulating von Willebrand factor in patients on mechanical circulatory support," *Journal of the American College of Cardiology*, vol. 71, no. 19, pp. 2106–2118, 2018.

[31] A. L. Edwards, P. Fitzmorris, S. V. Pamboukian, J. F. George, C. M. Wilcox, and S. Peter, "Association of pulsatility with gastrointestinal bleeding in a cohort of heartmate II recipients," *ASAIO Journal*, vol. 64, no. 4, pp. 472–479, 2018.

Review Article

A Contemporary Systematic Approach to Assessing the Patient with Heart Failure with Reduced Ejection Fraction: Multimodal Noninvasive and Invasive Evaluation

Siu-Hin Wan [ID]**, Paul M. McKie, and John P. Bois** [ID]

Department of Cardiovascular Diseases, Mayo Clinic, Rochester, MN, USA

Correspondence should be addressed to John P. Bois; bois.john@mayo.edu

Heart failure with reduced ejection fraction (HFrEF) is a progressive clinical syndrome commonly associated with left ventricle dilatation and characterized by reduced cardiac output, secondary pulmonary and systemic venous congestion, and inadequate peripheral oxygen delivery. It is common yet complex and requires synthesis of evidence-based guidelines along with strong clinical acumen. The following is a review of an illustrative case that highlights the important clinical considerations in diagnosis, assessment, and management of HFrEF commonly encountered in practice. Explanations provided highlight of the relevant pathophysiology of HFrEF as well as detailed explanations of interpretation of examinations and both noninvasive and invasive assessment in heart failure. The example provided would hopefully serve as a potential point of reference for trainees as well as healthcare practitioners for patients with HFrEF.

1. Introduction and Disease Overview

1.1. Prevalence and Etiology. 5.1 million Americans suffer from heart failure with annual associated healthcare expenditures nearing $30 billion [1]. Heart failure severity is classified into stages A through D by the American College of Cardiology and the American Heart Association. Heart failure with reduced ejection fraction (HFrEF) is a clinical syndrome defined by systolic dysfunction with inadequate tissue perfusion and generally associated with an ejection fraction of less than or equal to 40%. Approximately half of the patients with heart failure have HFrEF and half have heart failure with preserved ejection fraction (HFpEF). The differential diagnosis for etiologies of HFrEF is broad (Table 1) with coronary artery disease and hypertension as the most common precipitants.

1.2. Pathophysiology. HFrEF arises from cardiac myocyte dysfunction leading to decreased contractile force. Neurohumoral systems such as the renin-angiotensin aldosterone and sympathetic nervous system compensate by increasing preload and heart rate. The resultant ventricular dilatation serves to maintain stroke volume and ultimately ensure sufficient systemic perfusion. However, chronic activation of these neurohumoral systems predisposes surviving myocytes to pathologic remodeling and further cardiac dysfunction [2]. In early stages of heart failure, the natriuretic peptide system counteracts the deleterious effects of maladaptive neurohumoral activation but is dysfunctional in later stages of heart failure. Ultimately, the heart reaches its limit to compensate and cardiac output is unable to meet demand.

2. Clinical Presentation

2.1. History. A seventy-three-year-old African American man with a history of long-standing paroxysmal atrial fibrillation on warfarin therapy, hypertension, dyslipidemia, and stage III chronic kidney disease (GFR 52 mL/min) presented with a two-year history of progressive dyspnea on exertion. The patient's symptoms initially occurred after walking two miles but now developed after only walking a

Table 1: Differential diagnosis for etiologies of heart failure with reduced ejection fraction (HFrEF).

Coronary artery disease
Hypertension
Diabetes
Familial cardiomyopathies
Tachycardia-induced cardiomyopathy
Infectious agents: bacterial, viral
Infiltrative disorders
Toxins
Nutritional deficiencies
Electrolyte disorders
Collagen vascular disorders
Endocrine and metabolic diseases
Peripartum cardiomyopathy
Obstructive sleep apnea
Idiopathic

Adapted from Mayo Board Review Textbook, Table 93.5, page 862.

half-mile. He denied cough, fever, orthopnea, paroxysmal nocturnal dyspnea, or angina. He noted trace bilateral lower extremity edema and occasional palpitations.

He had no known history of coronary artery or structural heart disease. There were no underlying pulmonary disorders and he was a never smoker. There was no family history of cardiovascular disease, and the patient had maintained a healthy body weight and exercise regimen, although now with decreasing tolerance.

Pertinent cardiovascular medications included warfarin for antithrombotic prophylaxis, diltiazem to maintain heart rate control, and hydrochlorothiazide for blood pressure management.

2.2. History Discussion.
The initial differential for this case is broad and should include pulmonary pathology, deconditioning, and various cardiac etiologies.

Possible cardiac etiologies include arrhythmias, structural heart disease, and coronary artery disease. Heart failure should be considered as the clinician formulates the diagnostic approach. The clinical history is notable for bilateral lower extreme edema coupled with exertional dyspnea which is suggestive of heart failure. The clinical history is negative for orthopnea and paroxysmal nocturnal dyspnea, two specific findings in heart failure at 81% and 80%, respectively. However, with a sensitivity ranging from 20% to 30%, the lack of orthopnea or paroxysmal dyspnea does not eliminate the possibility of heart failure [3]. Finally, given the patient's age, gender, dyslipidemia, and chronic kidney disease, coronary artery disease should be considered in the primary differential with dyspnea on exertion as a possible anginal equivalent. The clinician should note that renal disease among African-Americans nearly doubles the risk of coronary artery disease.

Pertinent aspects in the history such as maintaining a healthy body weight and appropriate levels of physical activity lessen the probability that simple deconditioning is the culprit for the patient's presentation. Furthermore, the lack of smoking coupled with no prior known pulmonary disease decreases the likelihood that a primary pulmonary disorder is responsible for the patient's dyspnea on exertion.

2.3. Physical Examination.
Upon initial presentation, the patient appeared comfortable and well nourished. The heart rate was 77 beats per minute and regular, blood pressure was 125/82 mmHg, respiratory rate was 12 breaths per minute with an oxygen saturation of 96% on room air, and temperature was 36.9 degrees Celsius. Body mass index was recorded at 25.85 kg/m^2.

On inspection, there was jugular venous distention to the angle of the mandible (~12 cm H$_2$O). Palpation revealed that the cardiac apex was both enlarged and displaced lateral to the midaxillary line. There was no parasternal heave, and the second heart sound was not palpable. Cardiac auscultation noted a normal first and an accentuated second heart sound with wide splitting that increased during inspiration but was present throughout the respiratory cycle. A grade II/VI holosystolic murmur was noted at the apex. The murmur did not radiate nor did it change in intensity with respiration or provocative measures such as Valsalva or handgrip maneuver.

The abdominal examination revealed no evidence of hepatomegaly or ascites. The liver was nonpulsatile, and a hepatojugular reflux could not be elicited.

Examination of the extremities revealed no evidence of clubbing, sclerodactyly, joint inflammation, or rash. Grade II pitting edema to just below the knees bilaterally was noted. Posterior tibial and dorsalis pedis pulses were easily palpable bilaterally. Cutaneous and joint examination was unremarkable without evidence of rash, lesions, or joint swelling.

Pulmonary examination revealed no evidence of dullness to percussion, and the lung fields were clear without any detection of rales or decreased breath sounds.

No lymphadenopathy was appreciated upon palpation. Oral examination revealed moist mucous membranes without any other abnormalities.

2.4. Physical Examination Interpretation.
There are several key elements in the physical examination that aid in focusing the differential diagnosis. Most importantly, the cardiac examination suggests a dilated cardiomyopathy given the findings of an enlarged and displaced cardiac apex.

The prominent second heart sound coupled with persistent splitting suggests pulmonary hypertension. The loud S2 in pulmonary hypertension is generated by the increased pulmonary pressure closing the pulmonic valve. There is persistent splitting of the second heart sound that increases with inspiration. Increased pulmonary pressure prolongs the right ventricular ejection time, which delays closure of the pulmonic valve resulting in increased splitting of the second heart sound. The increased return of venous blood to the right ventricle during inspiration further increases the right ventricular ejection time, leading to the finding of wide persistent splitting. Persistent splitting may also be found in other conditions that delay emptying of the right ventricle during systole such as right bundle branch block.

The location, timing, and nature of the grade II/VI holosystolic murmur at the apex are consistent with mitral regurgitation. Mitral regurgitant murmurs are typically appreciated best at the cardiac apex and are often persistent throughout systole. In severe mitral regurgitation, the murmur will increase with increased afterload and will decrease with decreased preload. However, this murmur did neither and is soft in its intensity, suggesting mild or mild to moderate regurgitation.

A proposed mechanism for the mitral regurgitant murmur based upon the physical examination findings is dilation of the mitral valve annulus with resultant decreased ability of the mitral valve leaflets to coapt resulting in secondary mitral regurgitation. An abnormality with the valve itself known as primary mitral regurgitation can be seen in such diseases as mitral valve prolapse. However, a murmur of mitral valve prolapse will often include an audible systolic click, corresponding with prolapse of the valve followed by a murmur. Furthermore, provocative maneuvers that increase afterload or decrease preload should accentuate the murmur of mitral valve prolapse, neither of which was appreciated in this case.

With the suspicion of dilated cardiomyopathy as well as pulmonary hypertension, the next task is to determine if other examination findings suggest the degree of the patient's physiologic compensation. The jugular venous pulse was distended and 2+ peripheral edema was appreciated, suggesting moderate intravascular volume overload. While the lung fields were clear upon auscultation, this finding can be less sensitive in determining clinical volume status in chronic heart failure patients given the ability of the pulmonary lymphatic system to engorge over time and accommodate excess fluid.

There is little on examination to suggest a systemic cause of the suspected dilated cardiomyopathy. For instance, there was no macroglossia that would be appreciated in amyloidosis, no mention of hypogonadism that is associated with hemochromatosis, and no cutaneous abnormalities such as erythema nodosum which is noted in up to a quarter of patients with sarcoidosis.

In regard to the suspicion of pulmonary hypertension, there are several key examination findings that reveal the status of the right ventricle as well as possible clues as to an underlying etiology. First, the patient had appropriate oxygen saturation on room air and no evidence of peripheral cyanosis. Next, it was noted on the examination that a parasternal heave was not appreciated. While the presence of a right ventricular heave is specific for right ventricular hypertrophy (95.7%), it is not sensitive (37.5%) and therefore right ventricular hypertrophy cannot be ruled out by the absence of this finding [4]. Similarly, the hepatojugular reflux, which was not appreciated on examination, is specific (100%) but not particularly sensitive (66%) for diagnosing right ventricular heart failure [5]. The examination includes many pertinent negatives as to possible etiologies of pulmonary hypertension. For instance, kyphosis was noted, but this was mild and therefore unlikely to be causing restrictive lung disease. Auscultation of the lung fields did not reveal any rales that would be associated with interstitial lung disease nor was there evidence of peripheral clubbing. The patient does not have evidence of joint inflammation or skin rash that would suggest an underlying autoimmune disease that would result in pulmonary hypertension. A significant pertinent positive is the discovery of a dilated left ventricle raising the suspicion of an elevated left ventricular end-diastolic pressure contributing to increased pressures in the pulmonary vasculature (Table 2).

2.5. Case Presentation Summary.

A seventy-three-year-old male with a history of paroxysmal atrial fibrillation, dyslipidemia, and chronic kidney disease stage III presented with progressive exertional dyspnea. The differential was broad and included pulmonary disorders such as restrictive or obstructive lung disease, deconditioning, and a variety of cardiac conditions such as coronary artery disease, heart failure, or sequelae from atrial fibrillation such as poor heart rate control.

The clinical examination refined this differential with findings suggestive of a dilated cardiomyopathy with mild to moderate secondary mitral regurgitation and pulmonary hypertension. The subsequent noninvasive evaluation should focus upon confirming these clinical suspicions and defining specific etiologies to guide therapeutic strategies.

2.6. Noninvasive Assessment.

Laboratory evaluation was as follows (findings outside of the normal limits bolded):

Hemoglobin: **13.3** (13.5–17.5 g/dL)

Leukocytes: 9.6×10^9 ($3.5–10.5 \times 10^9$/L)

Mean corpuscular volume: 83 (81.2–95.1 fL)

Platelet count: 204×10^9 ($150–450 \times 10^9$/L)

Creatinine: **1.6** (0.8–1.3 mg/dL)

Sodium: 143 (135–145 mmol/L)

Blood urea nitrogen (BUN): **29** (8–24 mg/dL)

Potassium: 4.2 (3.6–5.2 mmol/L)

Alkaline phosphatase: **125** (45–115 U/L)

Aspartate aminotransferase (AST): 29 (8–48 U/L)

Uric acid: **25** (3.7–8.0 mmol/L)

Thyroid-stimulating hormone (TSH): 2.0 (0.3–5.0 MIU/L)

Amino-terminal proB-type natriuretic peptide (NT-proBNP): **9245** (<107 pg/mL)

Total iron: 114 (50–150 mcg/dL)

Total iron-binding capacity (TIBC): 287 (250–400 mcg/dL)

Ferritin: 112 (24–336 ng/ml)

Total cholesterol: **208** (<200 mg/dL)

Triglycerides: 71 (<150 mg/dL)

High-density lipoprotein (HDL): 59 (>40 mg/dL)

Low-density lipoprotein (LDL): 125 (<130 mg/dL)

Serum and urine protein electrophoresis (SPEP and UPEP) negative for monoclonal gammopathy

TABLE 2: Physical exam findings of pulmonary hypertension.

Sign	Implication
Central cyanosis	Hypoxemia, right to left shunt
Clubbing	Congenital heart disease, pulmonary venopathy
Cardiac auscultation: murmurs, opening snap, gallop	Congenital or acquired heart or valvular disease
Rales, dullness, decreased breath sounds	Pulmonary congestion or effusion
Fine rales, accessory muscle use, wheezing, and prolonged expiration, productive cough	Pulmonary parenchymal disease
Obesity, kyphoscoliosis, enlarged tonsils	Disordered ventilation
Sclerodactyly, arthritis, rash	Connective tissue disorder
Peripheral venous insufficiency or obstruction	Venous thrombosis

Adapted from Mayo Board Review Table 79.3 (page 736).

A twelve-lead resting ECG demonstrated a normal sinus rhythm, left ventricular hypertrophy, and nonspecific ST changes (Figure 1(a)). A twenty-four-hour ambulatory blood pressure monitor documented an average blood pressure of 139/82 mmHg with a maximum blood pressure of 180/118 mmHg. A twelve-lead twenty-four-hour ambulatory Holter monitor noted sinus rhythm with a heart rate varying between 53 and 123 beats per minute with an average heart rate of 70 beats per minute. Two three- to four-beat runs of ventricular tachycardia were noted with a peak rate of 132 beats per minute. No other premature ventricular or supraventricular contractions were noted and the patient remained asymptomatic during the Holter evaluation.

A posteroanterior and lateral chest x-ray noted mild cardiomegaly, a tortuous aorta, and a mild interstitial prominence greatest at the right lung base (Figure 1(b)).

Transthoracic echocardiography demonstrated severe left ventricular enlargement (two-dimensional end-diastolic dimension of 64 mm (expected 37–51) and end-systolic dimension of 54 mm (expected 22–34)) with an ejection fraction of 39% when calculated by biplane volumes (Figures 2(a) and 2(b)). The posterior wall thickness was measured at 12 mm, and the left ventricular mass index was 185 g/m^2. Generalized left ventricular hypokinesis was appreciated. Mild-moderate central mitral valve regurgitation was noted (effective regurgitant orifice of 0.16 cm^2 with a regurgitant volume of 34 cc by proximal isovelocity surface area (PISA)) and was likely secondary to mitral annular dilation. Elevated left ventricular filling pressure was reported with an E to A ratio of 0.67 and a medial E to e' ratio of 20. In restrictive physiology, with elevated left atrial pressures, early diastolic filling is expected to occur rapidly once the mitral valve opens, thus leading to a steep deceleration time. Right ventricular assessment noted normal right ventricular size and function with an estimated right ventricular systolic blood pressure of 39 mmHg based upon a peak tricuspid regurgitant velocity of 2.90 m/sec and an inferior vena cava that was normal in size and collapsed greater than fifty percent of its diameter with inspiration (Figures 3(a)–3(c)).

2.7. Noninvasive Diagnostic Discussion.
The laboratory evaluation is notable for an elevated NT-proBNP which is most commonly elevated in HF, although elevation can be seen in any disease states with increased myocyte stretch or inflammation. The history of chronic kidney disease is confirmed with a calculated GFR of 52 mL/min, consistent with stage III disease. Importantly, TSH, serum ferritin, and monoclonal protein studies are within normal limits, suggesting that thyroid abnormalities, hemochromatosis, or amyloidosis are not playing a role in the patient's clinical presentation. However, if there were specific findings on clinical review, such as neuropathy and macroglossia, or echocardiographic features such as concentric hypertrophy that would be concerning for possible amyloidosis, then tissue acquisition would be recommended for pathologic diagnosis.

The ECG suggests left ventricular hypertrophy (LVH) based upon the Cornell voltage criteria. This criterion sums the R wave in aVL and the S wave in V3, and if greater than 20 mm in females or 28 mm in males, suggests LVH.

The echocardiogram measurements can be utilized to further characterize the patient's hypertrophy (Figure 4). First relative wall thickness can be measured by the following equation (where LVEDD is equal to left ventricular end-diastolic dimension):

$$\text{relative wall thickness} = \frac{(2 \times \text{posterior wall thickness})}{(\text{LVEDD})}. \tag{1}$$

In the current case,

$$\text{relative wall thickness} = \frac{(2 \times 12\,\text{mm})}{64\,\text{mm}} = 0.375. \tag{2}$$

Next, a relative wall thickness of 0.375 can be combined with a calculated left ventricular mass index by echocardiogram of 185 g/m^2 to suggest eccentric hypertrophy (Figure 4). Studies suggest that specification of type of hypertrophy not only correlates with underlying pathophysiology (concentric hypertrophy associated with pressure overload and eccentric hypertrophy associated with volume overload) but also has prognostic implications [6].

Echocardiographic findings are most consistent with a dilated cardiomyopathy given the global hypokinesis and no 2D evidence of infiltrative disorders such as amyloidosis or sarcoidosis. The global hypokinesis suggests a nonischemic etiology, but ischemic heart disease cannot be ruled out. The finding of a depressed ejection fraction with the presentation of dyspnea confirms HFrEF as the diagnosis. The patient is
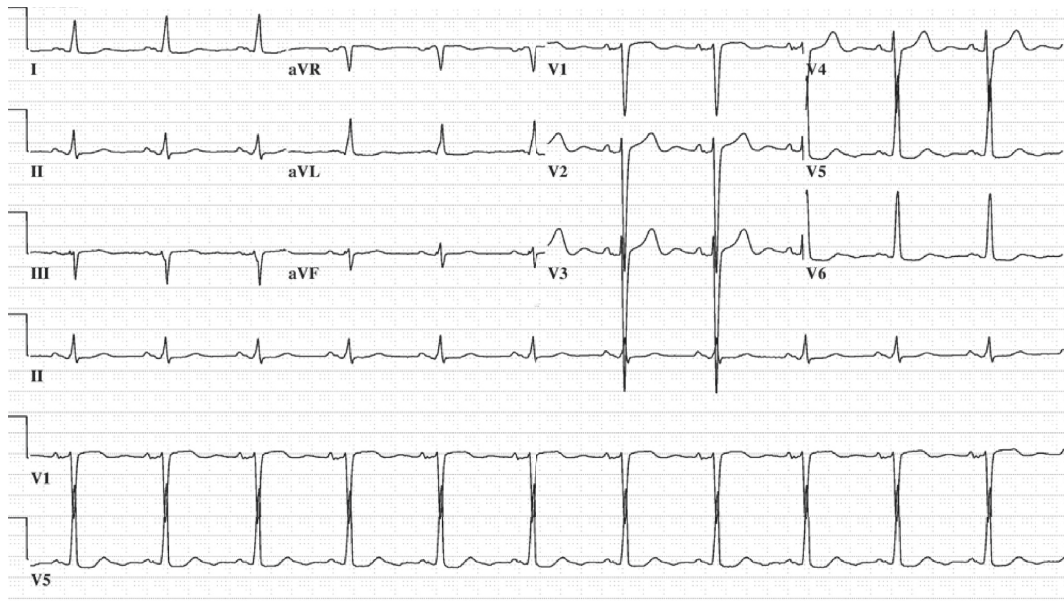
(a)
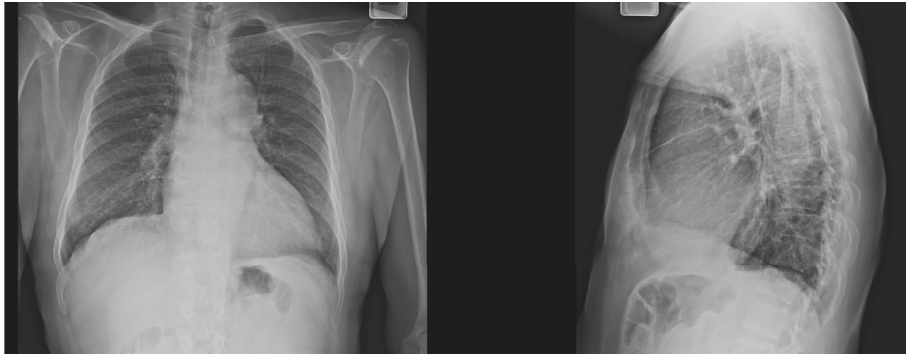
(b)

Figure 1: (a) 12-Lead electrocardiogram: ECG demonstrating sinus rhythm with left ventricular hypertrophy based upon Cornell voltage criteria. (b) Anteroposterior and lateral chest x-ray: demonstrating mild cardiomegaly, a tortuous aorta, and mild interstitial prominence greatest at the right lung base.
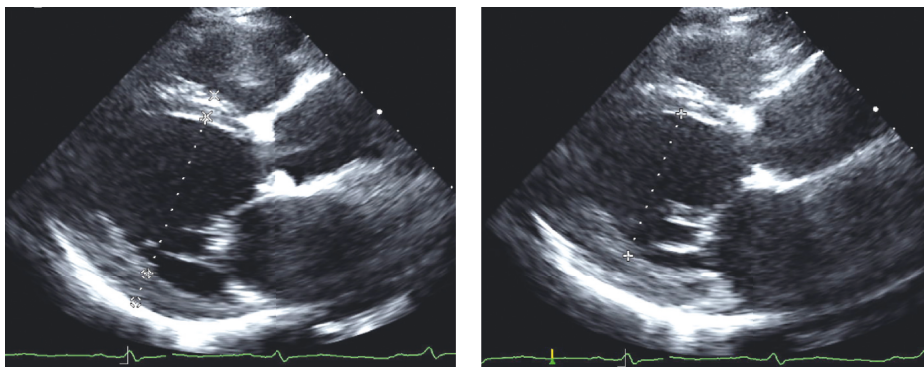
(a)   (b)

Figure 2: Transthoracic echocardiogram for cardiac size and function. (a) Parasternal long-axis view demonstrating severe dilatation (end-diastolic diameter of 64 mm) with normal anterior septal and inferior lateral wall thickness (9 and 12 mm, respectively). (b) Similar view demonstrating increased end-systolic dimension (57 mm) consistent with reduced ejection fraction.

(a)

(b)

(c)

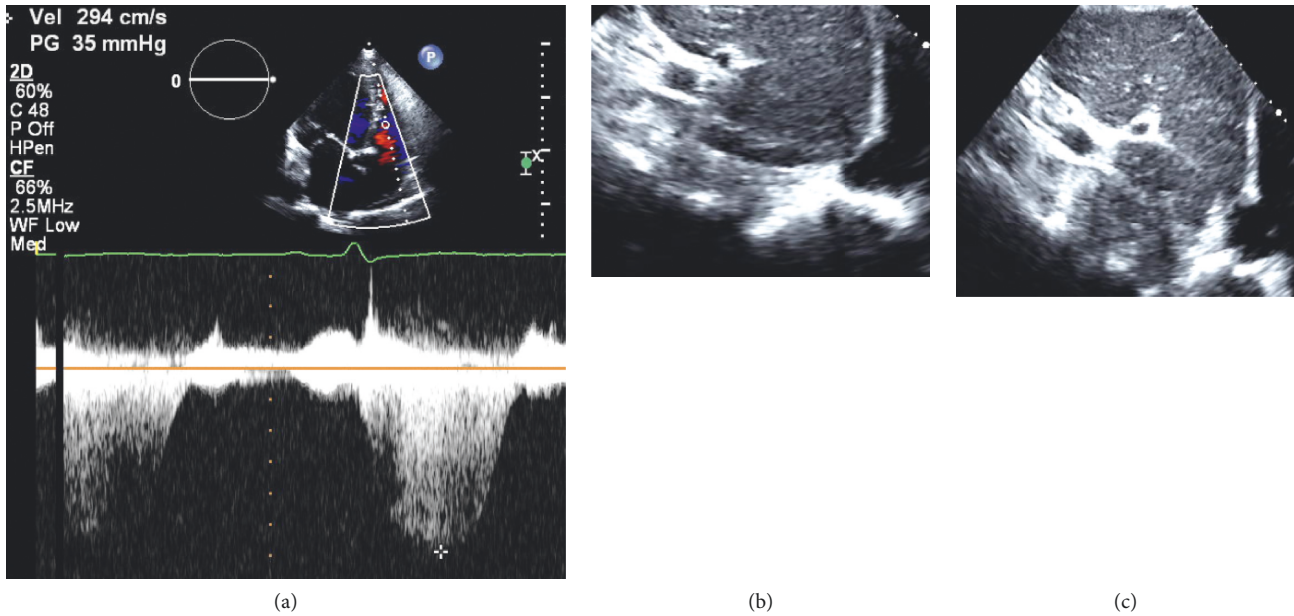FIGURE 3: Transthoracic echocardiogram to determine right ventricular systolic pressure (RVSP). (a) Continuous-wave Doppler measurement of peak tricuspid regurgitant velocity of 2.9 m/s. Right ventricular systolic pressure is calculated via the modified Bernoulli equation $\Delta P_{TV} = 4 \times (V_{TR})^2$ or $\Delta P_{TV} = 4 \times (2.9 \text{ m/s})^2 = 34$ mmHg. A small inferior vena on expiration (b) that completely collapses on inspiration (c) consistent with a mean right atrial pressure of 5 mmHg.
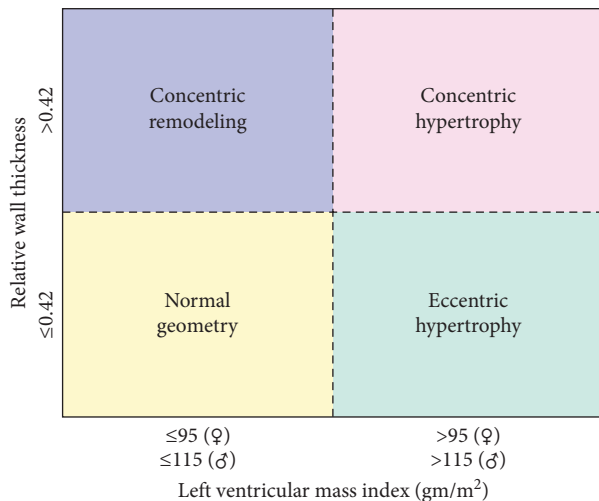

FIGURE 4: Characterization of left ventricular hypertrophy. The patient's ECG (Figure 2) suggests left ventricular hypertrophy. Transthoracic echocardiographic measurement of relative wall thickness (relative wall thickness = $(2 \times$ posterior wall thickness$)/($LVEDD$)$) coupled with left ventricular mass index can determine the specific type of hypertrophy. In the current case, the patient's eccentric hypertrophy is consistent with volume overload secondary to a dilated cardiomyopathy (image from Lang RM. JASE. 2005; 18: 1440–1463).

classified as AHA stage C based on reduced ejection fraction and symptoms (Figure 5).

Echocardiographic assessment of diastolic function suggests increased filling pressures. The Doppler E wave, or early diastolic filling of the left ventricle, reflects the pressure gradient between the left atrium and the left ventricle [7],

whereas the tissue Doppler e' depicts the rate of myocardial relaxation [8]. The elevated E/e' ratio indicates high filling pressures with impaired myocardial tissue relaxation corresponding with a pulmonary capillary wedge pressure greater than 12 mmHg [9]. An elevated E/e' (>15) is a sensitive but not specific determinant for left ventricular filling pressures [8]. In normal physiologic states, lateral e' is greater than medial e'. According to the 2016 ASE Diastolic Function Guidelines, the average of the lateral e' and medial e' should be used in determining left ventricular filling pressures in the setting of reduced ejection fraction.

The underlying pathophysiologic mechanism for HFrEF and associated LV dilatation is illustrated in Figure 6(a). An initial insult decreases left ventricular contractile force by increasing the EDV (x-axis). Initially, left ventricular end-diastolic pressure (LVEDP) (y-axis) remains low (<15 mmHg) and the patient remains asymptomatic (AHA class B, Figure 5). However, if progressive dilatation occurs, the LVEDP begins to rise with resultant dyspnea (AHA class C). Further deterioration leads to a reduction in stroke volume and inability to maintain necessary end-organ perfusion (AHA class D).

The chest x-ray is consistent with left ventricular and not right ventricular enlargement which is concordant with the physical examination findings. There is no evidence of lymphadenopathy that would be associated with sarcoidosis.

The ambulatory blood pressure and Holter monitors yield important data. Notably, the patient has suboptimal blood pressure control but does have appropriate rate control. Therefore, it is unlikely that he is suffering from a tachycardic or premature ventricular contraction-induced cardiomyopathy. However, his afterload is significantly
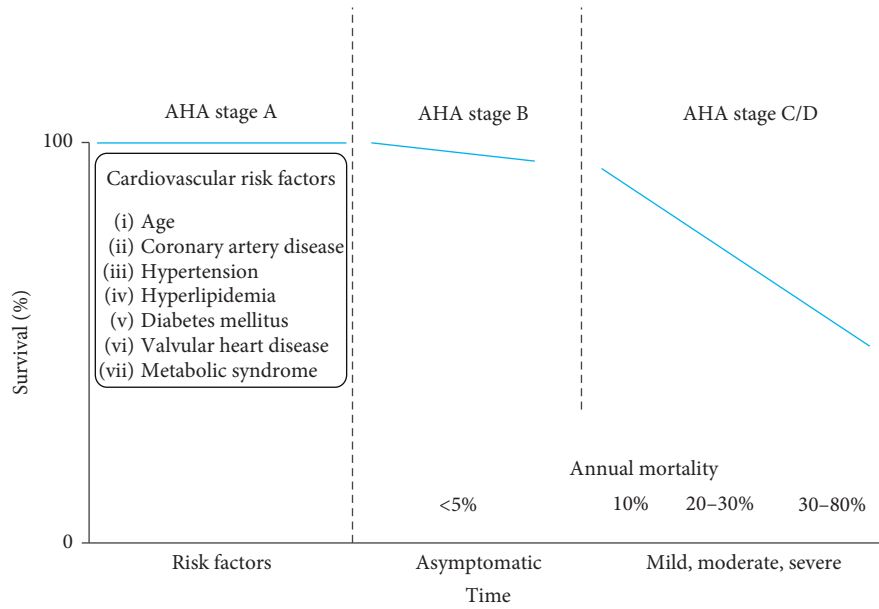
FIGURE 5: Correlation of AHA stage and survival. Note the marked deterioration in survival once the patient becomes symptomatic (the patient in the current case is AHA class C, mild to moderate with an annual mortality between ten and twenty percent) (adapted from Mayo Board Review, Figure 93.1 (page 859)).

elevated, particularly given his reduced ejection fraction, which may be playing a role in his symptomatology.

As indicated by the physical examination, the systolic murmur was consistent with secondary mitral regurgitation due to mitral annular dilatation. On echocardiography, a large central jet of regurgitation associated with central lack of coaptation in the setting of left ventricular and left atrial dilatation would support secondary mitral regurgitation. The right ventricular size and function are within normal limits which are consistent with the physical examination findings of no parasternal lift, jugular venous pressure elevation, ascites or hepatojugular reflux, and minimal peripheral edema. Interestingly, the right ventricular systolic pressure is only mildly elevated at 39 mmHg (normal at rest 30 mmHg and 40 mmHg with exertion).

2.8. Potential "Discrepant" Measurements. The right ventricular systolic pressure as measured by noninvasive Doppler echocardiography appears mildly elevated in this patient and is discordant with the physical examination findings of a pronounced and persistently split second heart sound throughout the precordium as well as deteriorating exercise tolerance.

Doppler echocardiography assesses right ventricular systolic pressure (RVSP) by employing the modified Bernoulli equation, which correlates pressure change to velocity via the following equation:

$$\Delta P_{TV} = 4 \times (V_{TR})^2, \tag{3}$$

where ΔP_{TV} is equal to the systolic pressure gradient across the tricuspid valve in mmHg and V_{TR} is the Doppler assessment of peak tricuspid regurgitant velocity in m/s.

Subsequently, the size and degree of collapse of the inferior vena cava can be utilized to estimate right atrial pressure (RAP). These two values can be combined to estimate RVSP:

$$RVSP = \Delta P_{TV} + RAP. \tag{4}$$

This utility of this measurement is dependent upon (1) absence of pulmonary stenosis, (2) ability to obtain and correctly measure the tricuspid regurgitant velocity signal during Doppler examination, and (3) correct estimation of the right atrial pressure. Importantly, in severe tricuspid regurgitation, Doppler assessment of RVSP might be underestimated [10]. In these specific scenarios of a discrepancy between physical examination findings and noninvasive evaluation, catheter-based assessment would yield a more accurate measurement of RVSP.

Prior studies have demonstrated that right ventricular systolic pressure by echocardiography could accurately be obtained in 87% of patients. Moreover, simultaneous assessment of right ventricular systolic pressure by invasive hemodynamics and Doppler echocardiography demonstrates excellent correlation (correlation coefficient, $R = 0.96$) [11].

In those patients where a tricuspid regurgitant signal cannot be obtained, then end-diastolic pulmonary regurgitant velocity can be measured as demonstrated in Figure 6(b) (normal less than 10 mmHg). The following equation can be utilized to calculate end-diastolic pulmonary artery pressure:

$$PADP = \Delta P_{PVED} + RAP, \tag{5}$$

where PADP indicates end-diastolic pulmonary pressure, ΔP_{PVED} equals the end-diastolic pressure gradient across the pulmonic valve, and RAP indicates right atrial pressure.
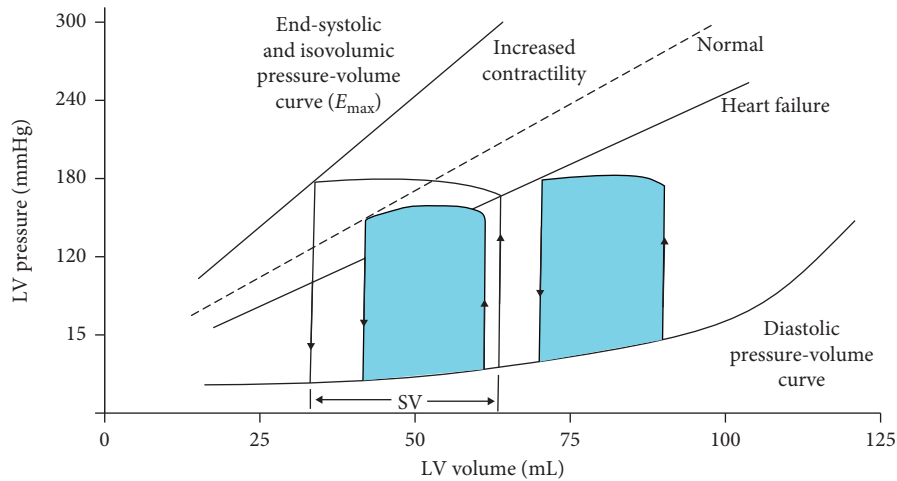
(a)
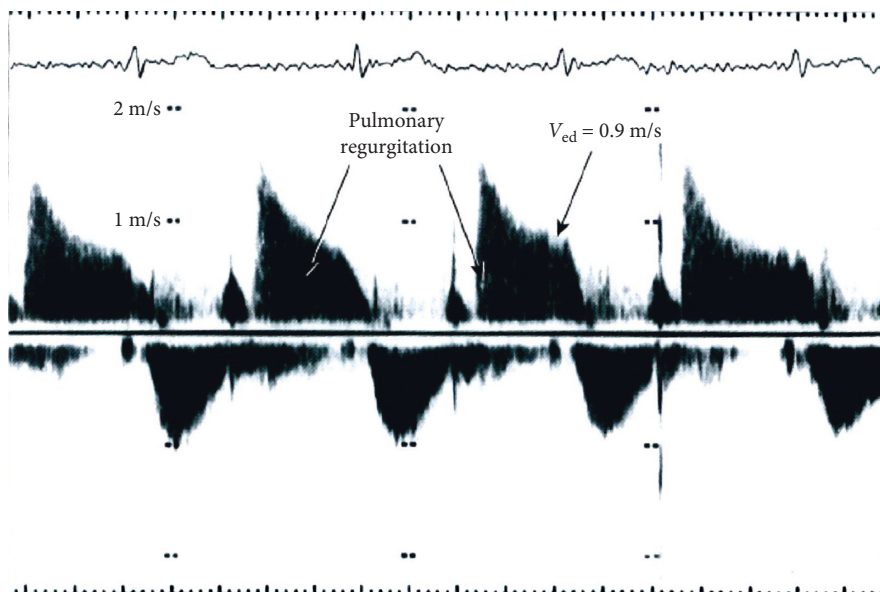
(b)

(c)

FIGURE 6: (a) Pathophysiology of dilated cardiomyopathy. The left ventricle reacts to an initial insult that decreases contractile force by increasing the end-diastolic volume (x-axis). Initially, left ventricular end-diastolic pressure (y-axis) remains low (<15 mmHg) and the patient remains asymptomatic (AHA class B). However, if progressive dilatation occurs, the end-diastolic pressure begins to rise with resultant dyspnea (AHA class C). Further deterioration leads to a reduction in stroke volume and inability to maintain necessa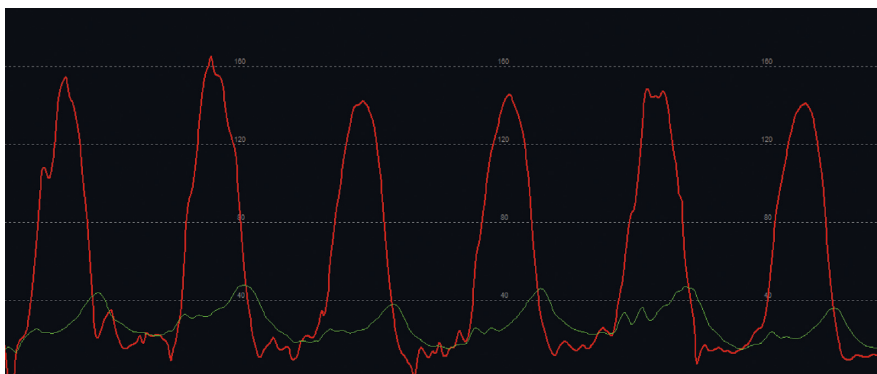ry end-organ perfusion (AHA class D). (a) is found in Mayo Board Review as Figure 91.7 (page 849). (b) Transthoracic echocardiogram to determine RVEDP. Typically obtained in the parasternal short-axis view at the cardiac base, continuous-wave Doppler of the pulmonary regurgitant signal coupled with right atrial pressure can estimate pulmonary artery end-diastolic pressure (PADP) via PADP = ΔP_PVED + RAP. (b) is found in Mayo Board Review as Figure 79.7 (page 743). (c) Left ventricular (red) and pulmonary capillary wedge (PCWP) (green) tracings. Note the elevated left ventricular end-diastolic pressure (white arrow), elevated PCWP (green tracing) with prominent "v" wave (blue arrow).

3. Invasive Assessment

When is invasive evaluation indicated for HFrEF?

The initial invasive hemodynamic evaluation of the ambulatory HF patient may include the following [12]:

(1) A coronary angiogram to determine the burden of coronary atherosclerosis and the possibility of ischemic cardiomyopathy as the underlying etiology for the systolic heart failure (Level IIc).

(2) An endomyocardial biopsy when a "specific diagnosis is suspected that would influence therapy" (Level IIc). A routine endomyocardial biopsy should not be routinely performed in all HF patients (Level III).

(3) Hemodynamic assessment when systemic or pulmonary vascular resistance is uncertain (Level IIc).

Invasive assessment to confirm elevated LVEDP and resultant type II pulmonary hypertension is a class IIb recommendation by the ACC/AHA [12] and the European Society of Cardiology [13]. One could argue in this case that the elevated E/e' on Doppler echocardiography coupled with the underlying cardiomyopathy already suggests elevated left ventricular end-diastolic filling pressures and that treatment should be initiated without the need for further refinement of the diagnosis by catheterization.

However, in the current case, invasive hemodynamic assessment will clarify both the severity and the nature of the pulmonary hypertension, predict response to drug intervention, and aid in determining prognosis. Also, angiography can exclude CAD as underlying mechanism for HF.

In regard to the severity of PH, there is a discrepancy between physical examination findings of a prominent second heart sound that is widely split and only mild elevation of right ventricular systolic pressure on Doppler echocardiography. Measurement of right ventricular systolic pressure during cardiac catheterization will aid in clarifying the severity of pulmonary hypertension. Furthermore, measurement of the wedge pressure (PCWP) and transpulmonary gradient (TPG), which will be described in further detail in the following sections, will determine which type of PH the patient suffers from (discussed in following sections). Furthermore, measurement of the severity of pulmonary hypertension by documenting the transpulmonary gradient and pulmonary vascular resistance will aid in assessing prognosis [13]. Lastly, cardiac catheterization can demonstrate whether acute afterload reduction significantly lowers the TPR which may also impact prognosis particularly in heart transplant candidates [13].

What testing should be performed at invasive cardiac catheterization?

In approaching this case, what tests would you select from the following options?

[X] Right heart pressure assessment (right atrial (RA), right ventricular (RV), pulmonary artery (PA), and pulmonary capillary wedge (PCW) pressures)

[X] Full saturation run (inclusive of peripheral, inferior vena cava (IVC), superior vena cava (SVC), and arterial measures)

[X] Fick cardiac outputs

　[_] Thermodilution cardiac outputs

　[_] Left ventricular pressure assessment (retroaortic)

　[_] Left atrial (LA) pressure assessment (transseptal)

[X] Drug study: pulmonary vs. systemic vasodilator

　[_] Intravenous fluid challenge

　[_] Exercise study

[X] Coronary angiography

　[_] Coronary vasospasm study

　[_] Ventriculography

　[_] Double-sampling dye curves

　[_] Other maneuvers

3.1. Invasive Assessment Planning. There are two main objectives for the invasive assessment of this case. First, a diagnostic coronary angiogram should be performed to evaluate the presence and extent of coronary atherosclerosis. This will help to determine if the patient's dilated cardiomyopathy is ischemic in nature. After completion of the coronary angiogram and with arterial access already in place, the aorta can be crossed in a retrograde fashion in order to assess left ventricular end-diastolic pressure.

The second objective is to confirm and further define the SVR and presence of pulmonary hypertension and how they respond to drug intervention. For this portion of the study, a right heart catheterization should be performed for assessment of the right atrial, right ventricular, pulmonary artery, and pulmonary capillary wedge pressures. These assessments will allow calculation of the TPG, demonstrated below. Furthermore, during the right heart catheterization, measurement of the mixed venous blood saturation and the arterial saturation should be obtained as well as measured assessment of oxygen consumption so that the cardiac output may be calculated via the Fick equation and subsequently the pulmonary vascular resistance (PVR) determined.

If the patient's PCWP is elevated as is suspected, then the final step will be to determine the response to acute systemic arterial vasodilator therapy such as nitroprusside. The presence or absence of a decrease in pulmonary capillary wedge pressure and ultimately TPG suggests an improved prognosis particularly in heart transplant candidates.

The clinical history, physical examination, and non-invasive assessment do not suggest an etiology that would both be readily identifiable on endomyocardial biopsy and that would alter therapeutic strategy. Therefore, in accordance with ACC/AHA guidelines, an endomyocardial biopsy was not pursued [14].

3.2. Pitfalls to Avoid in Invasive Assessment of HF and Type II Pulmonary Hypertension.

There are several critical points to consider when assessing both HF and pulmonary hypertension. The first issue to consider is appropriate method for determining cardiac output. As will be demonstrated in the following section, cardiac output is utilized to determine PVR and the degree of PVR impacts prognosis. There are several methods utilized to determine cardiac output in the invasive hemodynamics laboratory. The thermodilution method analyzes the change in blood temperature over time after a cooled injectant has been introduced to the system. This method has the potential to underestimate cardiac output in patients with markedly low output states or severe tricuspid regurgitation. If the cardiac output were to be underestimated, then the pulmonary vascular resistance would be overestimated. The Fick equation utilizes oxygen consumption to determine cardiac output (equation noted below). Oxygen consumption can be measured in the laboratory or can be "assumed" based upon body weight. However, the assumed oxygen consumption value is often inaccurate and should be avoided as its potential inaccuracy can result in a misleading PVR.

Second, the assessment of PCWP as a surrogate for left ventricular end-diastolic pressure (LVEDP) has been shown to underestimate the true LVEDP. If the operator relied solely on PCWP, then the patient could be misclassified as type I PAH when indeed they had type II PH and be initiated on a drug therapy that would be ineffective and possibly even deleterious. A prior investigation has demonstrated that 53% of cases classified as type I PH based upon a low PCWP were reclassified as type II PH when LVEDP was measured and was demonstrated to be greater than 15 mmHg [15].

Lastly, caution should be utilized when considering the appropriate agent to administer during the drug study. In type I PAH, a pulmonary vasodilator agent such as nitric oxide is administered to determine if the mean pulmonary arterial pressure can be lowered while maintaining or improving cardiac output. Pulmonary vasodilating agents increase preload, and in type II PAH where the LVEDP is already elevated, this can lead to acute volume overload resulting in pulmonary congestion. The correct agent to use in postcapillary PH (type II PH) is an afterload reducing agent such as nitroprusside. This will allow the investigator to determine if better systemic blood pressure control would alleviate the elevated LVEDP and in turn improve the patient's symptomatology.

3.3. Catheterization Results.

Venous and arterial access was obtained via a 7-French right femoral vein sheath and a 6-French right femoral arterial sheath. Judkins left 4 and Judkins right 4 catheters were utilized to engage the left and right coronary system, respectively. Coronary angiography noted mild diffuse disease. The catheter was then advanced into the left ventricle where an end-diastolic pressure of 24 mmHg was recorded.

The catheter was withdrawn into the aorta, and the blood pressure was measured, noted below. Hemoglobin was drawn and noted to be 12.4 g/dL.

Next oxygen consumption was measured at the bedside to be 305.00 ml/min. Arterial oxygen saturation was 92%, and mixed venous blood saturation was 45%. Subsequently, a 7-French 110 cm balloon wedge pressure catheter was introduced through the femoral sheath, and the following measurements were obtained:

Aortic blood pressure (mmHg): 144/75 (Figure 6(c))

Right atrial pressure (mmHg): 14/11, mean = 10

Right ventricular pressure (mmHg): 73/8, end-diastolic pressure = 16

Pulmonary artery pressure (mmHg): 72/32, mean = 49. Oxygen saturation = 45%

Pulmonary capillary wedge pressure (mmHg): mean = 26. Oxygen saturation = 95% (Figure 6(c))

Cardiac output: 3.9 L

Pulmonary vascular resistance (Woods unit, WU): 5.96

A nitroprusside drip was administered at 2 μg/kg/min, and the following data were recorded:

Aortic blood pressure (mmHg): 92/47

Arterial oxygen saturation: 97%

Oxygen consumption: 340.00 ml/min

Pulmonary artery pressure (mmHg): 46/15, mean = 26. Oxygen saturation: 73%

Pulmonary capillary wedge pressure (mmHg): 10

Cardiac output: 8.3 L

Pulmonary vascular resistance (Woods unit, WU): 1.5

The changes in systemic, MPAP, and PCWP are demonstrated in Figures 7(a)–7(c).

3.4. Catheterization Result Discussion.

The coronary angiogram demonstrates no obstructive coronary disease consistent with the diagnosis of nonischemic dilated cardiomyopathy.

The measurements prior to nitroprusside administration confirm markedly elevated filling pressure and low CO consistent with HF. Type II pulmonary hypertension is also present.

To better assess the pulmonary hypertension, the transpulmonary gradient should be calculated:

$$\text{TPG} = \text{MPAP} - \text{PCWP}, \qquad (6)$$

where TPG is equal to the transpulmonary gradient, MPAP is mean pulmonary arterial pressure, and PCWP is pulmonary capillary wedge pressure. In our case,

$$\text{TPG} = 49 \, \text{mmHg} - 26 \, \text{mmHg} = 23 \, \text{mmHg}. \qquad (7)$$

The TPG is ≥12 mmHg which is consistent with postcapillary reactive pulmonary hypertension whereas nonreactive postcapillary PH is ≤12 mmHg. Increased vasomotor tone with accompanying pulmonary artery remodeling underlies the pathophysiology of reactive PH [13]. It is unclear why some type II PH patients develop an elevated TPG.
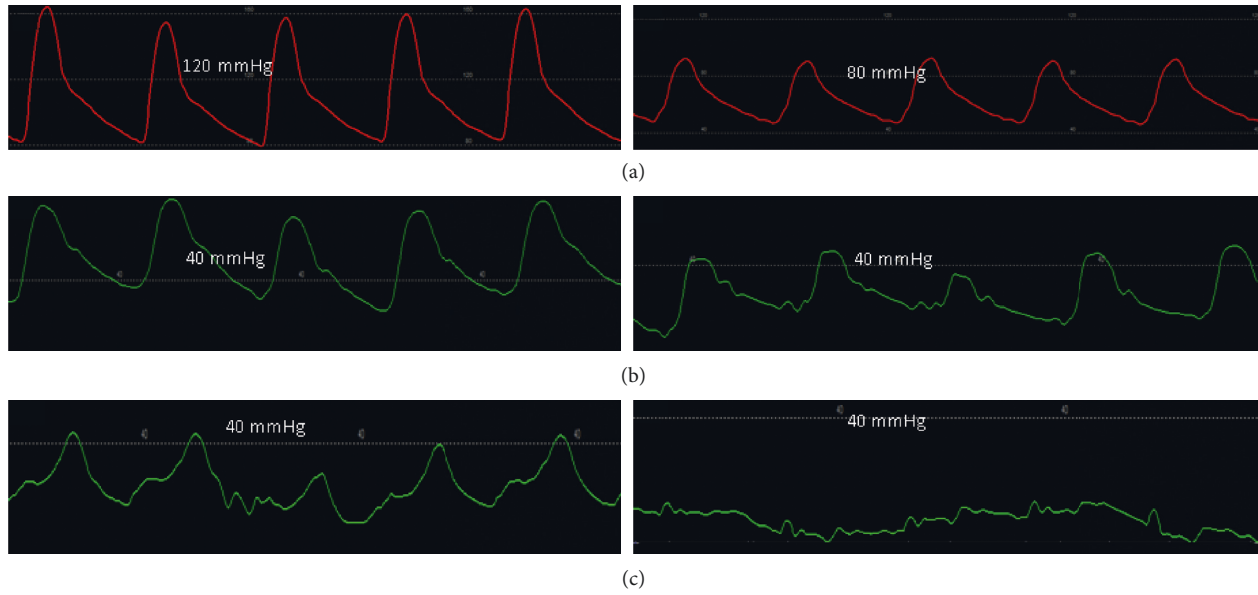
(a)

(b)

(c)

FIGURE 7: Response of systemic, pulmonary arterial, and pulmonary capillary wedge pressure to nitroprusside. The aortic blood pressure and consequently the LVEDP decreased markedly with introduction of nitroprusside (a). Subsequently, the MPAP (b) and the PCWP (c) demonstrated a marked decrease in pressure measurements.

Next, cardiac output should be calculated using the Fick equation as follows:

$$CO = \frac{(VO_2)}{((C_aO_2 - C_vO_2) \times 10)},$$

$$C_aO_2 = \text{hemoglobin concentration}\left(\frac{g}{dL}\right)$$

$$\times 1.36 \, ml \frac{O_2}{g} \text{hemoglobin}$$

$$\times \text{arterial oxygen saturation} (\%),$$

$$C_vO_2 = \text{hemoglobin concentration}\left(\frac{g}{dL}\right)$$

$$\times 1.36 \, ml \frac{O_2}{g} \text{hemoglobin}$$

$$\times \text{venous oxygen saturation} (\%),$$

(8)

where CO is the cardiac output, C_aO_2 is the oxygen content of arterial blood, and C_vO_2 is the oxygen content of venous blood. Oxygen consumption is given at 305 ml/min, hemoglobin is given at 12.4 g/dL, arterial oxygen saturation was 92%, and venous oxygen saturation was 45%. Entering these data, CO can be solved for:

$$CO = \frac{305}{((15.5 - 7.6) \times 10)} = 3.86 \, L/min,$$

$$CI = \frac{CO}{BSA} = \frac{3.9}{1.73} = 2.3 \frac{L/min}{m^2}.$$

(9)

CO can then be utilized to determine pulmonary vascular resistance as follows:

$$PVR = \frac{(MPAP - PCWP)}{CO}.$$

(10)

where PVR is the pulmonary vascular resistance, MPAP is the mean pulmonary artery pressure, MPCWP is the mean pulmonary capillary wedge pressure, and CO is the cardiac output. Therefore, prior to nitroprusside administration, PVR equals

$$PVR = \frac{(49 - 26)}{3.86} = 5.9 \, WU.$$

(11)

Normal PVR is ≤3 WU. This patient's elevated pulmonary vascular resistance is consistent with reactive type II PH.

Note that with the administration of nitroprusside, the systemic blood pressure fell from 144/75 mmHg to 92/47 mmHg. With this acute afterload reduction, there was a marked drop in the MPAP to 26 mmHg, the PCWP to 10 mmHg, and the PVR to 1.5 WU. These findings are reflected in the hemodynamic tracings noted in Figures 7(a)–7(c). The responsiveness of the pulmonary vascular resistance denotes reversibility, suggesting that the underlying pathophysiologic mechanism for the reactive type II PH is increased vasomotor tone rather than remodeling [13].

Also of critical importance is the more than twofold increase in CO from 3.9 to 8.3 L/min. This increase is attributable to the increased VO_2 (from 305 ml/min to 340 ml/min) as well as the increase in mixed venous oxygen saturation from 45% to 73%. The arterial oxygen also increased from 92% to 97%. The postnitroprusside cardiac output is therefore calculated as follows:

$$CO = \frac{340}{((16.4 - 12.3) \times 10)} = 8.3 \text{ L/min.} \qquad (12)$$

3.5. Synthesis. The left ventricular hemodynamic tracing (Figure 6(c)) is consistent with an elevated LVEDP which correlated with the transthoracic echocardiographic finding of an E to e' ratio of 20. Moreover, the "V" seen on the PCWP tracing (Figure 6(c)) is consistent with the known mitral regurgitation and elevated filling pressures. Nitroprusside reduced systemic vascular resistance and mean arterial pressure which decreased LVEDP and improved cardiac output.

The right ventricular systolic pressure is markedly higher with invasive assessment (73 mmHg) compared to non-invasive assessment (39 mmHg). This may be due to an inability to obtain an optimal continuous-wave Doppler signal or due to daily variation in right ventricular systolic pressure. Continuous daily invasive monitoring of right ventricular systolic pressure in PH type I patients has shown significant fluctuations [16], and we might expect similar fluctuations in patients with type II PH. Loading conditions can greatly affect the results of Doppler echocardiography, and exercise stress echocardiography may be quite helpful in identifying exercise-induced pulmonary hypertension and defining causes of exertional dyspnea.

4. Case Resolution

The patient was gradually initiated on a heart failure regimen consisting of carvedilol 25 mg twice daily, lisinopril 20 mg daily, furosemide 40 mg daily, and spironolactone 25 mg daily. The diltiazem was discontinued as it is a negative inotrope. The patient's blood pressure remained elevated, so hydralazine 50 mg three times daily and isosorbide mononitrate 30 mg daily was added to the regimen. Three-month follow-up demonstrated improved blood pressure control correlating with increased exercise tolerance.

Conflicts of Interest

The authors declare that there are no conflicts of interest regarding the publication of this paper.

References

[1] A. S. Go, D. Mozaffarian, V. L. Roger et al., "Heart disease and stroke statistics—2014 update: a report from the American Heart Association," *Circulation*, vol. 129, pp. 399–410, 2014.

[2] J. J. V. McMurray, "Systolic heart failure," *New England Journal of Medicine*, vol. 362, no. 3, pp. 228–238, 2010.

[3] R. D. S. Watson, C. R. Gibbs, and G. Y. Lip, "ABC of heart failure: clinical features and complications," *BMJ*, vol. 320, no. 7229, pp. 236–239, 2000.

[4] N. Pilatis, L. Jacobs, P. Rerkpattanapipat et al., "Clinical predictors of pulmonary hypertension in patients undergoing liver transplant evaluation," *Liver Transplantation*, vol. 6, no. 1, pp. 85–91, 2000.

[5] A. S. Maisel, J. E. Atwood, and A. L. Goldberger, "Hepatojugular reflux: useful in the bedside diagnosis of tricuspid regurgitation," *Annals of Internal Medicine*, vol. 101, no. 6, pp. 781-782, 1984.

[6] A. Verma, A. Meris, H. Skali et al., "Prognostic implications of left ventricular mass and geometry following myocardial infarction," *JACC: Cardiovascular Imaging*, vol. 1, no. 5, pp. 582–591, 2008.

[7] R. A. Nishimura and A. J. Tajik, "Evaluation of diastolic filling of left ventricle in health and disease: Doppler echocardiography is the clinician's Rosetta Stone," *Journal of the American College of Cardiology*, vol. 30, no. 1, pp. 8–18, 1997.

[8] J. K. Oh, S.-J. Park, and S. F. Nagueh, "Established and novel clinical applications of diastolic function assessment by echocardiography," *Circulation: Cardiovascular Imaging*, vol. 4, no. 4, pp. 444–455, 2011.

[9] S. R. Ommen, R. A. Nishimura, C. P. Appleton et al., "Clinical utility of Doppler echocardiography and tissue Doppler imaging in the estimation of left ventricular filling pressures," *Circulation*, vol. 102, no. 15, pp. 1788–1794, 2000.

[10] J. B. Geske, D. C. Scantlebury, J. D. Thomas, and R. A. Nishimura, "Hemodynamic evaluation of severe tricuspid regurgitation," *Journal of the American College of Cardiology*, vol. 62, no. 20, p. e441, 2013.

[11] P. J. Currie, J. B. Seward, K.-L. Chan et al., "Continuous wave Doppler determination of right ventricular pressure: a simultaneous Doppler-catheterization study in 127 patients," *Journal of the American College of Cardiology*, vol. 6, no. 4, pp. 750–756, 1985.

[12] C. W. Yancy, M. Jessup, B. Bozkurt et al., "2017 ACC/AHA/HFSA focused update of the 2013 ACCF/AHA guideline for the management of heart failure: a report of the American College of Cardiology/American Heart Association task force on clinical practice guidelines and the heart failure society of America," *Circulation*, vol. 136, no. 6, pp. e137–e161, 2017.

[13] N. Galie, M. M. Hoeper, M. Humbert et al., "Guidelines for the diagnosis and treatment of pulmonary hypertension: the task force for the diagnosis and treatment of pulmonary hypertension of the European Society of Cardiology (ESC) and the European Respiratory Society (ERS), endorsed by the International Society of Heart and Lung Transplantation (ISHLT)," *European Heart Journal*, vol. 30, pp. 2493–2537, 2009.

[14] L. T. Cooper, K. L. Baughman, A. M. Feldman et al., "The role of endomyocardial biopsy in the management of cardiovascular disease," *Circulation*, vol. 116, no. 19, pp. 2216–2233, 2007.

[15] S. D. Halpern and D. B. Taichman, "Misclassification of pulmonary hypertension due to reliance on pulmonary capillary wedge pressure rather than left ventricular end-diastolic pressure," *Chest*, vol. 136, no. 1, pp. 37–43, 2009.

[16] R. P. Frantz, R. L. Benza, B. Kjellström et al., "Continuous hemodynamic monitoring in patients with pulmonary arterial hypertension," *The Journal of Heart and Lung Transplantation*, vol. 27, no. 7, pp. 780–788, 2008.